A.A. Marelis
4018265

A benchmark study for dynamic multilevel multiscale (ADM) simulation of heat production from low-enthalpy fractured geothermal reservoirs

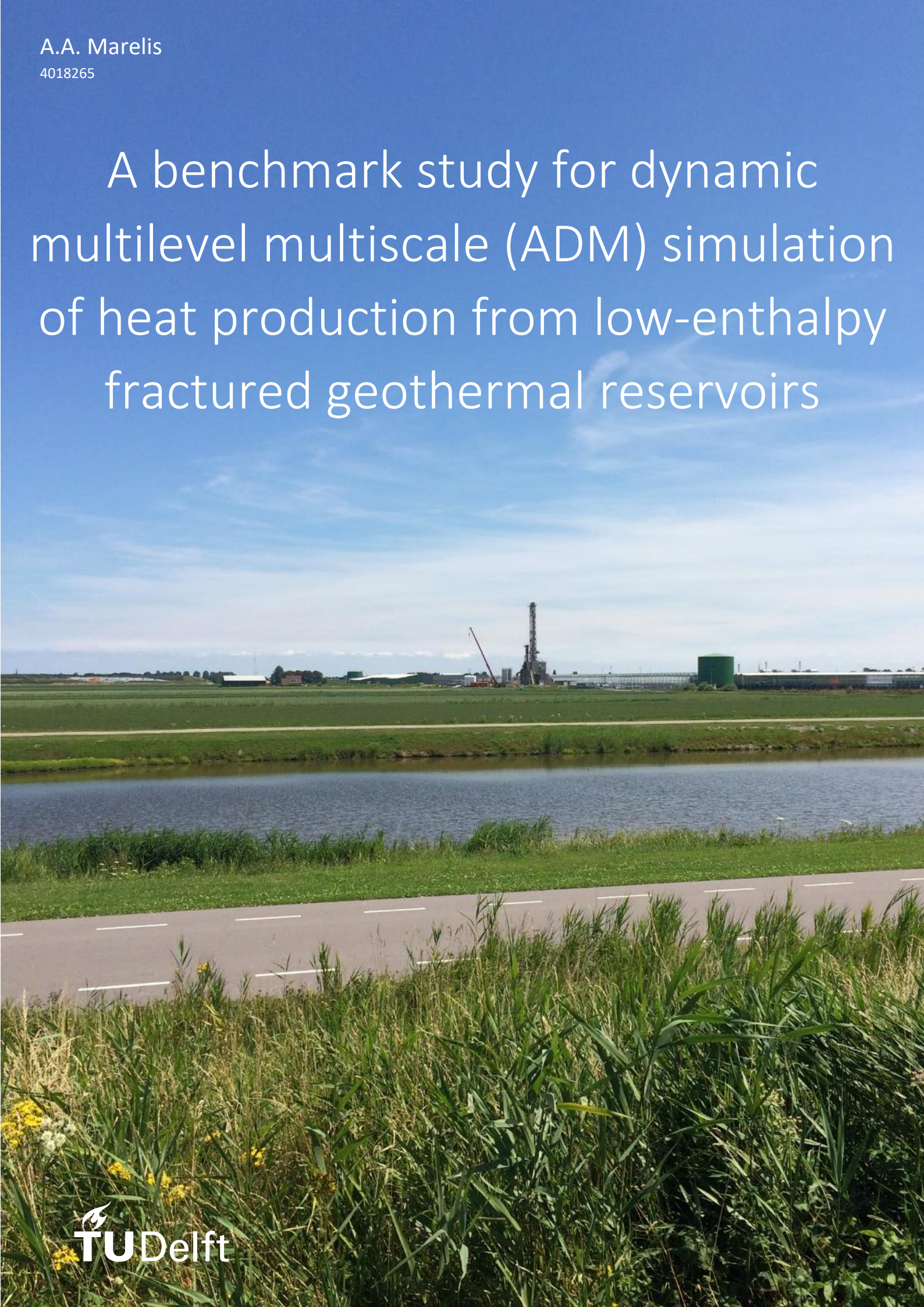

TU Delft

A benchmark study for dynamic multilevel multiscale (ADM) simulation of heat production from low-enthalpy fractured geothermal reservoirs

By

A.A. Marelis

in partial fulfilment of the requirements for the degree of

Master of Science
in Petroleum Engineering and Geosciences

at the Delft University of Technology,
to be defended publicly on Tuesday November 24, 2020 at 13.00 PM.

Supervisor:	Dr. H. Hajibeygi,	TU Delft
Co-supervisor:	M.HosseiniMehr,	TU Delft
Thesis committee:	Dr. P. Vardon,	TU Delft
	Dr. A. Barnhoorn,	TU Delft

This work was conducted in the Delft Advanced Reservoir Simulation (DARSim) group.

An electronic version of this thesis is available at https://repository.tudelft.nl.

TU Delft

Preface

"The story about my adventure in Delft is not one that is just about me"

To Jan and Yvonne, Gonnie and Eric, Casper and Evelien, Sabine and Dirk-jan, and Renzo and Alvar

To John and Frederiek

and most of all to Ella

Thank you all

Arjan Marelis
24-11-2020

Abstract

Accurate and efficient predictions on the behavior of fluid flow and heat transport are required in the development of low-enthalpy geothermal reservoirs in fractured formations. Key challenges include the demand for high-resolution computational grids, the non-linear behavior of the system due to strong mass-heat coupling and the presence of fractures with large heterogeneity contrasts.

In this work, a comparison is made between natural and molar variable formulation used to describe the coupled fluid-heat transport under non-isothermal conditions in low-enthalpy fractured porous media. The solutions and performance of the newly implemented molar formulation are compared to those of the existing natural variable formulation in the DARSim2 reservoir simulation framework. A fully implicit scheme (FIM) is applied to solve the coupled discrete system including mass and energy balance equations. Application of the Algebraic Dynamic Multilevel (ADM) method with projection-based Embedded Discrete Fracture Model (pEDFM) provides a scalable and efficient simulation framework for field-scale fractured reservoirs. The ADM method maps the fine-scale system onto a dynamically defined multilevel grid resolution system (Cusini et al., 2016, HosseiniMehr et al., 2020) based on the solution gradient and a series of restriction and prolongation operators, which ensure accurate capturing of fine-scale heterogeneities. Fractures are defined explicitly as either (highly) conductive passageways or flow barriers using the pEDFM formulation (Tene et al., 2017).

Simulation results using the molar formulation are compared with an analytical solution as verification of the implementation. Results of various (un-)fractured test cases with homogeneous and heterogeneous permeability fields show that there is no clear difference between the solutions and performance of the different primary variable formulations, and the performance itself is largely dependent on the level of complexity embedded in the numerical model independent of the simulation strategy applied.

Acknowledgements

I would like to thank Hadi Hajibeygi for his supervision of this project. A special thanks goes to Mousa HosseiniMehr for all his help and support. The clarity in his explanations is truly admirable.

Contents

1. Introduction

Geothermal energy resources are becoming increasingly important in the energy transition. Due to their high potential for urban (and greenhouse) heating and electricity generation the demand for geothermal power as a renewable form of energy has been rising and is expected to increase in the next decades (Burnell et al., 2012; McClure et al., 2014).

Geothermal resources are most commonly classified as either low- or high-enthalpy resources on the basis of their reservoir temperature (Dickson and Fanelli, 2003). Enthalpy provides a measure of the thermal energy stored in the geothermal system and can be considered proportional to temperature. Following the classification presented by Axelsson and Gunnlaugsson (2000, as cited in Dickson and Fanelli, 2003), low-enthalpy geothermal resources are characterized by temperatures lower than, or equal to $190\ [^oC]$, and high-enthalpy resources have temperatures exceeding $190\ [^oC]$. Note that these temperature ranges are arbitrary and there is no general agreement (Dickson and Fanelli, 2003).

Geothermal systems can be further classified on the basis of the predominant phase of the geothermal fluid (i.e. water- or vapor-dominated) and the equilibrium state of the reservoir (i.e. static or dynamic; conduction- or convection-dominated) (Dickson and Fanelli, 2003; Toth and Bobok, 2017). Examples of static water-dominated geothermal systems are (deep) sedimentary aquifers and Enhanced Geothermal Systems (EGS). Due to a relatively low thermal gradient, such systems are not part of a convective circulation system and are heated only by conduction. Geothermal reservoirs, and especially those that are conduction dominated, are heated by terrestrial heat flow. Following the geothermal gradient, temperature increases with depth. As the practical applications of a geothermal resource are largely dependent on temperature, the depth of the geothermal reservoir can play an important role in determining the suitability of the resource (Toth and Bobok, 2017). Contrary to temperature, porosity decreases exponentially with depth and therefore limits the region in which recoverable hot water reservoirs can be found. The presence of a natural or induced fracture network allows for fluid circulation in an otherwise impermeable formation (Dickson and Fanelli, 2003). Enhancement of permeability by means of hydraulic fracturing is common in enhanced geothermal systems, which are comprised of rock that contains sufficient heat but lacks sufficient intrinsic permeability.

Numerical simulation of heat production from geothermal reservoirs is an essential part in the development of geothermal resources (O'Sullivan et al., 2001; Axelsson et al., 2002). Geothermal reservoir simulation involves modeling of coupled fluid flow and heat transport processes in large-scale geothermal systems. Key challenges include the demand for high-resolution computational grids to be imposed on the entire geothermal system, the non-linear behavior of the system due to the various transport phenomena and the thermodynamic equations of state, and the presence of fractures with large heterogeneity contrasts compared to the rock matrix (Berkowitz, 2002; O'Sullivan et al., 2013; HosseiniMehr et al., 2020).

The non-linearity of the system is largely governed by the Jacobian matrix used in the non-linear solver as it contains the derivatives of the mass and energy balance equations with respect to each of the primary unknowns in the non-linear formulation (Wong et al., 2016). Depending on the type of non-linear formulation used, and the physics that are modeled, these primary unknowns vary. The molar formulation (Faust and Mercer, 1979a) encompasses pressure and enthalpy as the primary unknowns, whereas in the natural formulation (Coats, 1980) pressure, temperature and saturation are defined as the primary unknowns. A comparison study on the non-linear performance between both formulations

has been performed by Wong, Horne and Voskov (2016) which have concluded that there is no apparent preference in terms of formulation and the performance is largely dependent on the complexity of the model problem. Note that in this study the presence of fractures has not been taken into account.

The Algebraic Dynamic Multilevel (ADM) method provides scalable and efficient simulations for large-scale computational domains (i.e. field-scale simulations) by solving a dynamic multilevel system that consists of multiple hierarchically nested grid resolutions at coarse(r) scales (Cusini et al., 2016; HosseiniMehr et al., 2020). The ADM method combines two major concepts; 1) the Multiscale Finite Volume (MsFV) method in which multiscale basis functions allow for accurate coarse-scale treatment of fine-scale heterogeneities whilst avoiding upscaling (Praditia et al., 2018), and 2) a Dynamic Local Grid Refinement (DLGR) approach which applies a fine-scale resolution only in those parts of the domain where it is required (i.e. at the position of moving fronts). Contrary to classical DLGR methods, the algebraic formulation of the ADM method allows for efficient computation of the connections between the different grid resolutions (Cusini et al., 2016). The fine-scale discrete system (including fractures) is mapped onto the dynamic multilevel grid using a series of restriction operators and subsequently solved on the multilevel grid. The restriction operators ensure mass and energy conservation. The solution is prolonged back to the original fine-scale resolution using a series of prolongation operators. The effective grid resolution is determined by any user-defined error estimate criterion such that significant dynamic simulation features are accurately captured (HosseiniMehr et al., 2020). As an example, consider setting a threshold on the temperature gradient in geothermal simulations in order to force a fine-scale resolution on the moving cold-water front.

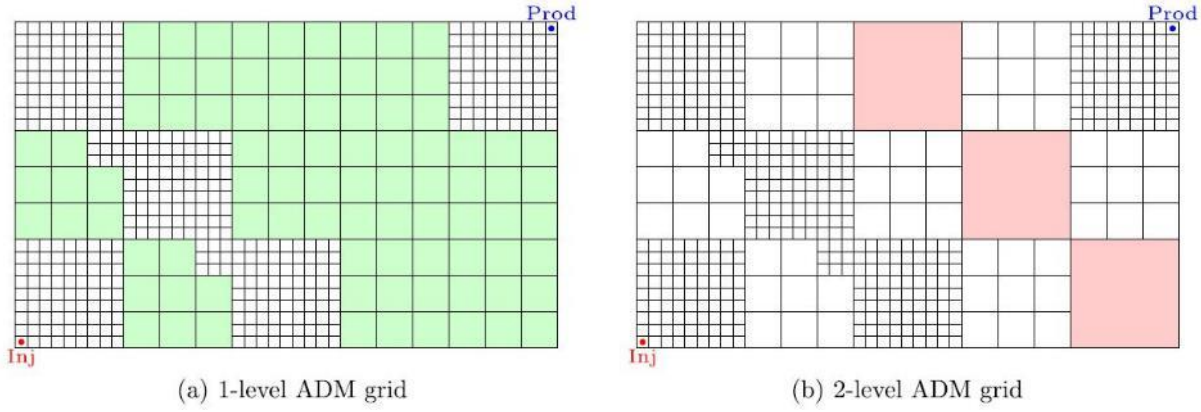

Figure 1.1: Example of 1-level (a) and 2-level (b) ADM solution grids. After Cusini et al., 2016.

Enhancement of intrinsic permeability by means of hydraulic fracturing yields (mainly) highly conductive fractures. In this case, the Embedded Discrete Fracture Model (EDFM) can be applied in order to model the effects of these fractures on reservoir behavior. EDFM employs non-conforming grids to discretize the fractures as lower dimensional objects independently from the matrix grid (HosseiniMehr et al., 2019a). Both domains are connected by conservative flux exchange terms between overlapping matrix and fracture elements. In the case of a naturally fractured geothermal reservoir, EDFM will not suffice as it cannot accurately represent sealing fractures and impermeable faults. Projection-based EDFM (pEDFM) has been specifically designed to allow the consideration of both highly conductive fractures and fractures that act as a barrier to flow (Tene et al., 2017). By developing consistent connectivities between matrix and fracture elements, pEDFM can be applied to naturally fractured reservoirs with an arbitrary range of conductivity contrasts between fracture and matrix (HosseiniMehr et al., 2019a).

HosseiniMehr, Vuik and Hajibeygi (2020) present an Algebraic Dynamic Multilevel method for simulation of non-isothermal single-phase flow in fractured geothermal reservoirs, in which the natural variable formulation is used to describe the thermodynamic state of the reservoir.

This study aims to compare the results and non-linear performance of the fine-scale and ADM methods between the molar and natural variable formulation for low-enthalpy fractured geothermal reservoirs. To this end, the molar formulation is implemented in the existing ADM simulation framework embedded in the DARSim2 reservoir simulator. A secondary aim is to extend this implementation to account for multiphase flow behavior (i.e. high-enthalpy) in fractured geothermal reservoirs. Heat production from both homogeneous and heterogeneous test cases with multiple different fracture networks is simulated using both a fine-scale and ADM approach, and by applying both primary variable formulations. The numerical results are presented in terms of pressure, temperature and enthalpy, and a comparison is made between both simulation approaches and both formulations. In addition, the performance of the various solution strategies is compared. Finally, the ADM results of a high-enthalpy fractured test case are presented and discussed in order to illustrate the successful extension towards simulating multiphase flow and heat transfer in fractured reservoirs.

This report is organized as follows. The governing equations and choice of primary variables are presented and discussed in chapter 2. The fine-scale discretization using pEDFM and the ADM simulation strategy for fractured reservoirs are covered in chapter 3. Test cases and their results are presented in chapter 4. The results are discussed in chapter 5, and subsequently concluded in chapter 6. Chapter 7 presents recommendations for future work. The fluid model for both formulations is presented in appendix A, and a full derivation of the governing equations is provided in appendix B.

2. Governing equations

The behavior of a geothermal reservoir under production stresses is described by the principles of conservation of mass and energy, under both single- and multiphase flow regimes. The equation for the conservation of mass yields the pressure solution, whereas the equation for the conservation of energy yields either the enthalpy or temperature solution depending on the primary variable formulation. This chapter presents the mass and energy conservation equations at continuum scale, and their extension for describing coupled matrix-fracture systems.

2.1. Conservation of mass

The equation for the conservation of mass in a pure water system assuming multi-phase flow conditions, i.e. single component water present in two possible phases, is written as (Faust and Mercer, 1979a; Wong et al., 2018)

$$\frac{\partial}{\partial t}\left(\phi \sum_{\alpha=1}^{n_p} \rho_\alpha S_\alpha\right) - \nabla \cdot \left(\sum_{\alpha=1}^{n_p} (\rho_\alpha \lambda_\alpha \cdot \nabla P)\right) = \sum_{\alpha=1}^{n_p} \rho_\alpha q_\alpha \tag{2.1}$$

where ϕ is the matrix porosity, ρ is density, S is saturation, P is pressure, and q is a source or sink term. The subscript α denotes a given fluid phase and n_p is the total number of phases. The phase mobility λ_α comprises both fluid phase and matrix properties as $\lambda_\alpha = K k_{r,\alpha}/\mu_\alpha$, where K, $k_{r,\alpha}$ and μ_α are matrix absolute permeability, fluid phase relative permeability and fluid phase viscosity, respectively. The saturation constraint requires summation of all phases to equal unity. Note that both the effects of capillary pressure and gravity are neglected in equation 2.1.

For coupled matrix-fracture systems, equation 2.1 is defined for both matrix and fracture domains separately. The coupling between both domains is ensured by defining additional source and/or sink terms describing the mass flux from matrix to fracture, and vice versa. The extended mass conservation equation reads (HosseiniMehr et al., 2019b)

$$\frac{\partial}{\partial t}\left(\phi^m \sum_{\alpha=1}^{n_p} \rho_\alpha S_\alpha\right) - \nabla \cdot \left(\sum_{\alpha=1}^{n_p} (\rho_\alpha \lambda_\alpha^m \cdot \nabla P^m)\right) = \sum_{\alpha=1}^{n_p} \rho_\alpha q_\alpha^{m,w} + \sum_{i=1}^{n_{frac}} \sum_{\alpha=1}^{n_p} \rho_\alpha Q_\alpha^{m,f_i} \tag{2.2}$$

on the rock matrix domain, denoted by the superscript m, and

$$\frac{\partial}{\partial t}\left(\phi^{f_i} \sum_{\alpha=1}^{n_p} \rho_\alpha S_\alpha\right) - \nabla \cdot \left(\sum_{\alpha=1}^{n_p} \left(\rho_\alpha \lambda_\alpha^{f_i} \cdot \nabla P^{f_i}\right)\right) =$$

$$\sum_{\alpha=1}^{n_p} \rho_\alpha q_\alpha^{f_i,w} + \sum_{\alpha=1}^{n_p} \rho_\alpha Q_\alpha^{f_i,m} + \sum_{j=1}^{n_{frac}} \left(\sum_{\alpha=1}^{n_p} \rho_\alpha Q_\alpha^{f_i,f_j}\right)_{j \neq i}, \tag{2.3}$$

$$\forall i \in \{1, \dots, n_{frac}\}$$

on the fracture domain and for an arbitrary fracture i, denoted by superscript f_i. The wells are denoted by the superscript w. Note that the fracture is always lower dimensional compared to the rock matrix. Here, $q^{m,w}$ and $q^{f_i,w}$ are source terms representing the volumetric flow rate of the wells w contributing to the matrix and fracture, respectively. These source terms are defined according to the Peaceman well model (Peaceman, 1978, as cited in HosseiniMehr et al., 2019b) as

$$q_\alpha^{m,w} = \frac{PI \cdot \lambda_\alpha^m \cdot (P^w - P^m)}{V}, \qquad q_\alpha^{f_i,w} = \frac{PI \cdot \lambda_\alpha^{f_i} \cdot \left(P^w - P^{f_i}\right)}{A} \tag{2.4}$$

in which PI is the productivity index of the well. Similar to the definition of the advective flux terms in equations 2.2 and 2.3, independent matrix and fracture mobilities are defined to ensure separation of the matrix and fracture permeabilities, i.e.

$$\lambda_\alpha^m = \frac{K^m k_{r,\alpha}}{\mu_\alpha}, \qquad \lambda_\alpha^{f_i} = \frac{K^f k_{r,\alpha}}{\mu_\alpha} \tag{2.5}$$

in which the fracture permeability is defined as (Hajibeygi et al., 2011)

$$K^f = \frac{a^2}{12} \tag{2.6}$$

in which a is the aperture of the fracture.

Furthermore, Q^{m,f_i} and $Q^{f_i,m}$ are source terms representing the advective flux exchange between matrix and the overlapping fracture, corresponding to the grid cells in which the overlap occurs. The advective flux exchange between two fractures on their intersecting elements is represented by Q^{f_i,f_j}. This means that the mentioned flux exchange terms are non-zero only where matrix-fracture overlap or fracture-fracture intersection occurs. These flux terms are defined as (HosseiniMehr et al., 2019b)

$$Q_\alpha^{m,f_i} = CI^{m,f_i} \cdot \lambda_\alpha^{m,f_i} \cdot \left(P^{f_i} - P^m\right) \tag{2.7}$$

$$Q_\alpha^{f_i,m} = CI^{f_i,m} \cdot \lambda_\alpha^{f_i,m} \cdot \left(P^m - P^{f_i}\right) \tag{2.8}$$

$$Q_\alpha^{f_i,f_j} = CI^{f_i,f_j} \cdot \lambda_\alpha^{f_i,f_j} \cdot \left(P^{f_j} - P^{f_i}\right) \tag{2.9}$$

where CI is the connectivity index between each two non-neighboring elements. These source terms describing flux exchange are defined such that they ensure mass conservation, i.e. $\iiint_V Q_\alpha^{m,f_i}\, dV = -\iint_A Q_\alpha^{f_i,m}\, dA$ and $\iint_A Q_\alpha^{f_i,f_j}\, dA = -\iint_A Q_\alpha^{f_j,f_i}\, dA$ (HosseiniMehr et al., 2019b). As an example, the connectivity index between the i-th matrix element and j-th fracture element is computed as

$$CI_{i,j} = \frac{A_{i,j}}{\langle d \rangle_{i,j}} \tag{2.10}$$

where $A_{i,j}$ is the area fraction of fracture cell j overlapping with matrix cell i and $\langle d \rangle_{i,j}$ is the average distance between these cells. Note that for fracture-fracture connectivities a lower dimensional formulation is applied to obtain the connectivity index.

Under the assumption of single-phase flow conditions, the saturation and relative permeability of the existing phase are equal to 1 and those of the absent phase are equal to zero (Faust and Mercer,1979a). This means that for the compressed water region, equations 2.2 and 2.3 reduce to

$$\frac{\partial}{\partial t}(\phi^m \rho_l) - \nabla \cdot (\rho_l \lambda_l^m \nabla P^m) = \rho_l q_l^{m,w} + \sum_{i=1}^{n_{frac}} \rho_l Q^{m,f_i} \tag{2.11}$$

on the rock matrix domain, and

$$\frac{\partial}{\partial t}\left(\phi^{f_i}\rho_l\right) - \nabla\cdot\left(\rho_l\lambda_l^{f_i}\nabla P^{f_i}\right) = \rho_l q_l^{f_i,w} + \rho_l Q^{f_i,m} + \sum_{j=1}^{n_{frac}}\left(\rho_l Q^{f_i,f_j}\right)_{j\neq i}, \qquad \forall i \in \{1,\dots,n_{frac}\} \tag{2.12}$$

on the fracture domain and for an arbitrary fracture i, respectively.

2.2. Conservation of energy

The equation for the conservation of energy in a pure water system assuming multi-phase flow conditions, i.e. single component water present in two possible phases, is written as (Faust and Mercer, 1979a; Wong et al., 2018)

$$\begin{gathered}\frac{\partial}{\partial t}\left[(1-\phi)\rho_r U_r + \phi\sum_{\alpha=1}^{n_p}\rho_\alpha U_\alpha S_\alpha\right] - \nabla\cdot\left(\sum_{\alpha=1}^{n_p}(\rho_\alpha h_\alpha \lambda_\alpha\cdot\nabla P)\right) \\ -\nabla\cdot\left(D_{eff}\cdot\nabla T\right) = \sum_{\alpha=1}^{n_p}\rho_\alpha h_\alpha q_\alpha\end{gathered} \tag{2.13}$$

where U is internal energy, h is enthalpy, T is temperature, and q is a source or sink term. The subscripts r and α denote rock and fluid phase properties, respectively, where n_p is the total number of (fluid) phases. Assuming local thermal equilibrium (Coats, 1977), an effective thermal conductivity D_{eff} is defined based on the weighted average between matrix and fluid phase conductivities, i.e.

$$D_{eff} = (1-\phi)D_r + \phi\sum_{\alpha=1}^{n_p} S_\alpha D_\alpha \tag{2.14}$$

where D_r and D_α are the rock and fluid phase thermal conductivities, respectively. Note that by neglecting the effects of gravity in equation (2.14), the occurrence of natural convection is consequently assumed absent.

For coupled matrix-fracture systems, equation 2.13 is defined for both matrix and fracture domains separately. The coupling between both domains is ensured by defining additional source and/or sink terms describing the energy flux from matrix to fracture, and vice versa. The extended energy conservation equation reads (HosseiniMehr et al., 2019b)

$$\begin{gathered}\frac{\partial}{\partial t}(\rho U)_t^m - \nabla\cdot\left(\sum_{\alpha=1}^{n_p}(\rho_\alpha h_\alpha \lambda_\alpha^m\cdot\nabla P^m)\right) - \nabla\cdot\left(D_{eff}^m\cdot\nabla T^m\right) = \\ \sum_{\alpha=1}^{n_p}\rho_\alpha h_\alpha q_\alpha^{m,w} + \sum_{i=1}^{n_{frac}}\sum_{\alpha=1}^{n_p}\rho_\alpha h_\alpha Q_\alpha^{m,f_i} + \sum_{i=1}^{n_{frac}} R^{m,f_i}\end{gathered} \tag{2.15}$$

on the rock matrix domain, denoted by the superscript m, and

$$\frac{\partial}{\partial t}(\rho U)_t^{f_i} - \nabla \cdot \left(\sum_{\alpha=1}^{n_p} \left(\rho_\alpha h_\alpha \lambda_\alpha^{f_i} \cdot \nabla P^{f_i} \right) \right) - \nabla \cdot \left(D_{eff}^{f_i} \cdot \nabla T^{f_i} \right) =$$

$$\sum_{\alpha=1}^{n_p} \rho_\alpha h_\alpha q_\alpha^{f_i,w} + \sum_{\alpha=1}^{n_p} \rho_\alpha h_\alpha Q_\alpha^{f_i,m} + \sum_{j=1}^{n_{frac}} \left(\sum_{\alpha=1}^{n_p} \rho_\alpha h_\alpha Q_\alpha^{f_i,f_j} \right)_{j \neq i} + R^{f_i,m} + \sum_{j=1}^{n_{frac}} \left(R^{f_i,f_j} \right)_{j \neq i}, \quad (2.16)$$

$$\forall i \in \{1, \dots, n_{frac}\}$$

on the fracture domain and for an arbitrary fracture i, denoted by superscript f_i. The wells are denoted by the superscript w. The total accumulation of internal energy in the system $(\rho U)_t$ and the effective thermal conductivity D_{eff} on an arbitrary domain β are defined as

$$(\rho U)_t^\beta = (1 - \phi^\beta)\rho_r U_r + \phi^\beta \sum_{\alpha=1}^{n_p} \rho_\alpha S_\alpha U_\alpha \quad (2.17)$$

and

$$D_{eff}^\beta = (1 - \phi^\beta) D_r + \phi^\beta \sum_{\alpha=1}^{n_p} S_\alpha D_\alpha \quad (2.18)$$

respectively. Equation 2.17 states that the total accumulation of energy is equal to the summation of the matrix and fluid phase internal energies.

The source terms $q_\alpha^{m,w}$, $q_\alpha^{f_i,w}$, Q_α^{m,f_i}, $Q_\alpha^{f_i,m}$ and $Q_\alpha^{f_i,f_j}$ in the extended energy conservation equation abide by the same definition as presented for the mass conservation equation. Note that the advective flux exchange Q is now considered a convective flux exchange as enthalpy is added in the formulation for the conservation of energy equation (HosseiniMehr et al., 2019b). Contrary to the mass conservation equation, a diffusive flux term is present in the energy conservation equation representing the transfer of heat by means of conduction. The conductive heat flux exchanges between matrix and the overlapping fracture R^{m,f_i} and $R^{f_i,m}$, and the flux exchange between two fractures on their intersecting elements R^{f_i,f_j}, are captured as source terms to the respective equations. The connectivity between two arbitrary domains α and β is defined as (HosseiniMehr et al., 2020)

$$R^{\alpha,\beta} = CI^{\alpha,\beta} \cdot D_{eff}^\alpha \cdot (T^\beta - T^\alpha) \quad (2.19)$$

Given the local thermal equilibrium assumption, the temperatures in the overlapping elements between both domains are assumed equal. The same goes for intersecting elements on the fracture domain. Therefore, the conductive connectivities can be ignored.

Under the assumption of single-phase flow conditions, the saturation and relative permeability of the existing phase are equal to 1 and those of the absent phase are equal to zero (Faust and Mercer,1979a). This means that for the compressed water region, equations 2.15 and 2.16 reduce to

$$\frac{\partial}{\partial t}(\rho U)_t^m - \nabla \cdot (\rho_l h_l \lambda_l^m \cdot \nabla P^m) - \nabla \cdot \left(D_{eff}^m \cdot \nabla T^m \right) =$$

$$\rho_l h_l q_l^{m,w} + \sum_{i=1}^{n_{frac}} \rho_l h_l Q^{m,f_i} + \sum_{i=1}^{n_{frac}} R^{m,f_i} \quad (2.20)$$

on the rock matrix domain, and

$$\frac{\partial}{\partial t}(\rho U)_t^{f_i} - \nabla \cdot \left(\rho_l h_l \lambda_l^{f_i} \cdot \nabla P^{f_i}\right) - \nabla \cdot \left(D_{eff}^{f_i} \cdot \nabla T^{f_i}\right) =$$

$$\rho_l h_l q_l^{f_i,w} + \rho_l h_l Q^{f_i,m} + \sum_{j=1}^{n_{frac}} \left(\rho_l h_l Q^{f_i,f_j}\right)_{j \neq i} + R^{f_i,m} + \sum_{j=1}^{n_{frac}} \left(R^{f_i,f_j}\right)_{j \neq i}, \qquad (2.21)$$

$$\forall i \in \{1, \dots, n_{frac}\}$$

on the fracture domain and for an arbitrary fracture i, respectively. The subscript l denotes the liquid phase and the total accumulation of energy in the system is defined as the summation of the matrix and fluid internal energies.

2.3. Primary variables

Following Gibb's phase rule, defining two independent primary variables is required to fully define the thermodynamic state of a system consisting of single-component water present in either the liquid or vapor phase (reference). To this end, two main non-linear formulations exist; 1) the natural formulation based on pressure P, temperature T and saturation S (Coats, 1980), and 2) the molar formulation based on pressure P and enthalpy H (Faust and Mercer, 1979a).

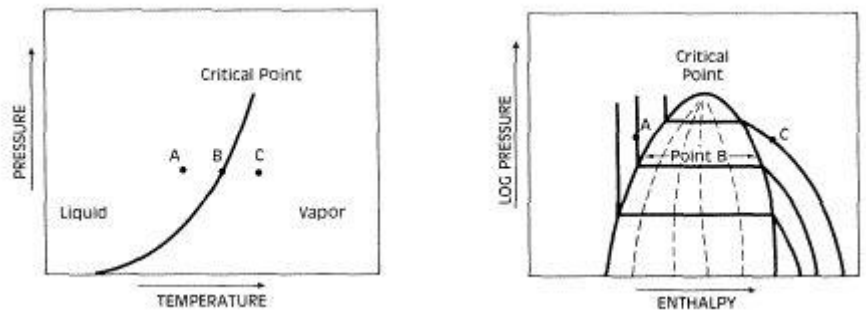

Figure 2.1: Pressure-temperature (left) and pressure-enthalpy (right) phase diagrams of pure water. Points A, B and C are located in the compressed water, two-phase and superheated-steam regions, respectively. From: Mercer and Faust, 1979a.

Use of the natural formulation poses difficulties when defining the thermodynamic state of the system under two-phase conditions. In a pressure-temperature phase diagram (figure 2.1, left), the two-phase region is defined by the vaporization curve as pressure and temperature are dependent under two-phase conditions, i.e. $P = P_{sat}(T)$. This means the secondary variables are now only dependent on pressure and an additional variable, i.e. saturation, is required in order to describe the thermodynamic state of the system (Wong et al., 2016). In the two-phase region, the primary variables may be switched to pressure and saturation in order to solve the two-phase system.

Using the molar formulation, the thermodynamic state of the system is uniquely defined under both single- and two-phase conditions as pressure and enthalpy remain independent in the two-phase region , and singularities in the constitutive equations at the critical point are avoided (Ingebritsen et al., 2006). In a pressure-enthalpy phase diagram (figure 2.1, right), the two-phase region is defined by an area bounded by the bubble- and dew-point curves. This means that the thermodynamic state of the system under two-phase conditions can be determined directly by comparing the total (or mixture)

enthalpy H of the system to the saturated phase enthalpies (Faust and Mercer, 1979a; Wong et al., 2018). This is illustrated as follows

$$Phase\ state = \begin{cases} Single-phase\ compressed\ water & h_w(P) \geq H \\ Two-phase\ mixture\ (water-steam) & h_w(P) < H < h_s(P) \\ Single-phase\ superheated\ steam & H \geq h_s(P) \end{cases} \quad (2.22)$$

The saturation of both water and steam can be calculated directly from the mixture enthalpy H using

$$S_w = \frac{\rho_s(h_s - H)}{H(\rho_w - \rho_s) - (h_w\rho_w - h_s\rho_s)}, \qquad S_s = 1 - S_w \quad (2.23)$$

As thermodynamic properties are often described as functions of pressure and temperature (Wong et al., 2016), the natural formulation may be preferred for simulations under single-phase conditions. The molar formulation requires the use of implicit relations in order to describe the properties as functions of pressure and enthalpy, which can affect the accuracy.

Both pressure and temperature (and saturation) are written explicitly in the mass and energy balance equations in (2.2, 2.3) and (2.15, 2.16). Although enthalpy is also explicitly written in the energy balance equation, it is actually the phase enthalpy (h_α) that this variable is referring to. Application of the molar formulation requires solving the energy balance equation for the total (or mixture) enthalpy H instead (Faust and Mercer, 1979a). In the single-phase region(s) the phase enthalpy is equal to the total enthalpy so that there is no apparent issue using the molar formulation. However, in the two-phase region, both phase- and total enthalpy are two different entities entirely. In order to express the energy balance equation in terms of total enthalpy, the internal energy is re-written according to

$$U = H - PV \quad (2.24)$$

which states that a change in internal energy in the system is equal to the amount of energy transferred to or from the system, i.e. enthalpy H, and an associated change in volume at constant pressure PV (Fletcher, 1993). Here, the PV-term represents the work done by compression of the system resulting from a constant external pressure and therefore refers to the effects of matrix compressibility. In terms of the internal energy of the matrix U_r, the work done by compression of the rock itself can be neglected as the rock is assumed non-deformable, i.e. $U_r = H_r$. As the matrix compressibility also affects the fluid volume, neglecting the work done by compression of the system is not that straightforward in terms of the internal energy of the fluid phase U_α. However, Faust and Mercer (1979a) state that the compressible work of the fluid volume as a result of an external pressure is negligible, except for fluid volumes of low liquid-phase saturation, i.e. $U_l = H = h_l$ in the compressed water region. This assumption is supported by the knowledge that the vapor phase (i.e. superheated steam) is highly compressible, especially compared to the low compressibility of the liquid phase. Note that $H = U + PV$ so that the work done by compression of the fluid as a result of the fluid pressure itself is taken into account (see Appendix B). This allows re-writing the energy balance equation in terms of the required total enthalpy H as

$$\begin{aligned} &\frac{\partial}{\partial t}[(1-\phi)\rho_r H_r + \phi\rho_t H] - \nabla\cdot(\rho_l h_l \lambda_l \cdot \nabla P) \\ &-\nabla\cdot\left(D_{eff}\cdot\nabla T\right) = \rho_l h_l q_l \end{aligned} \quad (2.25)$$

for the single-phase compressed water region in which $H = h_l$. In the two-phase region, the total enthalpy H is defined as

$$H = \frac{\rho_l S_l h_l + \rho_v S_v h_v}{\rho_t}, \qquad with\ \rho_t = \rho_l S_l + \rho_v S_v \tag{2.26}$$

where the subscripts l and v refer to the liquid and vapor phases, respectively.

In addition, Faust and Mercer (1979b) propose expanding the temperature gradient in the conductive flux in order to re-write the energy balance equation in terms of total enthalpy H. This approach is illustrated by

$$\nabla \cdot \left(D_{eff} \cdot \nabla T\right) = \nabla \cdot \left(D_{eff} \left(\frac{\partial T}{\partial P}\right)_H \cdot \nabla P + D_{eff} \left(\frac{\partial T}{\partial H}\right)_P \cdot \nabla H\right) \tag{2.27}$$

and applicable as temperature is treated as a function of both pressure and enthalpy (see Appendix A.2). Note that the derivative of temperature with respect to pressure at constant enthalpy is equal to the Joule-Thomson coefficient (Ingebritsen et al., 2006).

As the focus of this work is on the implementation of the molar formulation, the modified extended energy conservation equation now reads

$$\frac{\partial}{\partial t}(\rho H)_t^m - \nabla \cdot (\rho_l h_l \lambda_l^m \cdot \nabla P^m) - \nabla \cdot \left(D_{eff}^m \left(\frac{\partial T}{\partial P}\right)_H^m \cdot \nabla P^m + D_{eff}^m \left(\frac{\partial T}{\partial H}\right)_P^m \cdot \nabla H^m\right) = \rho_l h_l q_l^{m,w} + \sum_{i=1}^{n_{frac}} \rho_l h_l Q^{m,f_i} + \sum_{i=1}^{n_{frac}} R^{m,f_i} \tag{2.28}$$

on the rock matrix domain, denoted by the superscript m, and

$$\frac{\partial}{\partial t}(\rho H)_t^{f_i} - \nabla \cdot \left(\rho_l h_l \lambda_l^{f_i} \cdot \nabla P^{f_i}\right) - \nabla \cdot \left(D_{eff}^{f_i} \left(\frac{\partial T}{\partial P}\right)_H^{f_i} \cdot \nabla P^{f_i} + D_{eff}^{f_i} \left(\frac{\partial T}{\partial H}\right)_P^{f_i} \cdot \nabla H^{f_i}\right) = \rho_l h_l q_l^{f_i,w} + \rho_l h_l Q^{f_i,m} + \sum_{j=1}^{n_{frac}} \left(\rho_l h_l Q^{f_i,f_j}\right)_{j \neq i} + R^{f_i,m} + \sum_{j=1}^{n_{frac}} \left(R^{f_i,f_j}\right)_{j \neq i}, \tag{2.29}$$

$$\forall i \in \{1, \dots, n_{frac}\}$$

on the fracture domain and for an arbitrary fracture i, denoted by superscript f_i. Note that equations (2.28) and (2.29) are written in terms of the total accumulation of enthalpy in the system, which is defined as $(\rho H)_t^\beta = (1 - \phi^\beta)\rho_r H_r + \phi^\beta \rho_l H$ on an arbitrary domain β.

2.4. Constitutive equations

The mass and energy conservation equations presented in the previous section require additional constitutive equations in order to describe the model problem. The thermodynamic properties of pure water and steam are expressed by these constitutive equations, which, in turn, are functions of the primary variables. These correlations form the so-called fluid model, which is presented in appendix A for both the natural and molar variable formulations.

3. Fine-scale discretization and simulation approach

The fine-scale discretization of the mass and energy balances in terms of the molar variable formulation are presented in this chapter. As the methodology is largely similar, this chapter follows the description presented by HosseiniMehr, Vuik and Hajibeygi (2020) for the natural variable formulation. In the simulation approach the pEDFM and ADM methodologies are set forth.

The strong coupling between the mass and energy balance equations poses a significant challenge for convergence in geothermal simulations. The non-linearity in the (thermodynamic) equations of state for the fluid properties is the main reason for this strong coupling (Wong et al., 2017). Additionally, the mass and energy balance equations exhibit both parabolic and hyperbolic behavior, respectively, adding to the complexity of the model problem. In order to ensure numerical stability in the solution, a fully implicit approach is taken to solve the coupled fluid flow and heat transfer problem (Pruess et al., 1999; Zaydullin et al., 2014).

3.1. Fine-scale discrete system

The fine-scale discrete system is obtained using finite volume difference approximations in order to ensure conservation of mass and energy. The discretizations of the mass and energy balance equations are discussed separately.

3.1.1. Mass balance discretization

Discretization by means of the Finite Volume method yields the discrete form of the mass balance equation as

$$\frac{\Delta V}{\Delta t}(\phi^m \rho_l)_i - \Delta A\left(F^m_{mb}|_{i+\frac{1}{2}} - F^m_{mb}|_{i-\frac{1}{2}}\right) = \Delta V\left(\rho_l q_l^{m,w}\right)_i + \sum_{k=1}^{n_{frac}}\left(F_{mb}^{m,f_k}\right)_i \tag{3.1}$$

for a grid cell i in the rock matrix domain m. The subscript mb denotes the fluxes F pertaining to the mass balance equation. Note that the source term describing the advective flux exchange between matrix and overlapping fracture F_{mb}^{m,f_k} is not multiplied with ΔV. The physical dimensions between matrix and fracture grid cells are taken into account in the transmissibility between the overlapping elements, i.e. the connectivity index. The extended mass balance equation for a single fracture k is discretized as

$$\frac{\Delta V}{\Delta t}\left(\phi^{f_k}\rho_l\right)_i - \Delta A\left(F^{f_k}_{mb}\Big|_{i+\frac{1}{2}} - F^{f_k}_{mb}\Big|_{i-\frac{1}{2}}\right) = \Delta V\left(\rho_l q_l^{f_k,w}\right)_i + \left(F_{mb}^{f_k,m}\right)_i + \sum_{g=1}^{n_{frac}}\left(F_{mb}^{f_k,f_g}\right)_i \tag{3.2}$$

for a grid cell i in the fracture domain f.

The advective fluxes F^m_{mb} and $F^{f_k}_{mb}$ at the interfaces of their respective domains are approximated using the two-point flux approximation method (i.e. upwind differencing) resulting in

$$F^\beta_{mb}\Big|_{i+\frac{1}{2}} = \left(\rho_l \lambda_l^\beta\right)\frac{\partial P^\beta}{\partial x}\Big|_{i+\frac{1}{2}} = \begin{cases} \dfrac{\left(\frac{\rho_l}{\mu_l}\right)_{i+1} K^\beta_{i+\frac{1}{2}}(P_{i+1}-P_i)^\beta}{\Delta x} & if\ (P_{i+1}-P_i)^\beta > 0 \\ \dfrac{\left(\frac{\rho_l}{\mu_l}\right)_{i} K^\beta_{i+\frac{1}{2}}(P_{i+1}-P_i)^\beta}{\Delta x} & if\ (P_{i+1}-P_i)^\beta < 0 \end{cases} \tag{3.3}$$

and

$$F_{mb}^{\beta}\Big|_{i-\frac{1}{2}} = \left(\rho_l \lambda_l^{\beta}\right)\frac{\partial P^{\beta}}{\partial x}\Big|_{i+\frac{1}{2}} = \begin{cases} \dfrac{\left(\frac{\rho_l}{\mu_l}\right)_i K^{\beta}_{i-\frac{1}{2}}(P_i - P_{i-1})^{\beta}}{\Delta x} & if\ (P_i - P_{i-1})^{\beta} > 0 \\ \dfrac{\left(\frac{\rho_l}{\mu_l}\right)_{i-1} K^{\beta}_{i-\frac{1}{2}}(P_i - P_{i-1})^{\beta}}{\Delta x} & if\ (P_i - P_{i-1})^{\beta} < 0 \end{cases} \tag{3.4}$$

where the superscript β denotes either the matrix m or fracture f_k domain. $K^{\beta}_{i\pm\frac{1}{2}}$ is the harmonic average of the absolute matrix m or fracture f_k permeability defined at the interface between two neighboring grid cells.

The advective flux exchange terms between two overlapping grid cells originating from different domains α and β are obtained via EDFM formulation resulting in

$$F_{mb}^{\alpha,\beta} = -F_{mb}^{\beta,\alpha} = \left(\frac{\rho_l}{\mu_l}\right) T^{\alpha,\beta}\left(P^{\beta} - P^{\alpha}\right) \tag{3.5}$$

where α and β both represent either matrix m, fracture f_g or fracture f_k domains so that the above expression is valid for matrix-fracture, fracture-matrix and fracture-fracture (intersection) connectivities. The transmissibility between overlapping elements $T^{\alpha,\beta}$ is defined as

$$T^{\alpha,\beta} = CI^{\alpha,\beta} \cdot K^{\alpha,\beta} \tag{3.6}$$

where $CI^{\alpha,\beta}$ and $K^{\alpha,\beta}$ are the connectivity index and harmonically averaged permeability, respectively, between overlapping elements on both domains.

3.1.2. Energy balance discretization

Discretization by means of the Finite Volume method yields the discrete form of the energy balance equation as

$$\frac{\Delta V}{\Delta t}((\rho U)_t^m)_i - \Delta A\left(F_{eb}^m|_{i+\frac{1}{2}} - F_{eb}^m|_{i-\frac{1}{2}}\right) - \Delta A\left(G_{eb}^m|_{i+\frac{1}{2}} - G_{eb}^m|_{i-\frac{1}{2}}\right) = \Delta V\left(\rho_l h_l q_l^{m,w}\right)_i + \sum_{k=1}^{n_{frac}}\left(F_{eb}^{m,f_k}\right)_i \tag{3.7}$$

for a grid cell i in the rock matrix domain. The subscript eb denotes the fluxes pertaining to the energy balance equation. The extended energy balance equation for a single fracture k is discretized as

$$\frac{\Delta V}{\Delta t}\left((\rho U)_t^{f_k}\right)_i - \Delta A\left(F_{eb}^{f_k}\Big|_{i+\frac{1}{2}} - F_{eb}^{f_k}\Big|_{i-\frac{1}{2}}\right) - \Delta A\left(G_{eb}^{f_k}\Big|_{i+\frac{1}{2}} - G_{eb}^{f_k}\Big|_{i-\frac{1}{2}}\right) = \Delta V\left(\rho_l h_l q_l^{f_k,w}\right)_i + \sum_{k=1}^{n_{frac}}\left(F_{eb}^{f_k,m}\right)_i + \sum_{g=1}^{n_{frac}}\left(F_{eb}^{f_k,f_g}\right)_i \tag{3.8}$$

for a grid cell i in the fracture domain f.

The convective fluxes F_{eb}^m and $F_{eb}^{f_k}$ at the right and left interfaces of their respective domains are approximated using the two-point flux approximation method (i.e. upwind differencing) resulting in

$$F_{eb}^{\beta}\Big|_{i+\frac{1}{2}} = \left(\rho_l h_l \lambda_l^{\beta}\right)\frac{\partial P^{\beta}}{\partial x}\Big|_{i+\frac{1}{2}} = \begin{cases} \dfrac{\left(\frac{\rho_l h_l}{\mu_l}\right)_{i+1} K^{\beta}_{i+\frac{1}{2}}(P_{i+1}-P_i)^{\beta}}{\Delta x} & if\ (P_{i+1}-P_i)^{\beta} > 0 \\ \dfrac{\left(\frac{\rho_l h_l}{\mu_l}\right)_{i} K^{\beta}_{i+\frac{1}{2}}(P_{i+1}-P_i)^{\beta}}{\Delta x} & if\ (P_{i+1}-P_i)^{\beta} < 0 \end{cases} \tag{3.9}$$

and

$$F_{eb}^{\beta}\Big|_{i-\frac{1}{2}} = \left(\rho_l h_l \lambda_l^{\beta}\right)\frac{\partial P^{\beta}}{\partial x}\Big|_{i+\frac{1}{2}} = \begin{cases} \dfrac{\left(\frac{\rho_l h_l}{\mu_l}\right)_{i} K^{\beta}_{i-\frac{1}{2}}(P_{i}-P_{i-1})^{\beta}}{\Delta x} & if\ (P_{i}-P_{i-1})^{\beta} > 0 \\ \dfrac{\left(\frac{\rho_l h_l}{\mu_l}\right)_{i-1} K^{\beta}_{i-\frac{1}{2}}(P_{i}-P_{i-1})^{\beta}}{\Delta x} & if\ (P_{i}-P_{i-1})^{\beta} < 0 \end{cases} \tag{3.10}$$

where the superscript β denotes either the matrix m or fracture f_k domain. $K^{\beta}_{i\pm1/2}$ is the harmonic average of the absolute matrix m or fracture f_k permeability defined at the interface between two neighboring grid cells.

The conductive fluxes G_{eb}^{m} and $G_{eb}^{f_k}$ at the interfaces of their respective domains are approximated using central differences resulting in

$$G_{eb}^{\beta}\Big|_{i+\frac{1}{2}} = \left(D_{eff}\frac{\partial T}{\partial P}\Big|_H\right)^{\beta}\frac{\partial P^{\beta}}{\partial x}\Big|_{i+\frac{1}{2}} + \left(D_{eff}\frac{\partial T}{\partial H}\Big|_P\right)^{\beta}\frac{\partial H^{\beta}}{\partial x}\Big|_{i+\frac{1}{2}} = \frac{\left(\frac{\partial T}{\partial P}\Big|_H\right)^{\beta}_{i}\left(D^{\beta}_{eff}\right)_{i+\frac{1}{2}}(P_{i+1}-P_i)^{\beta}}{\Delta x} + \frac{\left(\frac{\partial T}{\partial H}\Big|_P\right)^{\beta}_{i}\left(D^{\beta}_{eff}\right)_{i+\frac{1}{2}}(H_{i+1}-H_i)^{\beta}}{\Delta x} \tag{3.11}$$

and

$$G_{eb}^{\beta}\Big|_{i-\frac{1}{2}} = \left(D_{eff}\frac{\partial T}{\partial P}\Big|_H\right)^{\beta}\frac{\partial P^{\beta}}{\partial x}\Big|_{i-\frac{1}{2}} + \left(D_{eff}\frac{\partial T}{\partial H}\Big|_P\right)^{\beta}\frac{\partial H^{\beta}}{\partial x}\Big|_{i-\frac{1}{2}} = \frac{\left(\frac{\partial T}{\partial P}\Big|_H\right)^{\beta}_{i}\left(D^{\beta}_{eff}\right)_{i-\frac{1}{2}}(P_{i}-P_{i-1})^{\beta}}{\Delta x} + \frac{\left(\frac{\partial T}{\partial H}\Big|_P\right)^{\beta}_{i}\left(D^{\beta}_{eff}\right)_{i-\frac{1}{2}}(H_{i}-H_{i-1})^{\beta}}{\Delta x} \tag{3.12}$$

where the superscript β denotes either the matrix m or fracture f_k domain.

The flux exchange terms between two overlapping grid cells originating from different domains α and β are obtained via EDFM formulation resulting in

$$F_{eb}^{\alpha,\beta} = -F_{eb}^{\beta,\alpha} = \left(\frac{\rho_l h_l}{\mu_l}\right)T_F^{\alpha,\beta}\left(P^{\beta}-P^{\alpha}\right) \tag{3.13}$$

for the convective flux exchanges. Here, α and β both represent either matrix m, fracture f_g or fracture f_k domains so that the above expression is valid for matrix-fracture, fracture-matrix and fracture-fracture (intersection) connectivities. The transmissibility between overlapping elements $T_F^{\alpha,\beta}$ is defined as

$$T_F^{\alpha,\beta} = CI^{\alpha,\beta}\cdot K^{\alpha,\beta} \tag{3.14}$$

where $CI^{\alpha,\beta}$ and $K^{\alpha,\beta}$ are the connectivity index and harmonically averaged permeability, respectively, between overlapping elements on both domains.

3.2. Simulation approach/solution strategy

The discrete (extended) mass and energy balance equations given by (3.1), (3.2), (3.7) and (3.8) have strong non-linear dependencies on the primary unknowns. This is independent of the formulation that is chosen (Wong et al., 2016). Secondary unknowns are non-linear functions of the primary unknowns as well.

In order to obtain a linear system of equations, the Newton-Raphson method (Aziz and Settari, 2002) is applied to linearize and approximate the dependent non-linear properties (secondary variables). For an arbitrary property $\xi(\theta,\eta)$ as a non-linear function of unknowns θ and η, Newton's method reads

$$\xi(\theta,\eta)^{n+1} \approx \xi(\theta,\eta)^{\nu+1} = \xi(\theta,\eta)^{\nu} + \left.\frac{\partial \xi(\theta,\eta)}{\partial(\theta,\eta)}\right|^{\nu} ((\theta,\eta)^{\nu+1} - (\theta,\eta)^{\nu}) \tag{3.15}$$

where the solution at the new Newton iteration level $\nu+1$ is used to approximate the value of the property at the next timestep $n+1$.

By subtracting the left-hand side from the right-hand side in equations (3.1), (3.2), (3.7) and (3.8) a residual form of the balance equations is obtained in which the residual r can be considered a property that is a non-linear function of the primary unknowns. The discrete residuals on the matrix domain are written as

$$\begin{aligned}(r_{mb}^{m})_i^{n+1} = \Delta V\left(\rho_l q_l^{m,w}\right)_i + \sum_{k=1}^{n_{frac}} \left(\frac{\rho_l}{\mu_l}\right)_i T^{m,f_k}\left(P_i^{f_k} - P_i^{m}\right) - \frac{\Delta V}{\Delta t}\left[(\phi^m \rho_l)_i^{n+1} - (\phi^m \rho_l)_i^{n}\right] \\ + \frac{\Delta A}{\Delta x}\left(\left(\frac{\rho_l}{\mu_l}\right)_i K_{i+\frac{1}{2}}^{m}(P_{i+1} - P_i)^m - \left(\frac{\rho_l}{\mu_l}\right)_{i-1} K_{i-\frac{1}{2}}^{m}(P_i - P_{i-1})^m\right)^{n+1}\end{aligned} \tag{3.16}$$

for the mass balance equation mb, and

$$\begin{aligned}(r_{eb}^{m})_i^{n+1} = \Delta V\left(\rho_l h_l q_l^{m,w}\right)_i + \sum_{k=1}^{n_{frac}} \left[\left(\frac{\rho_l h_l}{\mu_l}\right)_i T_F^{m,f_k}\left(P_i^{f_k} - P_i^{m}\right)\right] \\ - \frac{\Delta V}{\Delta t}\left[\left((1-\phi^m)\rho_r U_r + \phi^m \rho_l U_l\right)_i^{n+1} - \left((1-\phi^m)\rho_r U_r + \phi^m \rho_l U_l\right)_i^{n}\right] \\ + \frac{\Delta A}{\Delta x}\left(\left(\frac{\rho_l h_l}{\mu_l}\right)_i K_{i+\frac{1}{2}}^{m}(P_{i+1} - P_i)^m - \left(\frac{\rho_l h_l}{\mu_l}\right)_{i-1} K_{i-\frac{1}{2}}^{m}(P_i - P_{i-1})^m\right) \\ + \frac{\Delta A}{\Delta x}\left(\left(\left.\frac{\partial T}{\partial P}\right|_H\right)_i^{m} (D_{eff})_{i+\frac{1}{2}}^{m}(P_{i+1} - P_i)^m - \left(\left.\frac{\partial T}{\partial P}\right|_H\right)_i^{m} (D_{eff})_{i-\frac{1}{2}}^{m}(P_i - P_{i-1})^m\right) \\ + \frac{\Delta A}{\Delta x}\left(\left(\left.\frac{\partial T}{\partial H}\right|_P\right)_i^{m} (D_{eff})_{i+\frac{1}{2}}^{m}(H_{i+1} - H_i)^m - \left(\left.\frac{\partial T}{\partial H}\right|_P\right)_i^{m} (D_{eff})_{i-\frac{1}{2}}^{m}(H_i - H_{i-1})^m\right)\end{aligned} \tag{3.17}$$

for the energy balance equation eb. The residuals for the extended mass and energy balance equations on the fracture domain, i.e. $\left(r_{mb}^{f_k}\right)_i^{n+1}$ and $\left(r_{eb}^{f_k}\right)_i^{n+1}$, are obtained similarly to equations (3.16) and (3.17).

Substitution of the mass and energy balance residuals into Newton's method yields

$$\left(r_{mb}^{\beta}\right)^{n+1} \approx \left(r_{mb}^{\beta}\right)^{\nu+1} = \left(r_{mb}^{\beta}\right)^{\nu} + \left[\frac{\partial\left(r_{mb}^{\beta}\right)}{\partial P}\right]^{\nu} \delta P^{\nu+1} + \left[\frac{\partial\left(r_{mb}^{\beta}\right)}{\partial H}\right]^{\nu} \delta H^{\nu+1} \tag{3.18}$$

and

$$\left(r_{eb}^{\beta}\right)^{n+1} \approx \left(r_{eb}^{\beta}\right)^{\nu+1} = \left(r_{eb}^{\beta}\right)^{\nu} + \left[\frac{\partial\left(r_{eb}^{\beta}\right)}{\partial P}\right]^{\nu} \delta P^{\nu+1} + \left[\frac{\partial\left(r_{eb}^{\beta}\right)}{\partial H}\right]^{\nu} \delta H^{\nu+1} \tag{3.19}$$

respectively, where $\delta P^{\nu+1} = P^{\nu+1} - P^{\nu}$ and $\delta H^{\nu+1} = H^{\nu+1} - H^{\nu}$, and the superscript β denotes either the matrix or fracture domain. Note that application of the molar formulation for the primary variables yields the use of pressure P and enthalpy H as the primary unknowns.

The fully coupled linear system of equations then reads

$$\begin{pmatrix} \begin{pmatrix} J_{mb,P}^{m,m} & J_{mb,P}^{m,f} \\ J_{mb,P}^{f,m} & J_{mb,P}^{f,f} \end{pmatrix} & \begin{pmatrix} J_{mb,H}^{m,m} & J_{mb,H}^{m,f} \\ J_{mb,H}^{f,m} & J_{mb,H}^{f,f} \end{pmatrix} \\ \begin{pmatrix} J_{eb,P}^{m,m} & J_{eb,P}^{m,f} \\ J_{eb,P}^{f,m} & J_{eb,P}^{f,f} \end{pmatrix} & \begin{pmatrix} J_{eb,H}^{m,m} & J_{eb,H}^{m,f} \\ J_{eb,H}^{f,m} & J_{eb,H}^{f,f} \end{pmatrix} \end{pmatrix}^{\nu} \begin{pmatrix} \delta P^{m} \\ \delta P^{f} \\ \delta H^{m} \\ \delta H^{f} \end{pmatrix}^{\nu+1} = - \begin{pmatrix} r_{mb}^{m} \\ r_{mb}^{f} \\ r_{eb}^{m} \\ r_{eb}^{f} \end{pmatrix}^{\nu} \tag{3.20}$$

which can be simplified to

$$J^{\nu} \delta x^{\nu+1} = -r^{\nu} \tag{3.21}$$

where J^{ν} is the Jacobian matrix. Each block $J_{e,\theta}^{\alpha,\alpha}$ of the Jacobian matrix represents the derivatives of balance equation e with respect to primary unknown θ on the domain α. The matrix-matrix and fracture-fracture connectivities are taken into account in these blocks. The blocks $J_{e,\theta}^{\alpha,\beta}$ represent the derivatives of the flux exchange terms between domains α and β. The matrix-fracture, fracture-matrix and fracture-fracture (intersection) connectivities are thus taken into account in these blocks (HosseiniMehr et al., 2020).

The solution to the above linear system $\delta x^{\nu+1}$ is used to obtain $r^{\nu+1}$, which is accepted as the correct approximation of r^{n+1} when the following conditions are met at a given iteration level (HosseiniMehr et al., 2020)

$$\frac{\left\|r_{mb}^{\nu+1}\right\|_2}{\left\|r_{mb}^{0}\right\|_2} < \epsilon_{mb} \ \wedge \ \frac{\left\|r_{eb}^{\nu+1}\right\|_2}{\left\|r_{eb}^{0}\right\|_2} < \epsilon_{eb} \ \wedge \ \frac{\|\delta P^{\nu+1}\|_2}{\|P^{\nu}\|_2} < \epsilon_P \ \wedge \ \frac{\|\delta H^{\nu+1}\|_2}{\|H^{\nu}\|_2} < \epsilon_H \tag{3.22}$$

where r_e^0 is the initial residual of balance equation e at time-step n and ϵ is a user-defined threshold. These conditions imply the following: 1) when the residual norm has decreased by ϵ compared to the

initial residual norm, the solution is accepted, and 2) when the change in primary variables compared to the value of the primary variables at the previous iteration is smaller than ϵ, the solution is accepted. Note that all four conditions have to be met before the solution is accepted, and that the above conditions are more physical compared to the absolute $\|r_{mb}\|_2 < \epsilon_{mb} \wedge \|r_{eb}\|_2 < \epsilon_{eb}$ conditions as the difference in the magnitude of the units between mass and energy balance equations is accounted for.

3.3. Extension to pEDFM

In order to correct for the parallel transmissibilities embedded in the EDFM method, the matrix-matrix, fracture-matrix and fracture-fracture connectivities are modified in those regions where overlap occurs. This modification eliminates the parallel transmissibilities such that the pEDFM method applies to any type of fracture conductivity, i.e. both highly-conductive and acting as a barrier to flow (Tene et al., 2017). By disconnecting the connections between neighboring matrix cells, the flux can only occur via one route, i.e. through matrix-fracture-matrix.

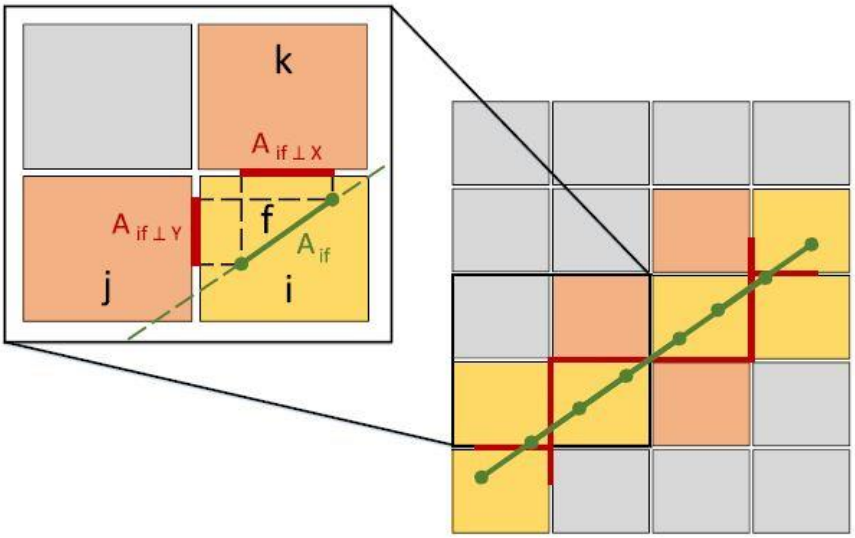

Figure 3.1: Illustration of pEDFM method assuming a 2D matrix on a structured grid and a 1D overlapping fracture. Overlapping cells are highlighted in yellow. From: Tene et al., 2017.

Figure 3.1 shows a fracture element f overlapping a matrix grid cell i. The area fraction of the overlapping fracture element A_{if} is projected onto the interfaces that connect the overlapped matrix cell i to its neighboring matrix cells j and k (Tene et al., 2017). The area fractions $A_{if\perp x}$ and $A_{if\perp y}$ of the projection are located on the interfaces and are defined as

$$A_{if\perp x} = A_{if} \times \cos(\gamma_{fx}), \qquad A_{if\perp y} = A_{if} \times \cos(\gamma_{fy}) \tag{3.23}$$

where γ_{fx} and γ_{fy} are the angles between the fracture element f and the interfaces to the neighboring matrix cells in k and j, respectively.

The transmissibility describing the connectivity between overlapped matrix grid cell i and fracture element f remains unchanged from the original EDFM formulation (Tene et al., 2017). The transmissibilities on the interfaces between the overlapped matrix cell i and its neighboring matrix grid cells j and k are modified by subtracting the respective projection area fractions from the cross-sectional areas of the matrix interfaces A_{ij} and A_{ik}, and are given by

$$T_{ij} = \frac{A_{ij} - A_{if\perp y}}{\Delta y}\lambda_{ij}, \qquad T_{ik} = \frac{A_{ik} - A_{if\perp x}}{\Delta x}\lambda_{ik} \tag{3.24}$$

where λ_{ij} and λ_{ik} are the effective fluid mobilities between the corresponding cells. Note that the projection area fractions are used to define separate connections between the fracture element f and the neighboring matrix cells j and k

$$T_{jf} = \frac{A_{if\perp y}}{\langle d \rangle_{jf}}\lambda_{jf}, \qquad T_{kf} = \frac{A_{if\perp x}}{\langle d \rangle_{kf}}\lambda_{kf} \tag{3.25}$$

where $\langle d \rangle_{jf}$ and $\langle d \rangle_{kf}$ are the average distances between the fracture element f and matrix cells j and k, respectively. Note that in terms of conduction elimination of the parallel transmissibilities is not required (HosseiniMehr et al., 2020). As fractures cannot pose as barriers to conduction, the EDFM formulation is sufficient.

The implementation of the extension is simplified by obtaining the modified transmissibilities through multiplication of a coefficient α that represents the projected fracture element area as a fraction of the total matrix interface area. Note that $\alpha = 1$ in most cases, as the projections of multiple overlapping fracture elements will cover the entire matrix interface. This will result in zero matrix-matrix transmissibility, and therefore effectively eliminate the parallel transmissibilities originally embedded in the EDFM method (HosseiniMehr et al., 2020).

3.4. Algebraic Dynamic Multilevel (ADM) method

At each time-step, before the Newton iterations, a reduced linear system is constructed algebraically on a dynamic multilevel grid resolution. This linear system is reduced from the fine-scale fully-implicit linear system of equation (3.20). In order to obtain the dynamic multilevel grid, a set of N_m^l and $N_{f_i}^l$ hierarchically nested grids are imposed on the matrix m and fracture f_i (HosseiniMehr et al., 2020). The coarsening level is denoted by l, with $l = 0$ being the fine-scale resolution. The coarsening ratio, i.e. the ratio between the resolutions of level l and $l-1$, for an arbitrary domain β is defined as

$$\gamma_\beta^l = \frac{N_\beta^{l-1}}{N_\beta^l}, \qquad with\ l = 1, \dots, n_c \tag{3.26}$$

where n_c is the number of coarsening levels. Although the coarsening ratio is constant over the different coarsening levels, it is defined separately for both domains, and for each fracture, to provide practical flexibility.

The ADM grid is thus an ensemble of grids at different resolutions. In order to move from the fine-scale resolution to this dynamic multilevel resolution, and vice versa, the ADM method employs dynamic restriction $\hat{R}$ and prolongation $\hat{P}$ operators. These dynamic operators consist of a series of static restriction R and prolongation P operators that apply to a single level of coarsening and were originally defined in the (multilevel) multiscale method (Wang et al., 2014; Tene et al., 2015). The static restriction operator R is defined in order to move to a coarse(r)-scale resolution, i.e. R_l^{l-1} maps the solution at level $l-1$ to level l. The restriction operator therefore represents the integration of the mass and energy balance equations over the coarse(r)-scale control volumes and effectively discretizes the equations on the coarse(r) grid. In order to ensure conservative solutions at each level, a finite-volume restriction operator is applied (Cusini et al., 2016). An arbitrary entry (i, j) of the restriction operator R_l^{l-1} reads

$$R_l^{l-1}(i,j) = \begin{cases} 1 & if\ cell\ j\ is\ inside\ coarser\ cell\ i \\ 0 & otherwise \end{cases} \tag{3.27}$$

The prolongation operator P is comprised of so-called basis functions and is defined in order to move to a fine(r)-scale resolution by means of interpolation, i.e. P_{l-1}^{l} maps the solution at level l to level $l-1$. These basis functions represent local solutions of the fine-scale system on the (dual) coarse-scale grid (Lee et al., 2008). Invoking the dynamic restriction and prolongation operators, the fully-implicit system of equations for the ADM method is written as

$$\left(\hat{R}\, J_0\, \hat{P}\right)\delta\hat{x}_{ADM} = -\hat{R}\, r_0 \tag{3.28}$$

in which $\hat{R} = R_l^{l-1}, \dots, R_1^0$ and $\hat{P} = P_0^1 \dots P_{l-1}^{l}$. The ADM Jacobian matrix $J_{ADM} = \left(\hat{R}\, J_0\, \hat{P}\right)$ and the residual $r_{ADM} = \hat{R}\, r_0$. By prolonging the ADM solution $\delta\hat{x}_{ADM}$ an approximate solution at the fine-scale resolution $\delta x_0'$ is obtained (HosseiniMehr et al., 2020), namely

$$\delta x_0 \approx \delta x_0' = \left[\hat{P}_0^1 \dots \hat{P}_{l-1}^{l}\right]\delta\hat{x}_{ADM} \tag{3.29}$$

in which δx_0 is the reference fine-scale solution.

3.4.1. Multilevel Multiscale basis functions

Different basis functions are considered for each of the primary variables due to the parabolic and hyperbolic nature of the mass and energy balance equations, respectively (Cusini et al., 2016). The pressure prolongation operator $(P_P)_{l-1}^{l}$ uses multilevel multiscale basis functions as interpolator, whereas the enthalpy prolongation operator $(P_H)_{l-1}^{l}$ uses constant basis functions such that $(P_H)_{l-1}^{l} = \left(R_l^{l-1}\right)^T$ (where the superscript T is the transpose operator).

Both multilevel multiscale and constant basis functions are defined at each coarsening level. The difference between these two types is that the multilevel multiscale basis functions require solving a local system and the constant basis functions assume the solution to the local system is a constant (Cusini et al., 2016; HosseiniMehr et al., 2020). As a consequence, the multilevel multiscale basis functions allow for a fully-coupled approach, in which both the matrix and fracture domains will affect the local solution on the (dual) coarse grid cell in which the overlap occurs. The local solutions are obtained algebraically by converting the two-point flux approximation (TPFA) connectivities of the fine-scale system to multi-point flux approximation (MPFA) connectivities at coarse-scale systems for each coarsening level l. This means that when multiple coarsening levels are considered, before constructing the coarse-scale system at level l, the system at level $l-1$ is (again) reduced to the TPFA scheme through (HosseiniMehr et al., 2020)

$$[A^{l-1}]_{TPFA} = OP_{TPFA}\,[A^{l-1}]_{MPFA} \tag{3.30}$$

where the operator OP_{TPFA} removes the MPFA components from the entries of the coarse-scale system matrix. This procedure is performed independently on each medium.

Meanwhile, the constant basis functions result in a decoupled approach in which both domains do not affect the local solution of one another. Furthermore, constant basis functions capture the fine-scale heterogeneity of the model problem to a lesser extent as the local solution on the coarse grid has a constant value. This approach is similar to the general upscaling method used in reservoir simulation and does yield a (minor) loss in accuracy (Cusini et al., 2016; HosseiniMehr et al., 2020).

3.4.2. Selection of the grid resolution

The dynamic grid resolution is obtained by a user defined grid selection criterion as a front-tracking technique (HosseiniMehr et al., 2020). The ADM grid at each time-step n is selected based on the solution at the previous time-step $n-1$. Between two neighboring cells at coarsening level l, the selection is conditioned by the maximum change in value of a given variable at level $l-1$. As an example, the temperature difference ΔT_{IJ} is obtained as

$$\Delta T_{IJ} = \max\left(\left|T_i - T_j\right|\right) \qquad \forall i \in \Omega_l^I \; and \; \forall j \in \Omega_l^J \tag{3.31}$$

where the indices i and j refer to the grid cells at level $l-1$ present in the neighboring coarse grid cells I and J at coarsening level l, respectively. Note that the grid selection criterion can be applied independently to both matrix and fracture domains. The grid cells in the vicinity of the wells are fixed at fine-scale resolution to ensure the effect of the source term fluxes is captured accurately (Cusini et al., 2016).

4. Results

Algebraic dynamic multilevel (ADM) and fine-scale simulation results are presented for a number of different test cases. In addition, a comparison between the results originating from the molar and natural formulations is presented, as well as a comparison of the performance of both formulations. The final section presents a high-enthalpy fractured test case as a multiphase simulation example illustrative of the extended implementation of the molar formulation.

An identical reservoir geometry and production strategy is applied in all test cases. The initial reservoir pressure is also identical for all test cases. A schematic overview of the reservoir geometry and production strategy is presented in figure 4.1. A subdivision is made in terms of geological realization of the reservoir. The initial reservoir temperature, rock matrix properties and permeability field are chosen such that the two realizations represent the geothermal fields of Middenmeer in the Netherlands and Soultz-sous-Forêts in France (Marelis, 2017). Note that the geothermal fluid is assumed identical, i.e. pure water, between both geothermal fields. The rock matrix properties of both geothermal fields are presented in table 4.1.

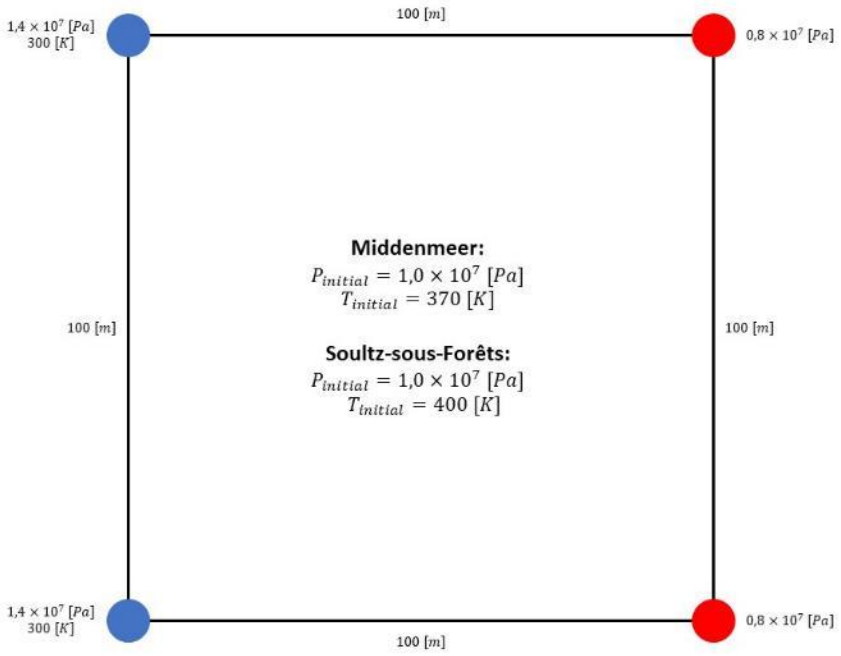

Figure 4.1: Schematic overview of the reservoir geometry and production strategy applied in all test cases. Two injection wells are located on the left corners of the domain with an injection temperature of $300\ [K]$*. Two production wells are located on the right corners of the domain, and the initial reservoir temperature is indicated for both geothermal fields under consideration.*

	Middenmeer	Soutlz-sous-Forêts
Density $[kg/m^3]$	2600	2600
Specific heat capacity $[J/kg/K]$	830	850
Thermal conductivity $[W/m/K]$	2.9	3
Porosity $[-]$	0.2	0.2

Table 4.1: Rock matrix properties of the Middenmeer and Soultz-sous-Forêts geothermal fiels. Note that the geothermal fluid is assumed identical, i.e. pure water, and therefore holds properties dependent on (initial) pressure and temperature distributions.

The permeability field of the Soultz-sous-Forêts geothermal field is assumed isotropic and homogeneous as the reservoir is located in granitic rock. The reservoir in the Middenmeer geothermal field is located in a sandstone layer and therefore the permeability field is assumed isotropic and heterogeneous. Note that the effect of anisotropic permeability is left out of consideration entirely. Both permeability fields are presented in figure 4.2.

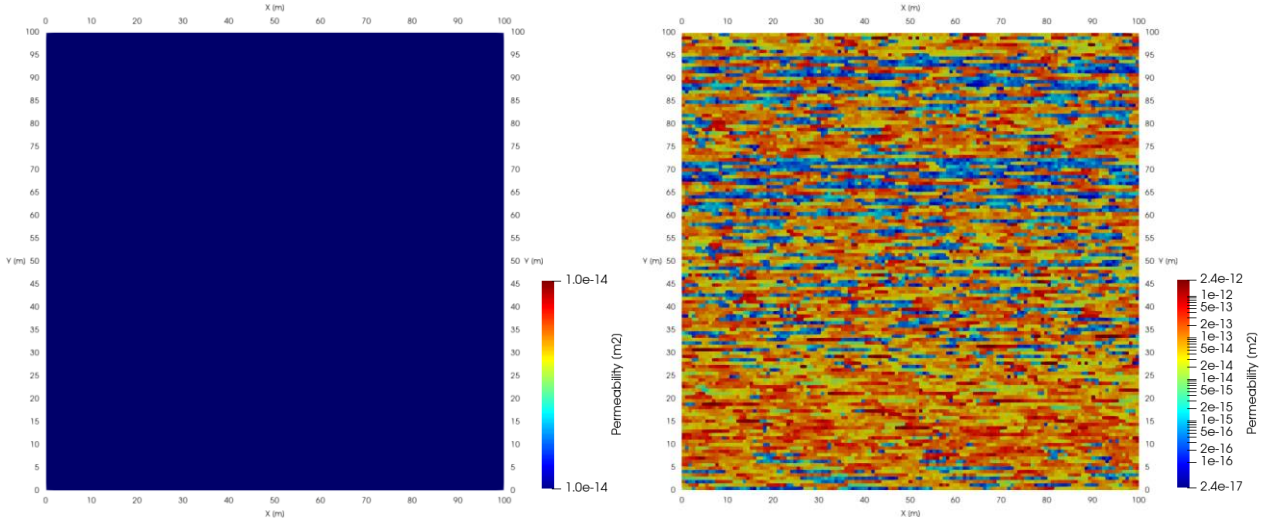

Figure 4.2: Assumed permeability fields of the Soultz-sous-Forêts (left) and Middenmeer (right) geothermal fields. Note that both permeability realizations are assumed isotropic.

Three different fracture network realizations are considered for both geothermal fields: 1) no fractures, 2) a fracture network consisting of 15 fractures and 3) a fracture network consisting of 30 fractures. Both fracture networks include both highly conductive fractures as well as fractures acting as a barrier to flow. The two fracture network realizations, and their respective conductivities (i.e. permeabilities), are presented in figure 4.3.

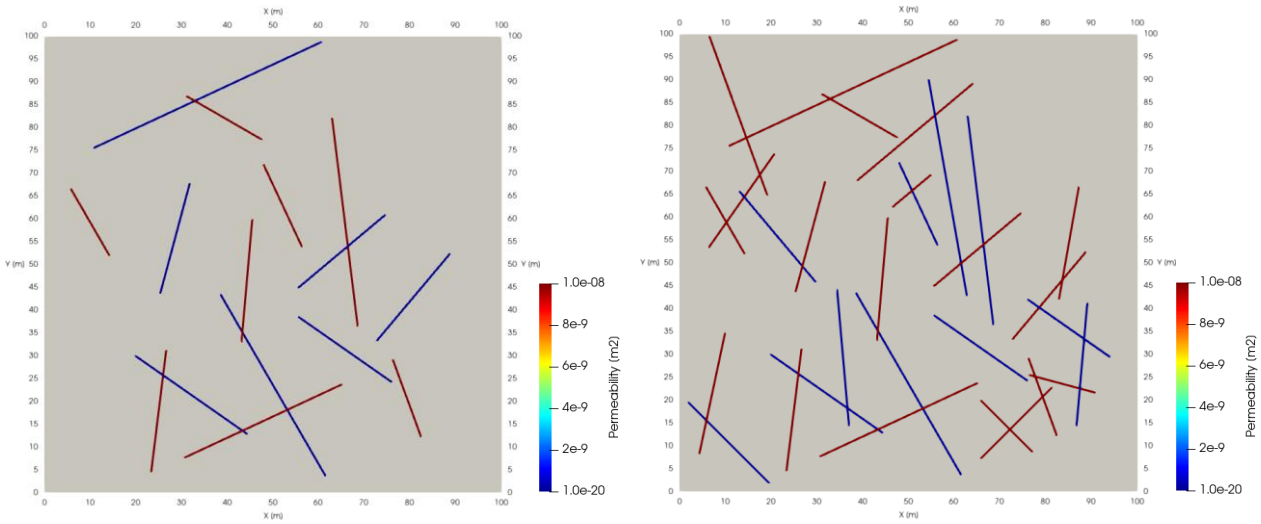

Figure 4.3: Fracture network realizations consisting of 15 (left) and 30 (right) fractures. Both highly conductive ($k_f = 1 \times 10^{-8}$ $[m^2]$) fractures as well as flow-barriers ($k_f = 1 \times 10^{-20}$ $[m^2]$) are considered present.

The simulation parameters, convergence tolerances and ADM parameters are presented in table 4.2.

	Value
Simulation time $[\boldsymbol{days}]$	2000
Maximum time-step $[\boldsymbol{days}]$	30
Maximum number of iterations $[-]$	10
Residual tolerances $\boldsymbol{\epsilon_{mb,eb}}$ *(eqn. 3.22)*	1×10^{-4}
Solution tolerances $\boldsymbol{\epsilon_{P,H,T}}$ *(eqn. 3.22)*	1×10^{-4}
ADM levels $\boldsymbol{l}$	2
ADM coarsening ratio $\boldsymbol{\gamma^l}$ *(eqn. 3.26)*	3
ADM threshold $\boldsymbol{\Delta T}$ $[\boldsymbol{K}]$ *(eqn. 3.31)*	20

Table 4.2: Simulation parameters and tolerances for all test cases.

Note that the ADM threshold refers to the grid selection criterion discussed in section 3.4.2.

The ADM results are compared to the fine-scale results in order to obtain an estimate of the accuracy of the ADM solution. The error of the ADM method e_{ADM} is defined as

$$e_{ADM} = \frac{\|x_{ADM} - x_{FS}\|_2}{\|x_{FS}\|_2} \tag{4.1}$$

where $\|x_{ADM}\|_2$ and $\|x_{FS}\|_2$ are the ADM and fine-scale (FS) solutions, respectively, of a given variable x (i.e. pressure, temperature or enthalpy). The percentage of active grid cells is presented in the results as AC.

In order to compare the results between the molar and natural formulations, a so-called formulation error e_f is defined that represents the relative difference between the numerical solutions obtained from both formulations. The formulation error is given by

$$e_f = \frac{\|x_{P-H} - x_{P-T}\|_2}{\|x_{P-T}\|_2} \tag{4.2}$$

where $\|x_{P-H}\|_2$ and $\|x_{P-T}\|_2$ are the second error norms of a given variable x using the molar and natural formulation, respectively.

4.1. Soultz-sous-Forêts – Realization 1

The first realization of the Soultz-sous-Forêts geothermal field is one without the presence of a fracture network. The fine-scale simulation results of the reservoir pressure are presented in figure 4.4. The pressure solution using the molar formulation (i.e. P, H) is presented in subfigures (a), (b) and (c), and the pressure solution using the natural formulation (i.e. P, T) is presented in subfigures (d), (e) and (f) for simulation times of 400, 1000 and 2000 [days], respectively. Subfigures (g), (h) and (i) show the error e_f between the solutions of both formulations at the respective simulation times.

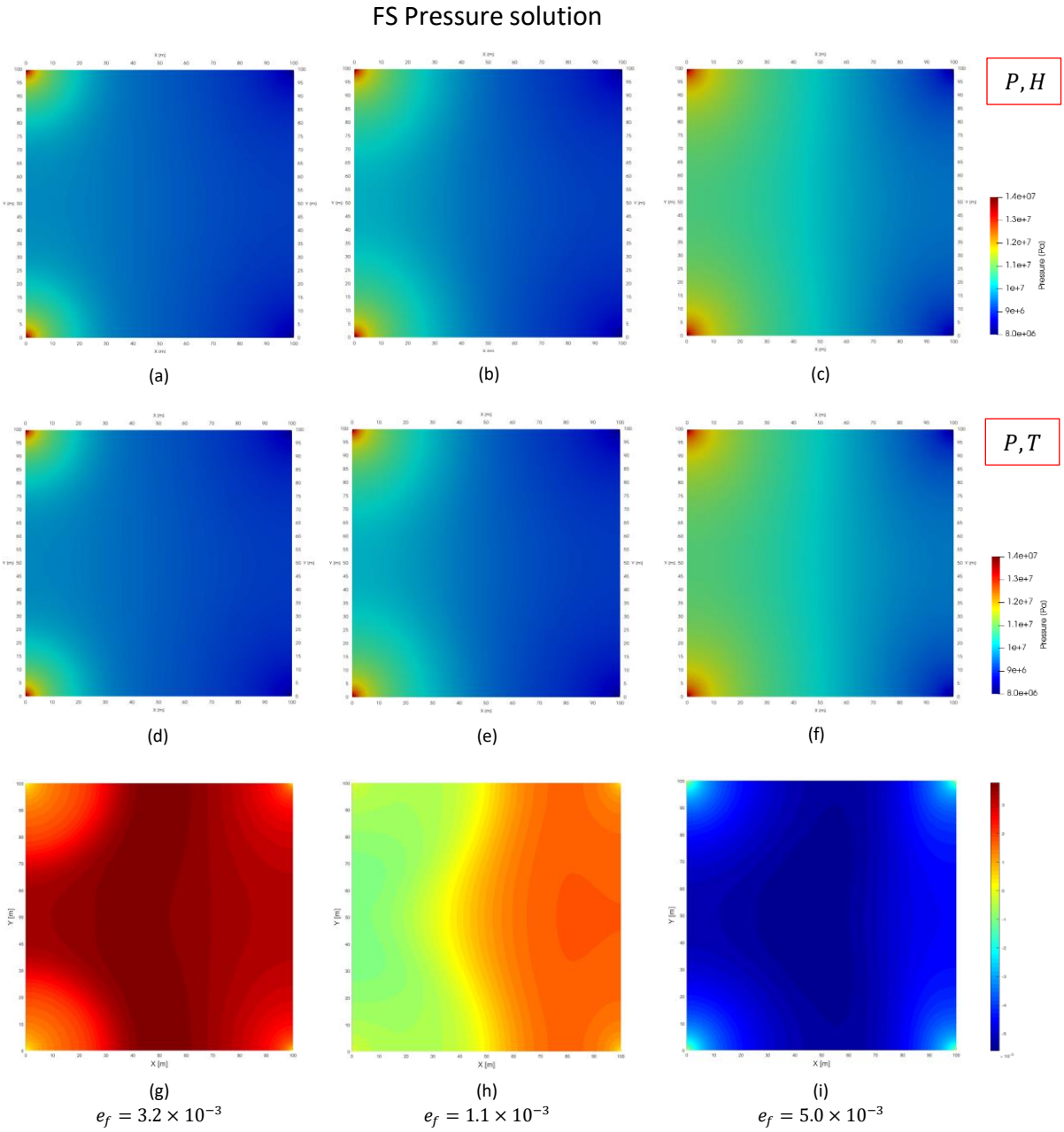

Figure 4.4: Fine-scale simulation results of reservoir pressure for realization 1 of the Soultz-sous-Forêts geothermal field. The first and second rows show the results using the molar and natural formulation, respectively. The third row shows the error between the results of both formulations. Column wise, the simulation time increases from 400 to 1000 to 2000 [days]. The formulation error e_f indicates the relative difference between the solutions obtained from both formulations.

The fine-scale simulation results of the reservoir temperature are presented in figure 4.5.

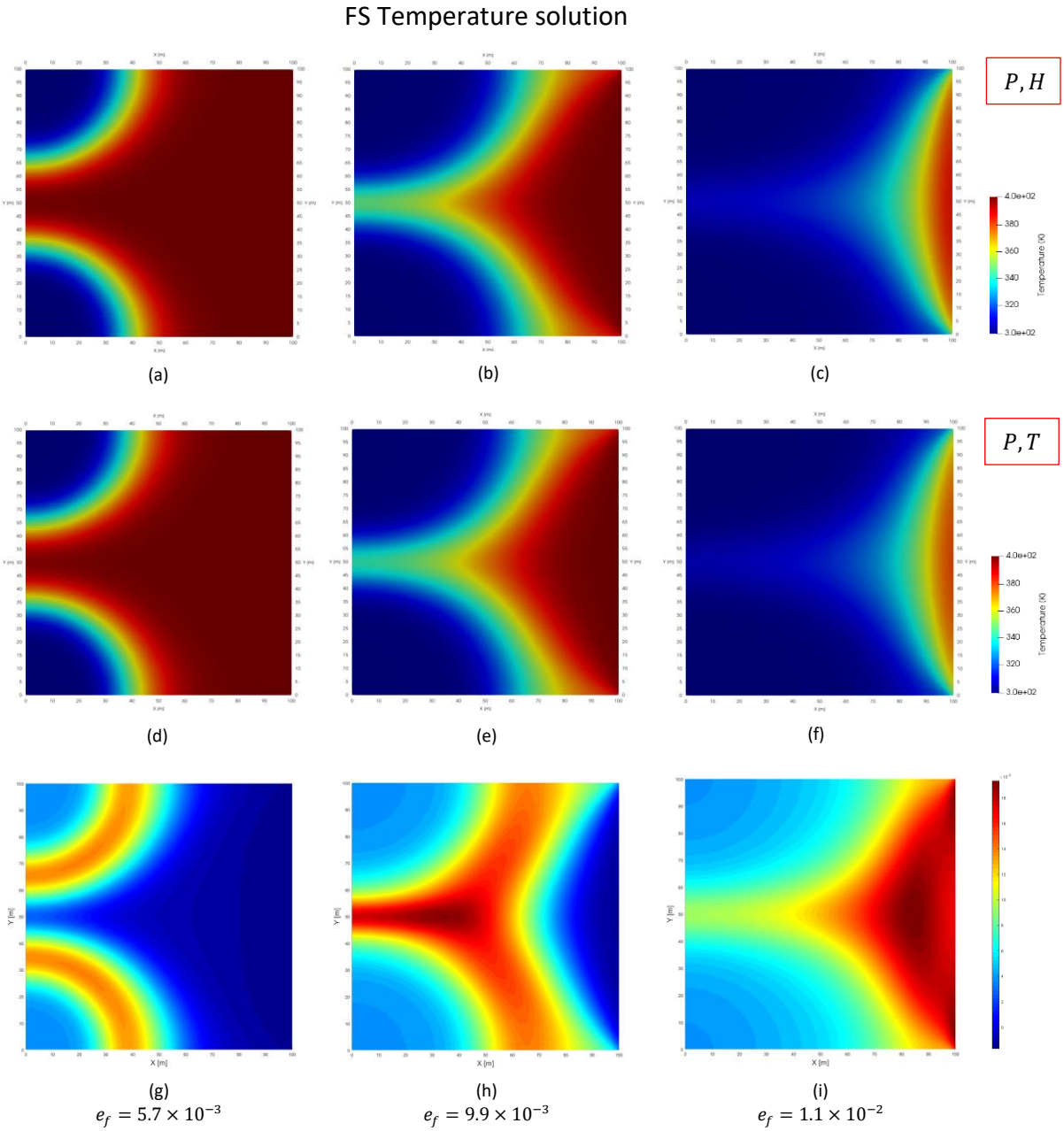

Figure 4.5: Fine-scale simulation results of reservoir temperature for realization 1 of the Soultz-sous-Forêts geothermal field. The first and second rows show the results using the molar and natural formulation, respectively. The third row shows the error between the results of both formulations. Column wise, the simulation time increases from 400 to 1000 to 2000 [days]. The formulation error e_f indicates the relative difference between the solutions obtained from both formulations.

The fine-scale simulation results of the reservoir enthalpy are presented in figure 4.6.

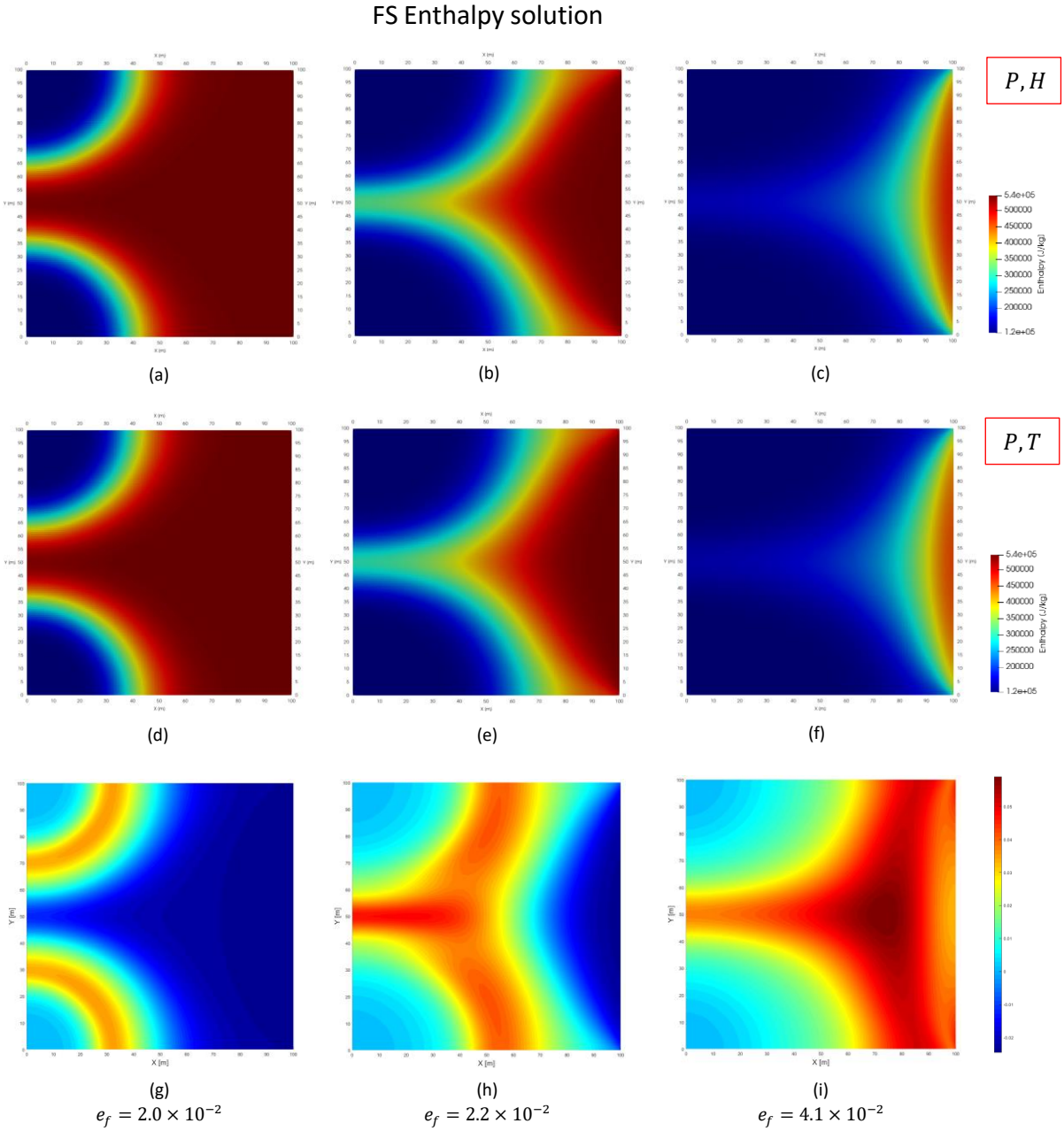

Figure 4.6: Fine-scale simulation results of reservoir enthalpy for realization 1 of the Soultz-sous-Forêts geothermal field. The first and second rows show the results using the molar and natural formulation, respectively. The third row shows the error between the results of both formulations. Column wise, the simulation time increases from 400 to 1000 to 2000 [days]. The formulation error e_f indicates the relative difference between the solutions obtained from both formulations.

The algebraic dynamic multilevel (ADM) simulation results of the reservoir pressure are presented in figure 4.7.

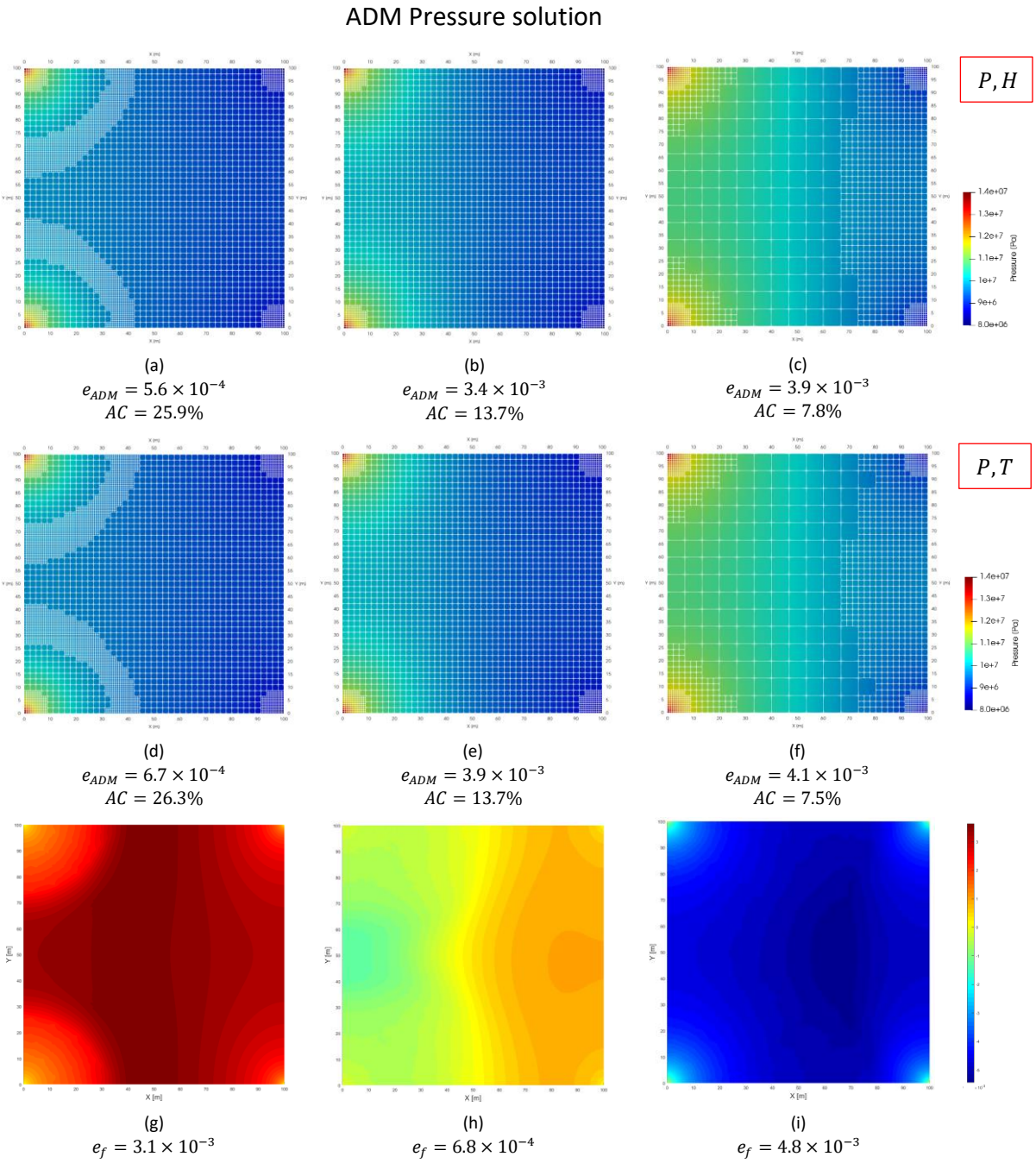

Figure 4.7: ADM simulation results of reservoir pressure for realization 1 of the Soultz-sous-Forêts geothermal field. The first and second rows show the results using the molar and natural formulation, respectively. The third row shows the error between the results of both formulations. Column wise, the simulation time increases from 400 to 1000 to 2000 [days]. The formulation error e_f indicates the relative difference between the solutions obtained from both formulations.

The algebraic dynamic multilevel (ADM) simulation results of the reservoir temperature are presented in figure 4.8.

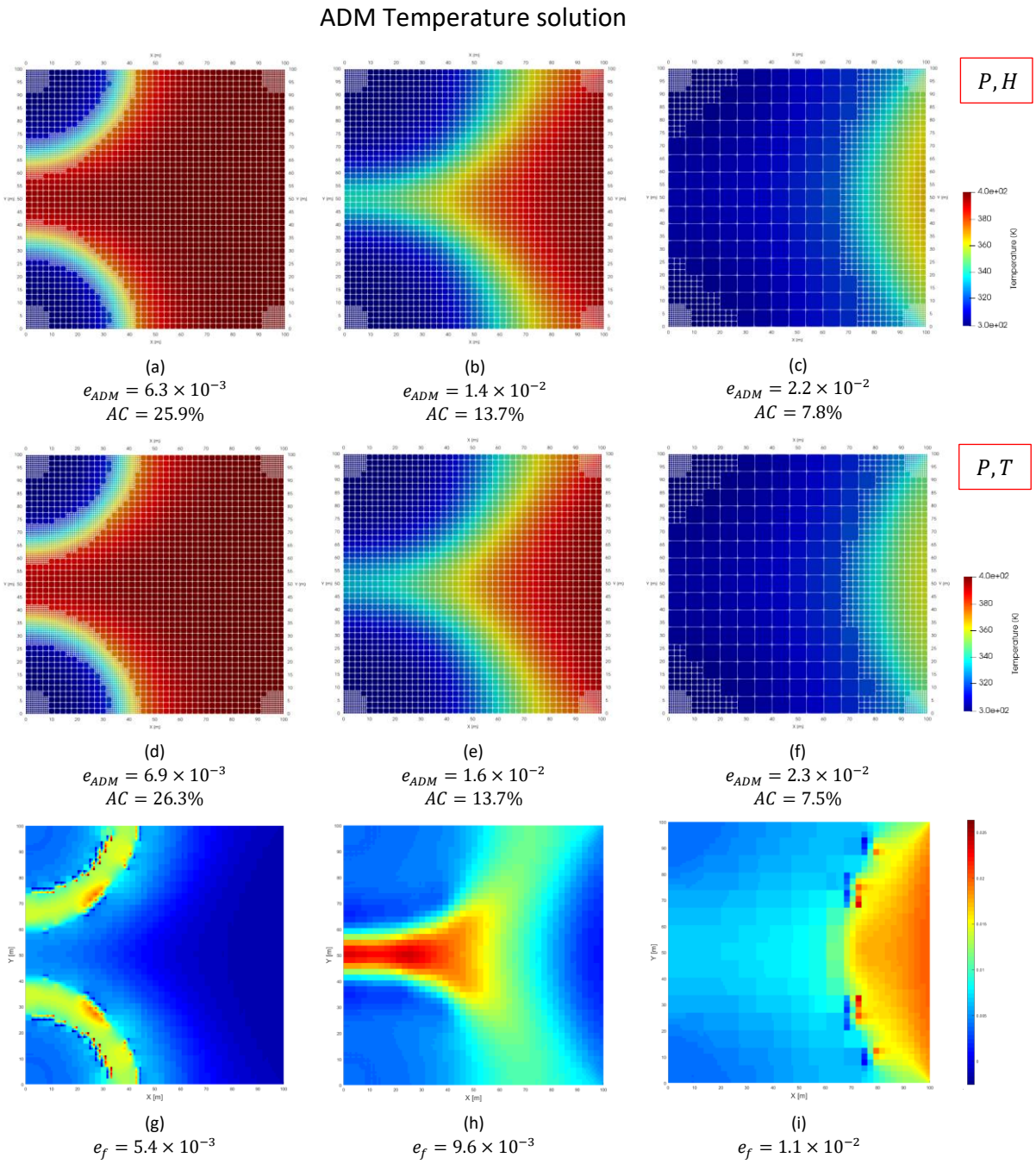

Figure 4.8: ADM simulation results of reservoir temperature for realization 1 of the Soultz-sous-Forêts geothermal field. The first and second rows show the results using the molar and natural formulation, respectively. The third row shows the error between the results of both formulations. Column wise, the simulation time increases from 400 to 1000 to 2000 [days]. The formulation error e_f indicates the relative difference between the solutions obtained from both formulations.

The algebraic dynamic multilevel (ADM) simulation results of the reservoir enthalpy are presented in figure 4.9.

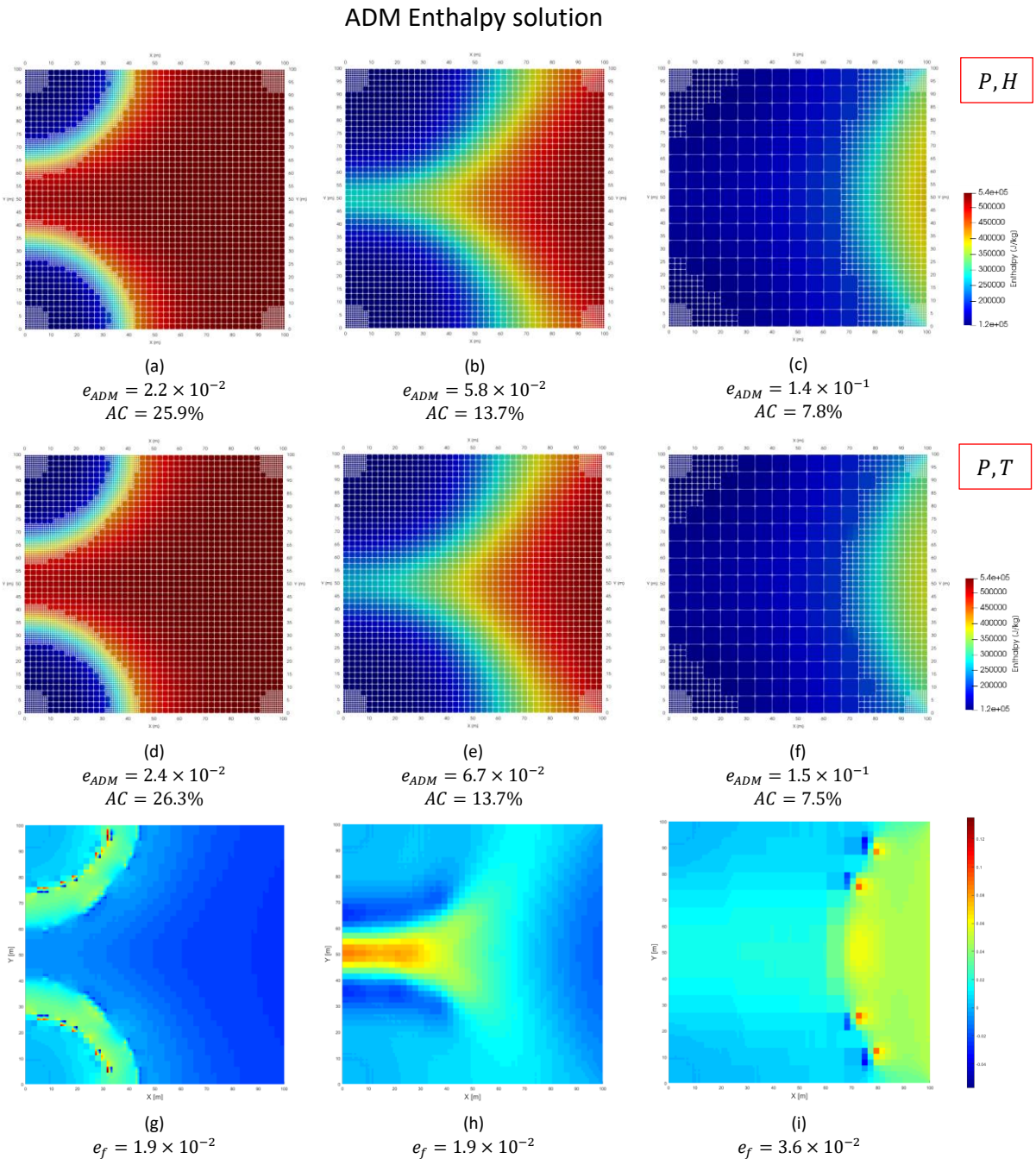

(a)
$e_{ADM} = 2.2 \times 10^{-2}$
$AC = 25.9\%$

(b)
$e_{ADM} = 5.8 \times 10^{-2}$
$AC = 13.7\%$

(c)
$e_{ADM} = 1.4 \times 10^{-1}$
$AC = 7.8\%$

(d)
$e_{ADM} = 2.4 \times 10^{-2}$
$AC = 26.3\%$

(e)
$e_{ADM} = 6.7 \times 10^{-2}$
$AC = 13.7\%$

(f)
$e_{ADM} = 1.5 \times 10^{-1}$
$AC = 7.5\%$

(g)
$e_f = 1.9 \times 10^{-2}$

(h)
$e_f = 1.9 \times 10^{-2}$

(i)
$e_f = 3.6 \times 10^{-2}$

Figure 4.9: ADM simulation results of reservoir enthalpy for realization 1 of the Soultz-sous-Forêts geothermal field. The first and second rows show the results using the molar and natural formulation, respectively. The third row shows the error between the results of both formulations. Column wise, the simulation time increases from 400 to 1000 to 2000 [days]. The formulation error e_f indicates the relative difference between the solutions obtained from both formulations.

The error between both formulations in terms of reservoir pressure, temperature and enthalpy is presented in figure 4.10. The error is presented for both fine-scale and ADM simulation over the total number of timesteps.

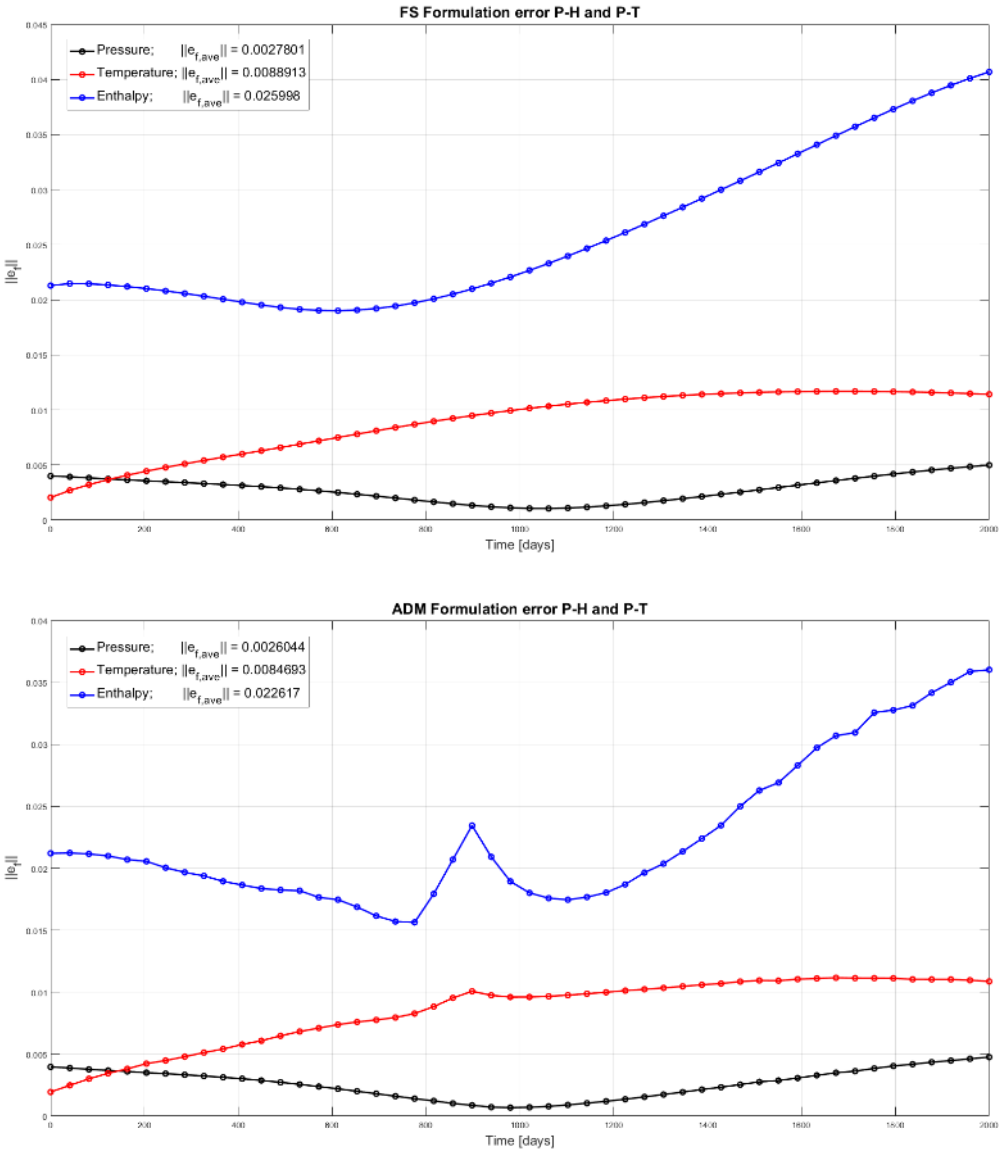

Figure 4.10: Pressure, temperature and enthalpy error between the molar and natural formulation e_f, for fine-scale (top) and ADM (bottom) simulations. The formulation error e_f indicates the relative difference between the solutions obtained from both formulations.

The performance comparison between both formulations is presented in figure 4.11, for both fine-scale and ADM simulations.

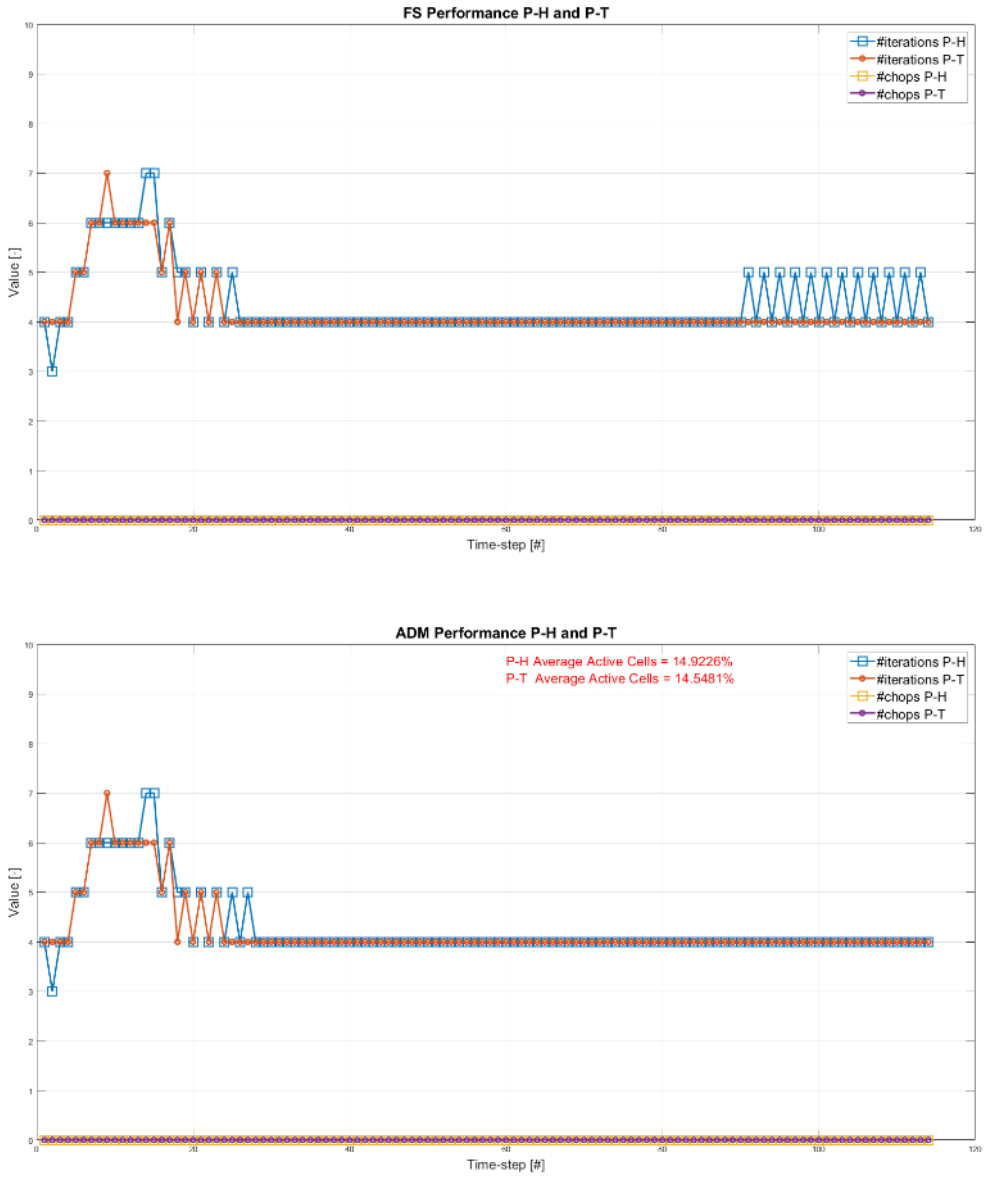

Figure 4.11: Fine-scale (top) and ADM (bottom) simulation performance for both formulations. The performance is compared at each timestep. Note that the average number of active cells during the entire simulation is marked in red in the ADM performance chart.

4.2. Soultz-sous-Forêts – Realization 2

The second realization of the Soultz-sous-Forêts geothermal field is one with a fracture network that consists of 15 fractures. The fine-scale simulation results of the reservoir pressure are presented in figure 4.12. The pressure solution using the molar formulation is presented in subfigures (a), (b) and (c), and the pressure solution using the natural formulation is presented in subfigures (d), (e) and (f) for simulation times of 400, 1000 and 2000 [days], respectively. Subfigures (g), (h) and (i) show the error e_f between the solutions of both formulations at the respective simulation times.

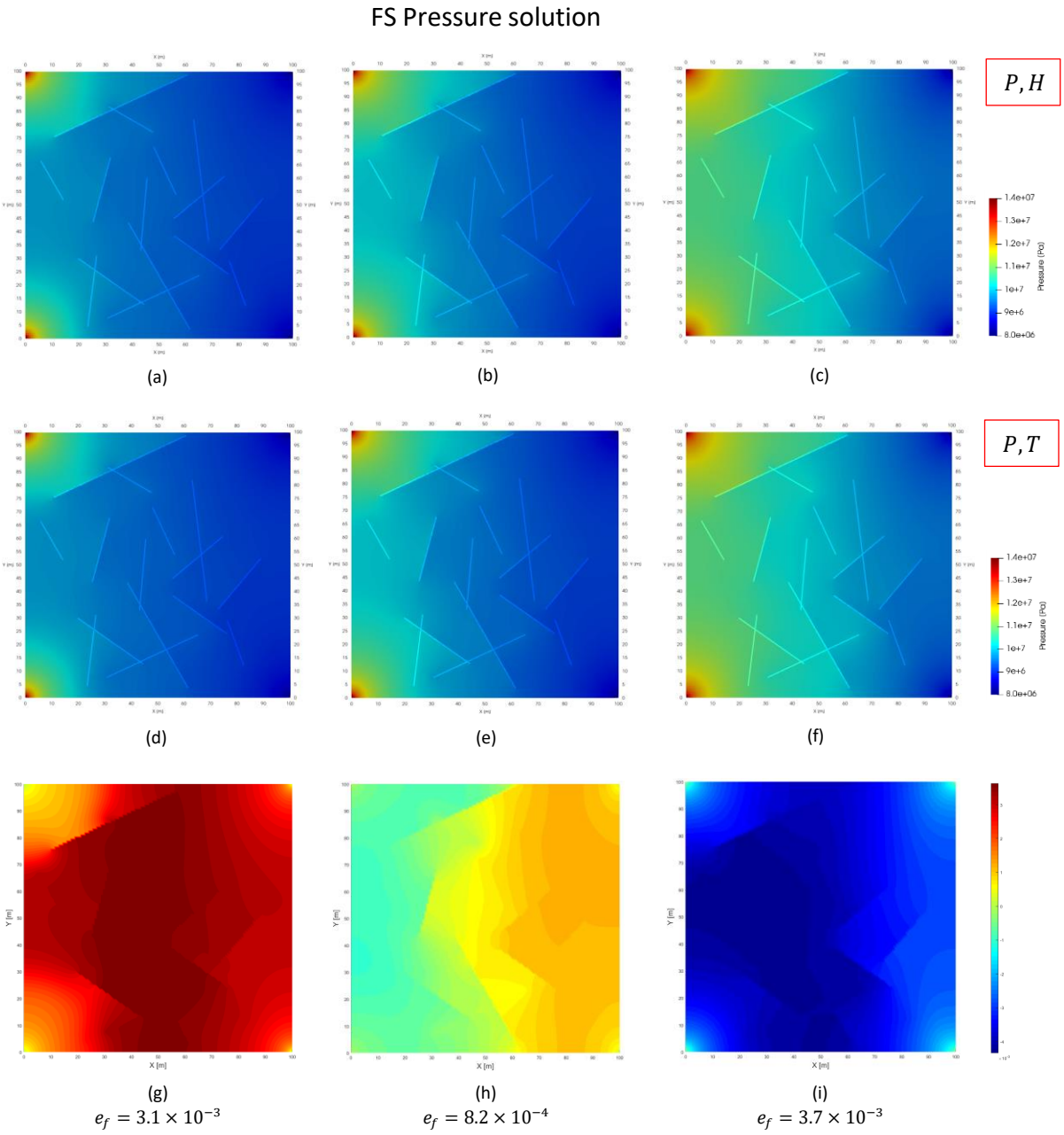

Figure 4.12: Fine-scale simulation results of reservoir pressure for realization 2 of the Soultz-sous-Forêts geothermal field. The first and second rows show the results using the molar and natural formulation, respectively. The third row shows the error between the results of both formulations. Column wise, the simulation time increases from 400 to 1000 to 2000 [days]. The formulation error e_f indicates the relative difference between the solutions obtained from both formulations.

The fine-scale simulation results of the reservoir temperature are presented in figure 4.13.

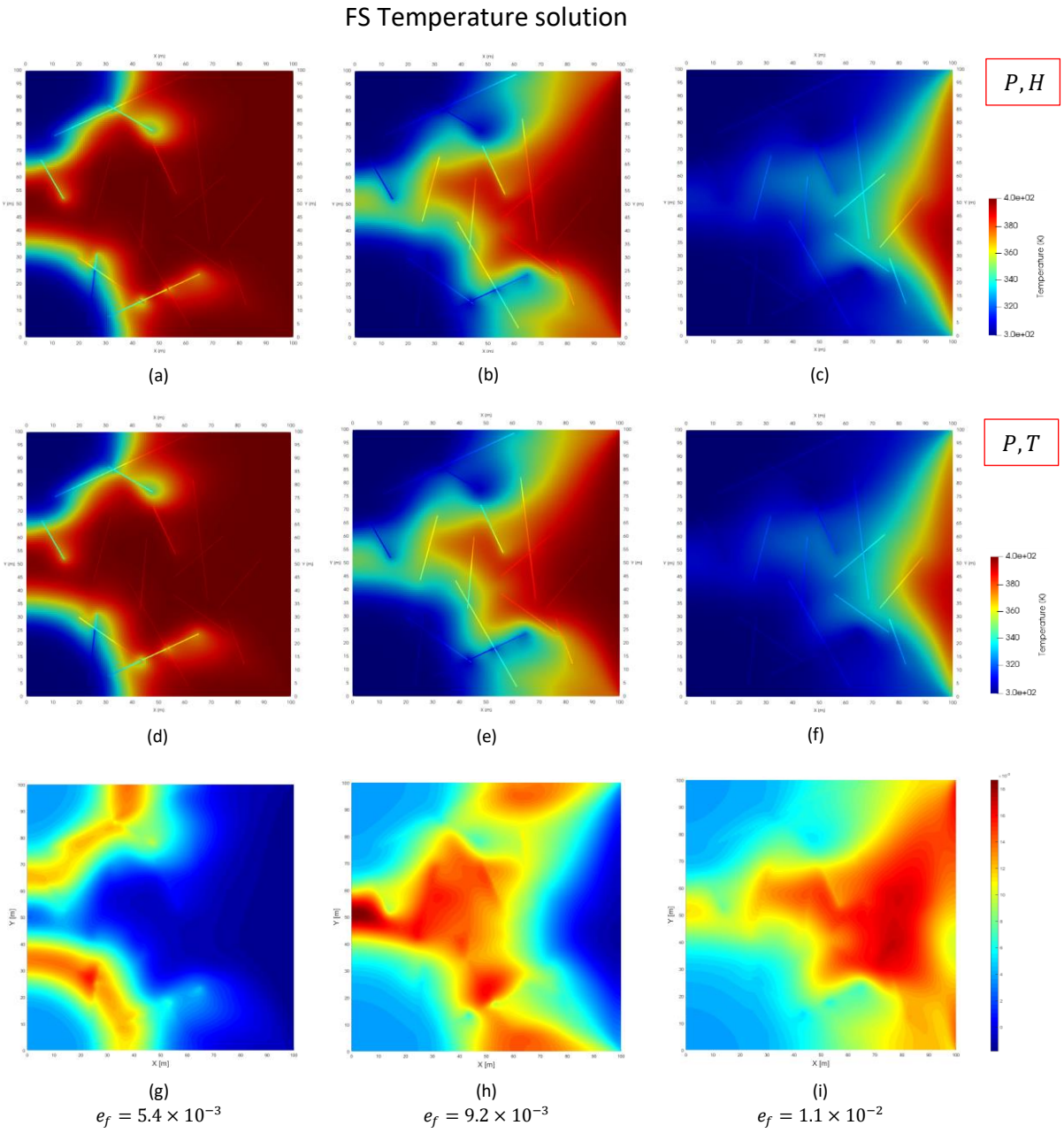

Figure 4.13: Fine-scale simulation results of reservoir temperature for realization 2 of the Soultz-sous-Forêts geothermal field. The first and second rows show the results using the molar and natural formulation, respectively. The third row shows the error between the results of both formulations. Column wise, the simulation time increases from 400 to 1000 to 2000 [days]. The formulation error e_f indicates the relative difference between the solutions obtained from both formulations.

The fine-scale simulation results of the reservoir enthalpy are presented in figure 4.15.

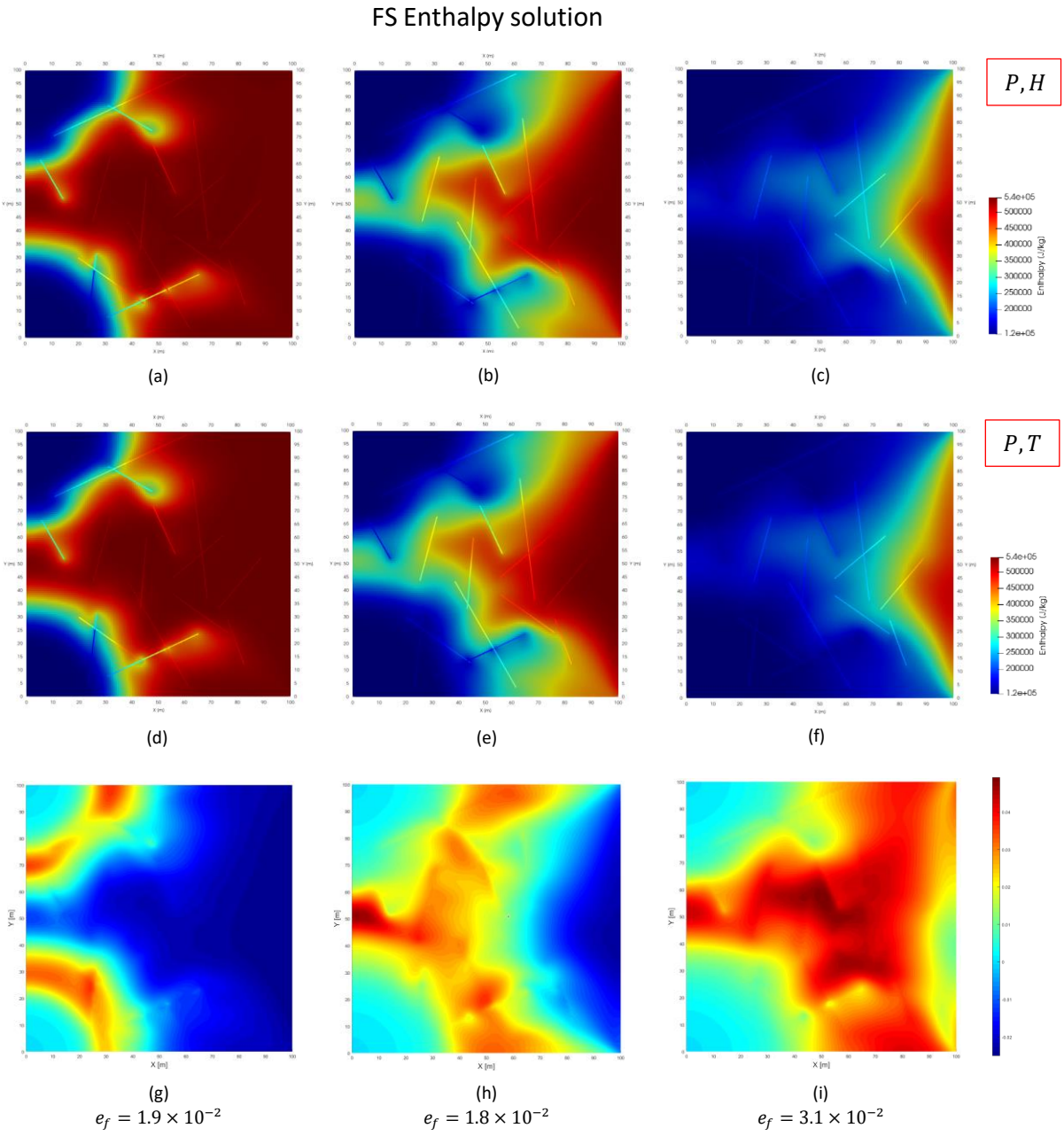

Figure 4.15: Fine-scale simulation results of reservoir enthalpy for realization 2 of the Soultz-sous-Forêts geothermal field. The first and second rows show the results using the molar and natural formulation, respectively. The third row shows the error between the results of both formulations. Column wise, the simulation time increases from 400 to 1000 to 2000 [days]. The formulation error e_f indicates the relative difference between the solutions obtained from both formulations.

The algebraic dynamic multilevel (ADM) simulation results of the reservoir pressure are presented in figure 4.16.

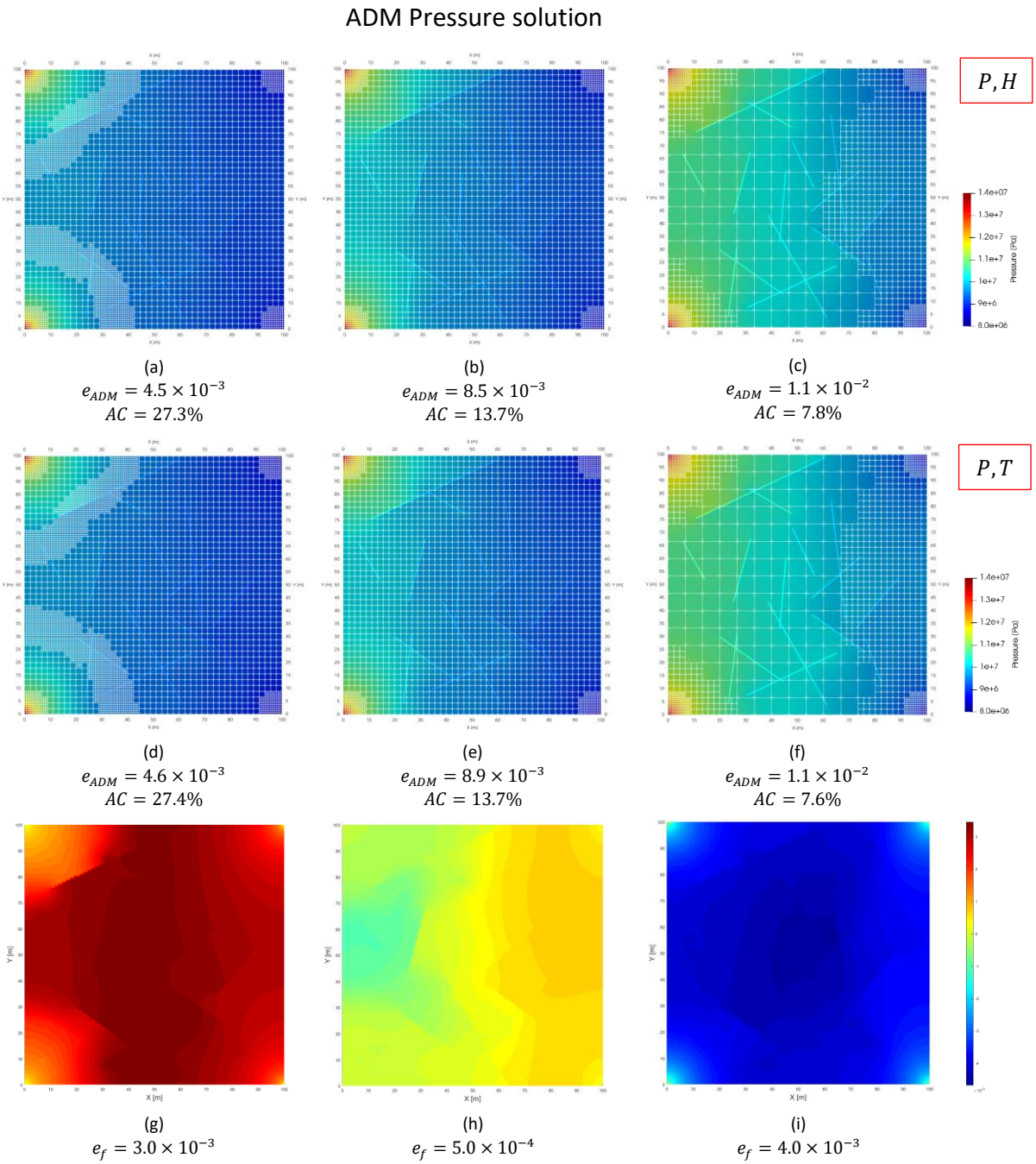

Figure 4.16: ADM simulation results of reservoir pressure for realization 2 of the Soultz-sous-Forêts geothermal field. The first and second rows show the results using the molar and natural formulation, respectively. The third row shows the error between the results of both formulations. Column wise, the simulation time increases from 400 to 1000 to 2000 [days]. The formulation error e_f indicates the relative difference between the solutions obtained from both formulations.

The algebraic dynamic multilevel (ADM) simulation results of the reservoir temperature are presented in figure 4.17.

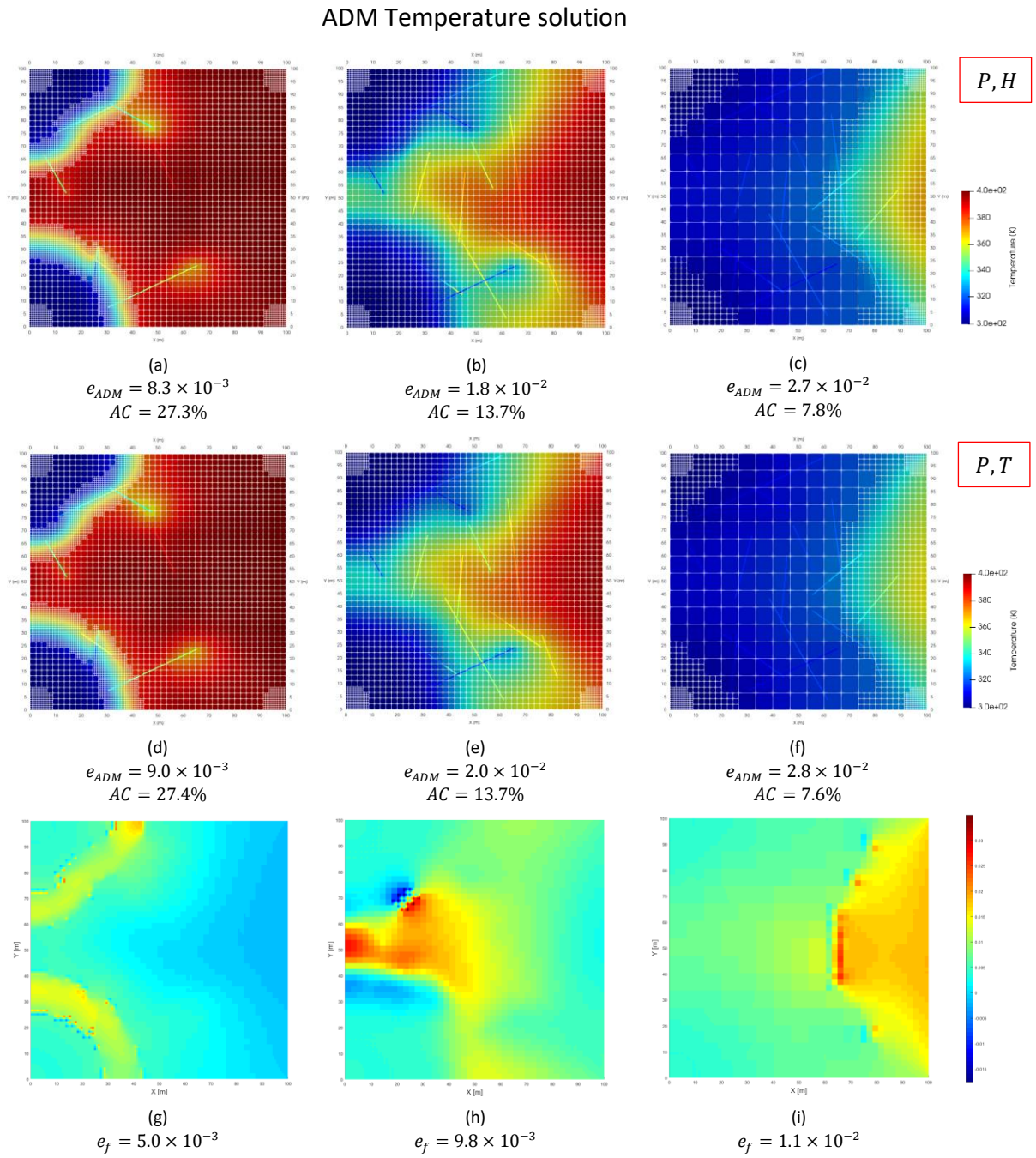

Figure 4.17: ADM simulation results of reservoir temperature for realization 2 of the Soultz-sous-Forêts geothermal field. The first and second rows show the results using the molar and natural formulation, respectively. The third row shows the error between the results of both formulations. Column wise, the simulation time increases from 400 to 1000 to 2000 [days]. The formulation error e_f indicates the relative difference between the solutions obtained from both formulations.

The algebraic dynamic multilevel (ADM) simulation results of the reservoir enthalpy are presented in figure 4.18.

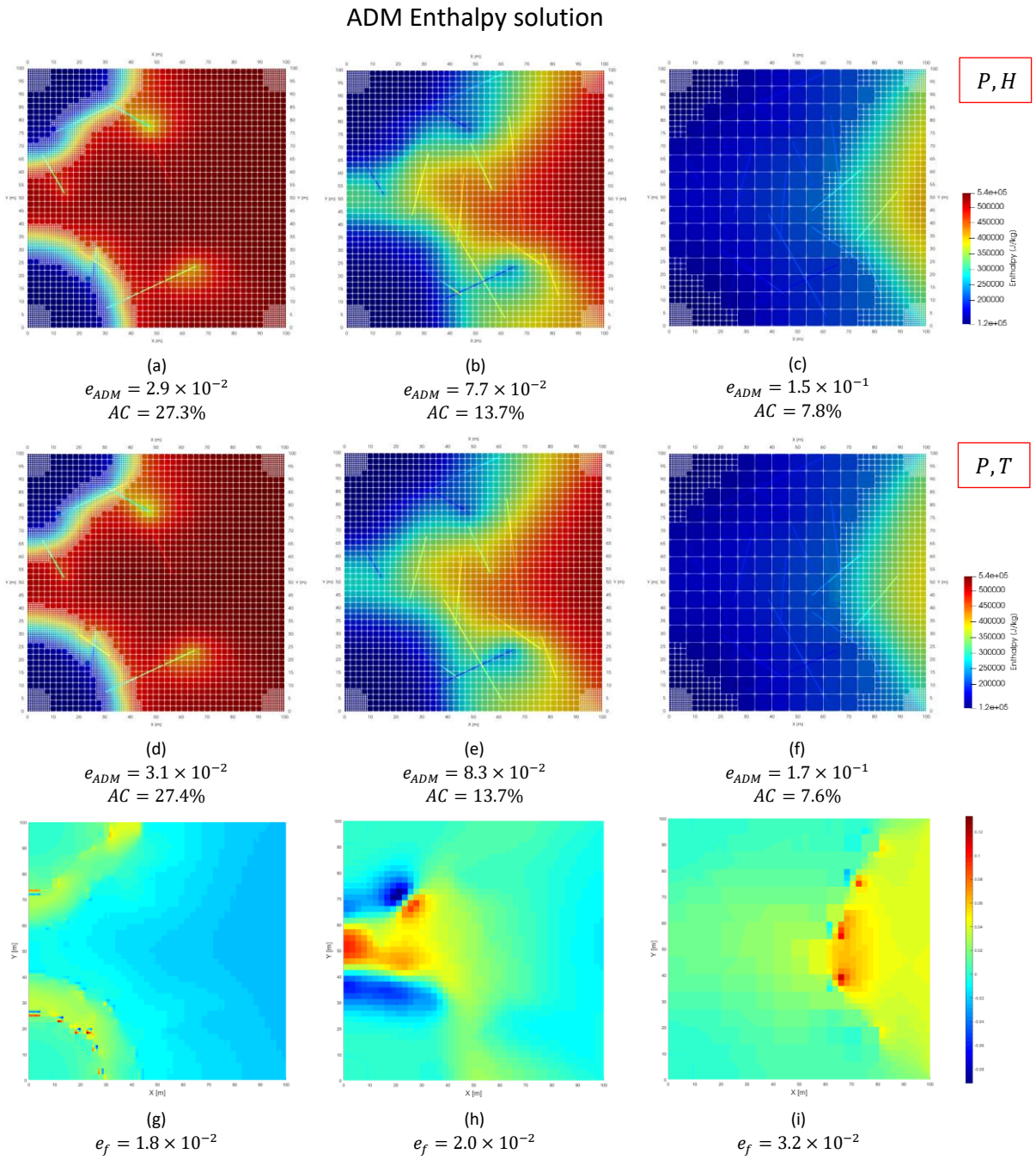

(a)
$e_{ADM} = 2.9 \times 10^{-2}$
$AC = 27.3\%$

(b)
$e_{ADM} = 7.7 \times 10^{-2}$
$AC = 13.7\%$

(c)
$e_{ADM} = 1.5 \times 10^{-1}$
$AC = 7.8\%$

(d)
$e_{ADM} = 3.1 \times 10^{-2}$
$AC = 27.4\%$

(e)
$e_{ADM} = 8.3 \times 10^{-2}$
$AC = 13.7\%$

(f)
$e_{ADM} = 1.7 \times 10^{-1}$
$AC = 7.6\%$

(g)
$e_f = 1.8 \times 10^{-2}$

(h)
$e_f = 2.0 \times 10^{-2}$

(i)
$e_f = 3.2 \times 10^{-2}$

Figure 4.18: ADM simulation results of reservoir enthalpy for realization 2 of the Soultz-sous-Forêts geothermal field. The first and second rows show the results using the molar and natural formulation, respectively. The third row shows the error between the results of both formulations. Column wise, the simulation time increases from 400 to 1000 to 2000 [days]. The formulation error e_f indicates the relative difference between the solutions obtained from both formulations.

The error between both formulations in terms of reservoir pressure, temperature and enthalpy is presented in figure 4.19. The error is presented for both fine-scale and ADM simulation over the total number of timesteps.

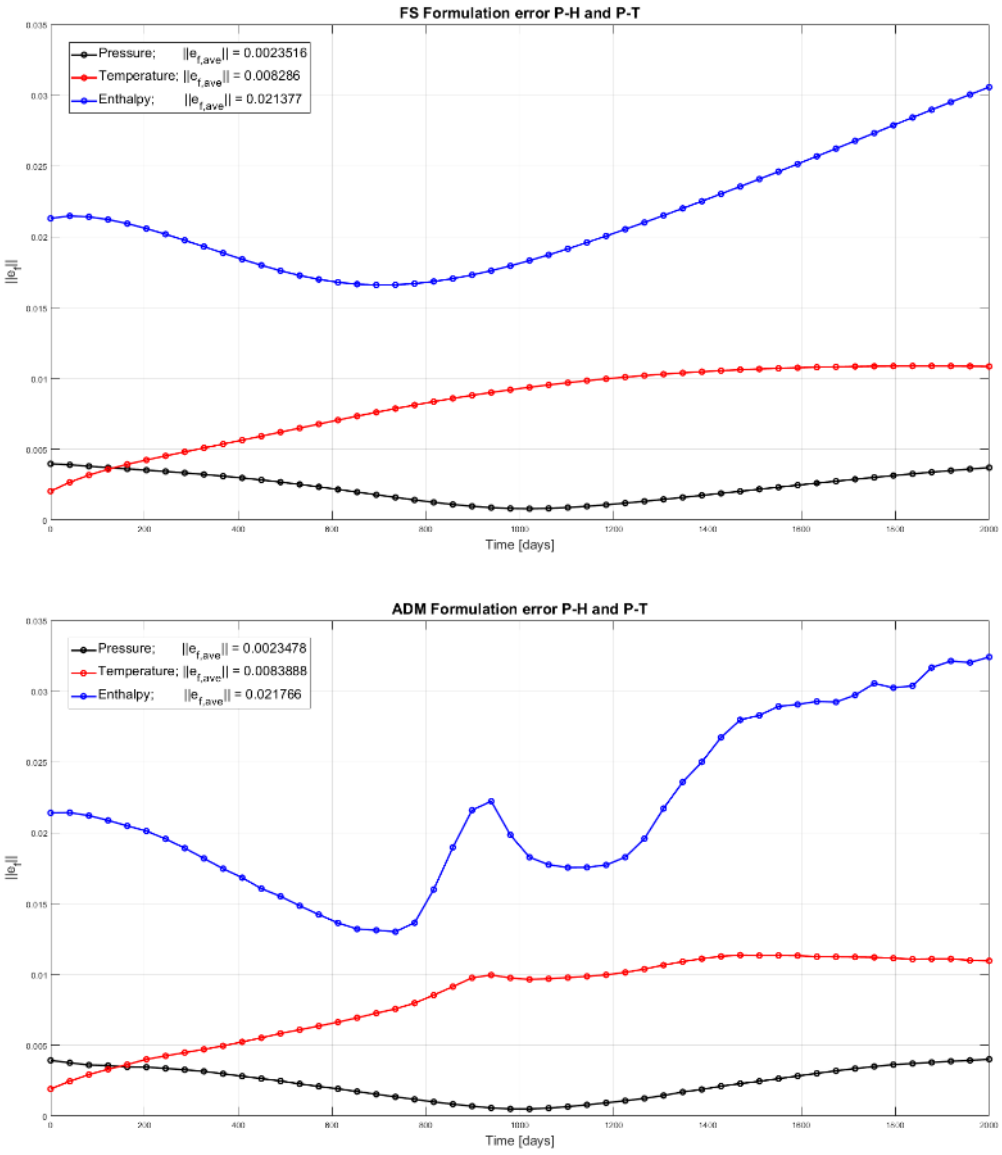

Figure 4.19: Pressure, temperature and enthalpy error between the molar and natural formulation e_f, for fine-scale (top) and ADM (bottom) simulations. The formulation error e_f indicates the relative difference between the solutions obtained from both formulations.

The performance comparison between both formulations is presented in figure 4.20, for both fine-scale and ADM simulations.

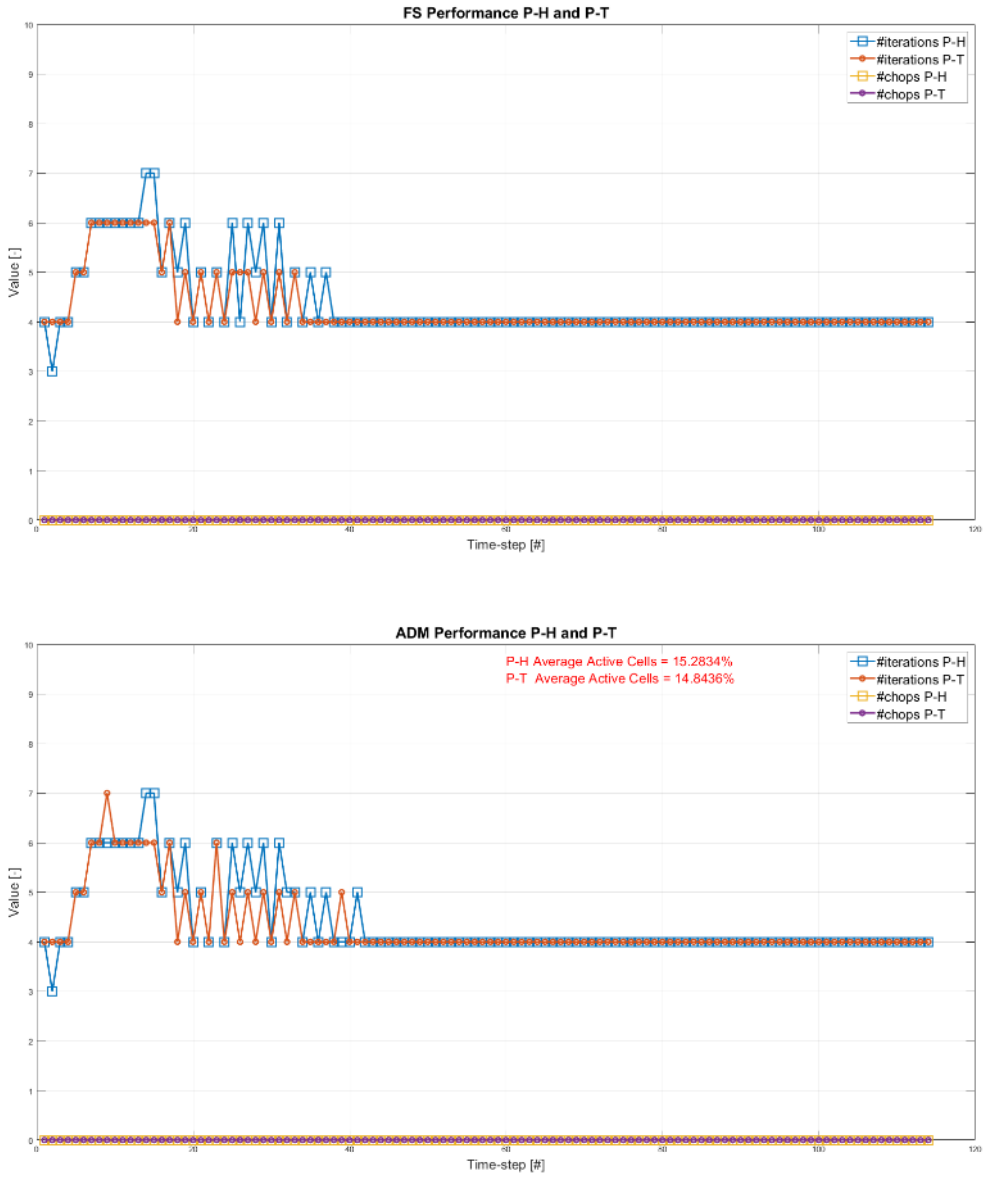

Figure 4.20: Fine-scale (top) and ADM (bottom) simulation performance for both formulations. The performance is compared at each timestep. Note that the average number of active cells during the entire simulation is marked in red in the ADM performance chart.

4.3. Soultz-sous-Forêts – Realization 3

The third realization of the Soultz-sous-Forêts geothermal field is one with a fracture network that consists of 30 fractures. The fine-scale simulation results of the reservoir pressure are presented in figure 4.21. The pressure solution using the molar formulation is presented in subfigures (a), (b) and (c), and the pressure solution using the natural formulation is presented in subfigures (d), (e) and (f) for simulation times of 400, 1000 and 2000 [days], respectively. Subfigures (g), (h) and (i) show the error e_f between the solutions of both formulations at the respective simulation times.

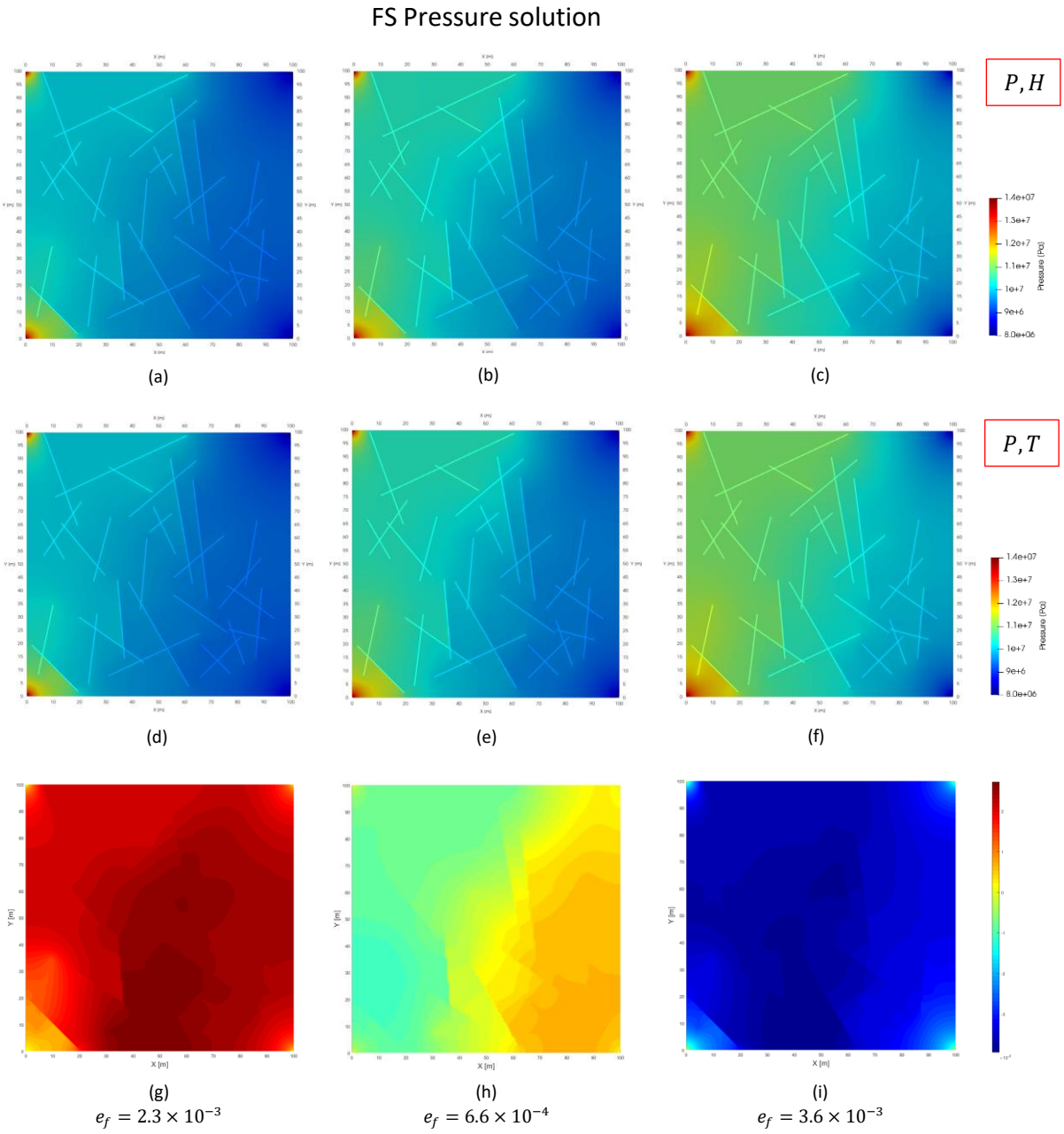

Figure 4.21: Fine-scale simulation results of reservoir pressure for realization 3 of the Soultz-sous-Forêts geothermal field. The first and second rows show the results using the molar and natural formulation, respectively. The third row shows the error between the results of both formulations. Column wise, the simulation time increases from 400 to 1000 to 2000 [days]. The formulation error e_f indicates the relative difference between the solutions obtained from both formulations.

The fine-scale simulation results of the reservoir temperature are presented in figure 4.22.

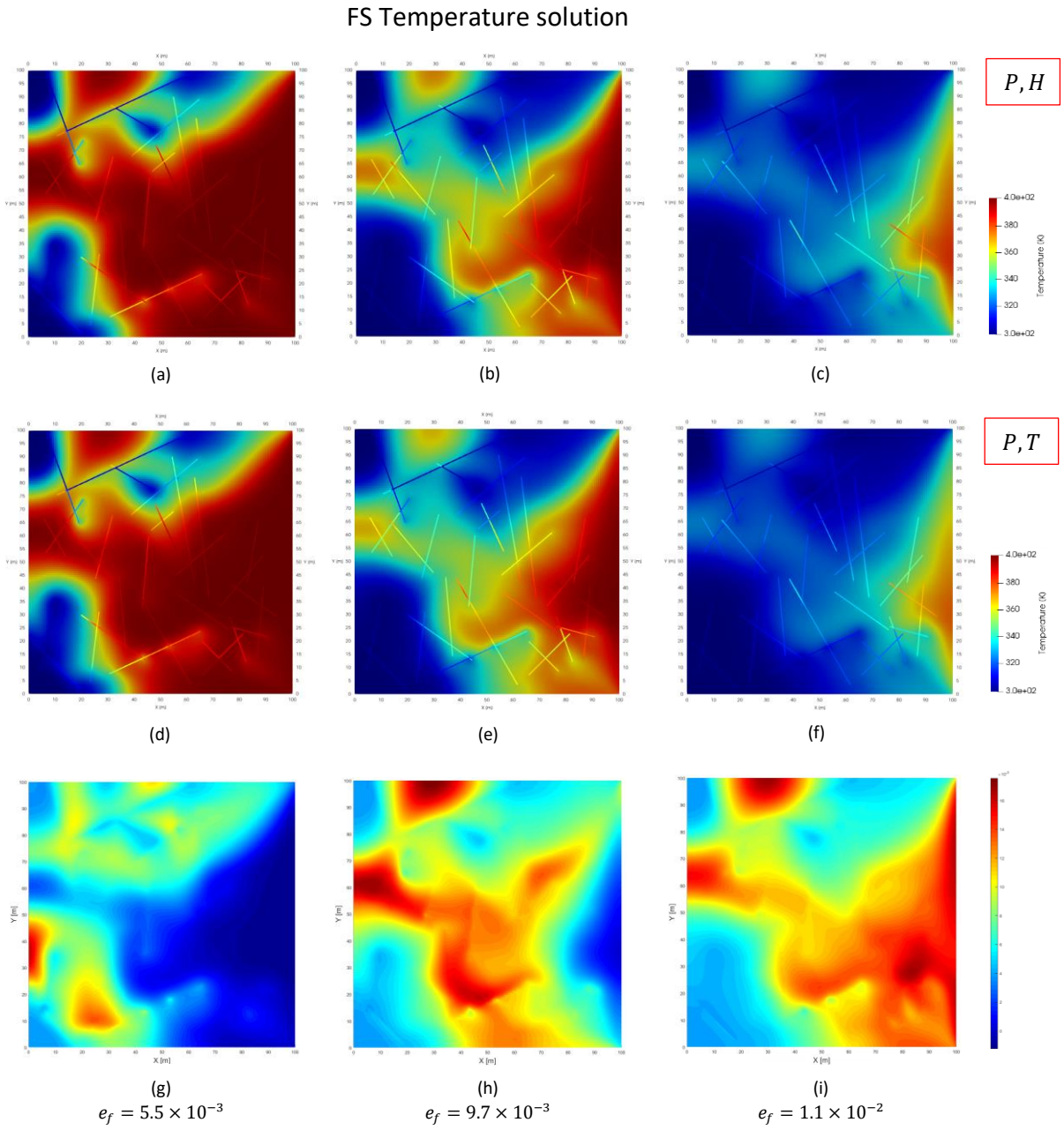

Figure 4.22: Fine-scale simulation results of reservoir temperature for realization 3 of the Soultz-sous-Forêts geothermal field. The first and second rows show the results using the molar and natural formulation, respectively. The third row shows the error between the results of both formulations. Column wise, the simulation time increases from 400 to 1000 to 2000 [days]. The formulation error e_f indicates the relative difference between the solutions obtained from both formulations.

The fine-scale simulation results of the reservoir enthalpy are presented in figure 4.23.

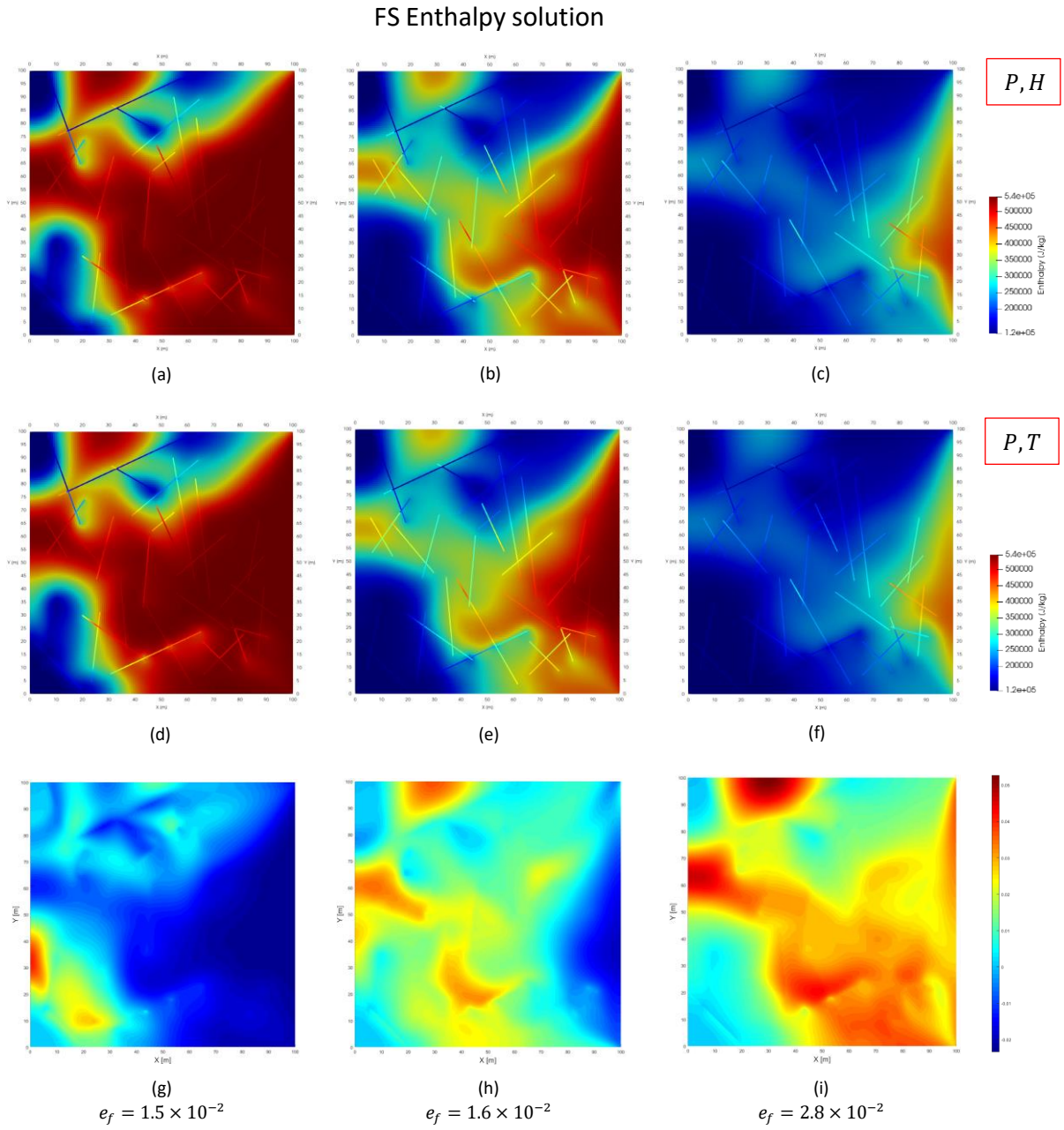

Figure 4.23: Fine-scale simulation results of reservoir enthalpy for realization 3 of the Soultz-sous-Forêts geothermal field. The first and second rows show the results using the molar and natural formulation, respectively. The third row shows the error between the results of both formulations. Column wise, the simulation time increases from 400 *to* 1000 *to* 2000 *[days]. The formulation error* e_f *indicates the relative difference between the solutions obtained from both formulations.*

The algebraic dynamic multilevel (ADM) simulation results of the reservoir pressure, temperature and enthalpy using the molar formulation are presented in figure 4.24.

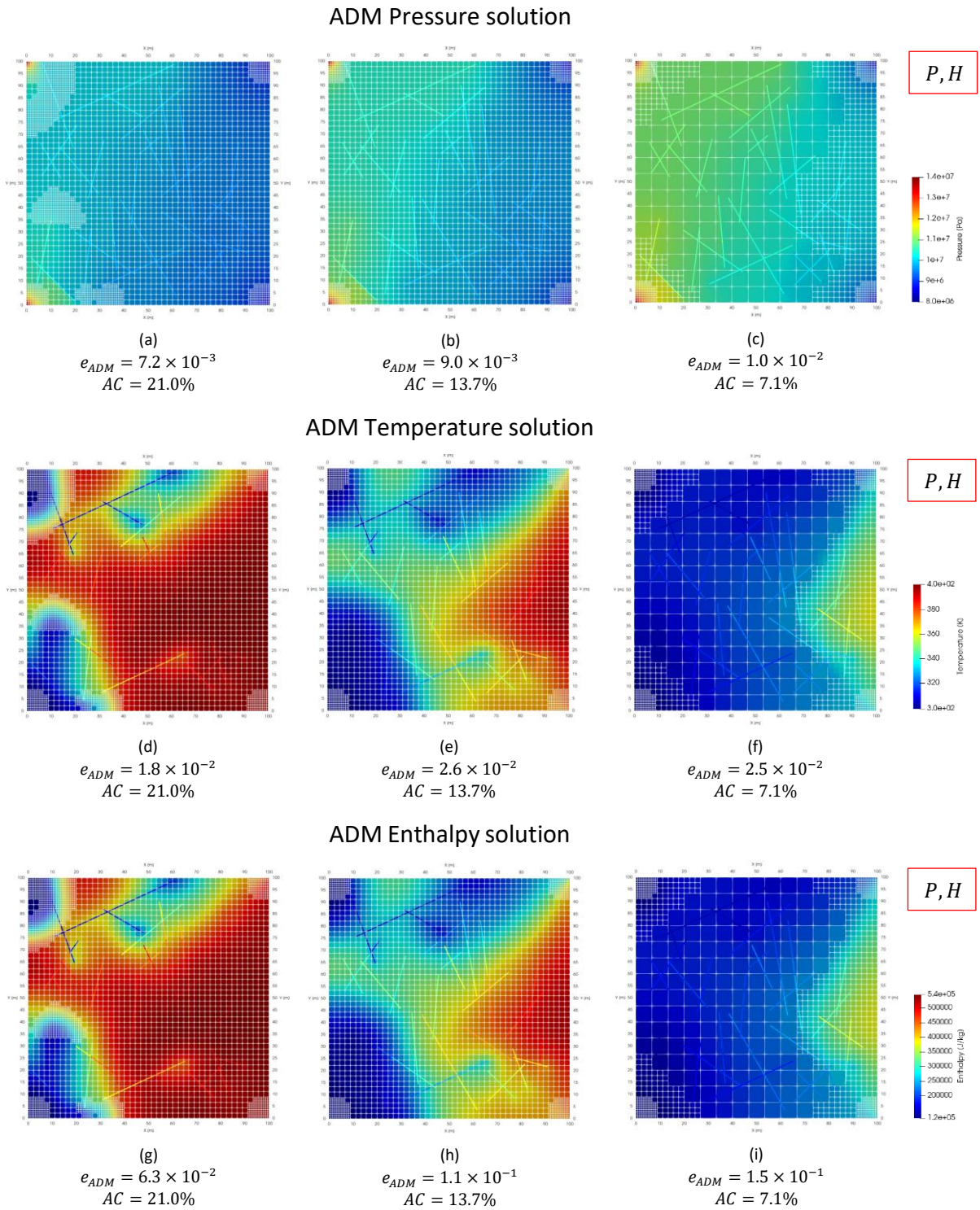

(a)
$e_{ADM} = 7.2 \times 10^{-3}$
$AC = 21.0\%$

(b)
$e_{ADM} = 9.0 \times 10^{-3}$
$AC = 13.7\%$

(c)
$e_{ADM} = 1.0 \times 10^{-2}$
$AC = 7.1\%$

(d)
$e_{ADM} = 1.8 \times 10^{-2}$
$AC = 21.0\%$

(e)
$e_{ADM} = 2.6 \times 10^{-2}$
$AC = 13.7\%$

(f)
$e_{ADM} = 2.5 \times 10^{-2}$
$AC = 7.1\%$

(g)
$e_{ADM} = 6.3 \times 10^{-2}$
$AC = 21.0\%$

(h)
$e_{ADM} = 1.1 \times 10^{-1}$
$AC = 13.7\%$

(i)
$e_{ADM} = 1.5 \times 10^{-1}$
$AC = 7.1\%$

Figure 4.24: ADM simulation results of reservoir pressure (top), temperature (middle) and enthalpy (bottom) using the molar formulation for realization 3 of the Soultz-sous-Forêts geothermal field. Column wise, the simulation time increases from 400 to 1000 to 2000 [days]. The formulation error e_f indicates the relative difference between the solutions obtained from both formulations.

The error between both formulations in terms of reservoir pressure, temperature and enthalpy is presented in figure 4.25. The error is presented for the fine-scale simulation over the total number of timesteps.

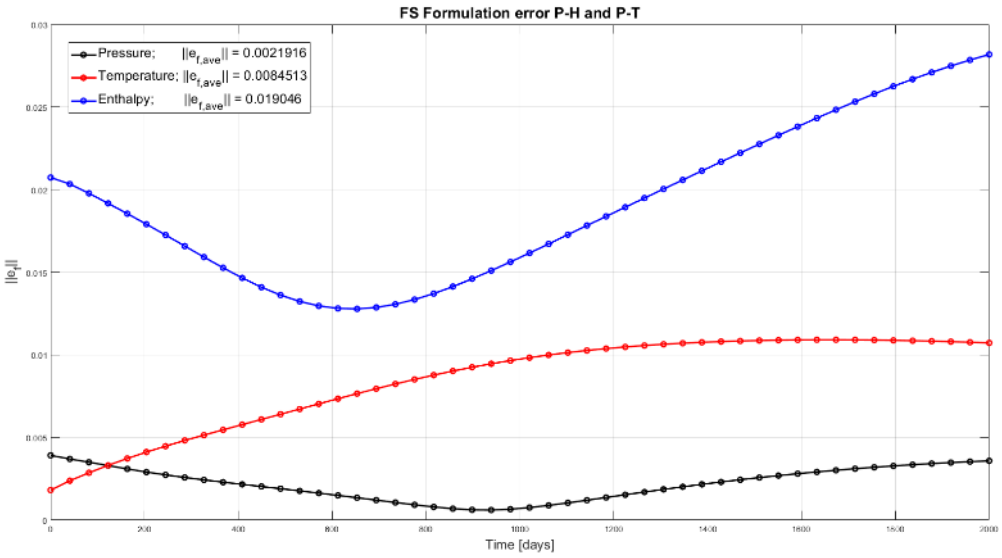

Figure 4.25: Pressure, temperature and enthalpy error between the molar and natural formulation e_f, for fine-scale simulations. The formulation error e_f indicates the relative difference between the solutions obtained from both formulations.

The performance comparison between both formulations is presented in figure 4.26, for the fine-scale simulations.

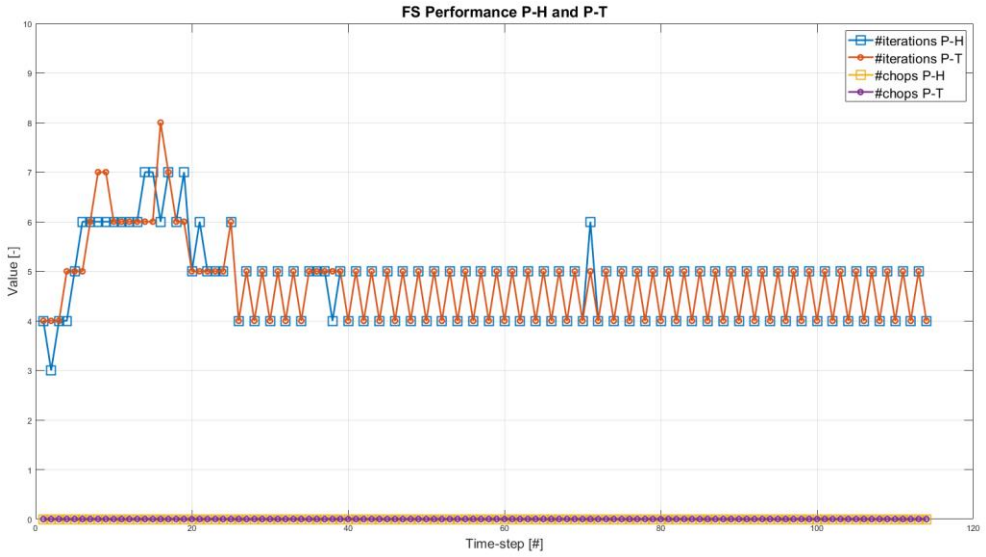

Figure 4.26: Fine-scale simulation performance for both formulations. The performance is compared at each timestep.

The performance of the molar formulation is presented in figure 4.27, for the ADM simulations.

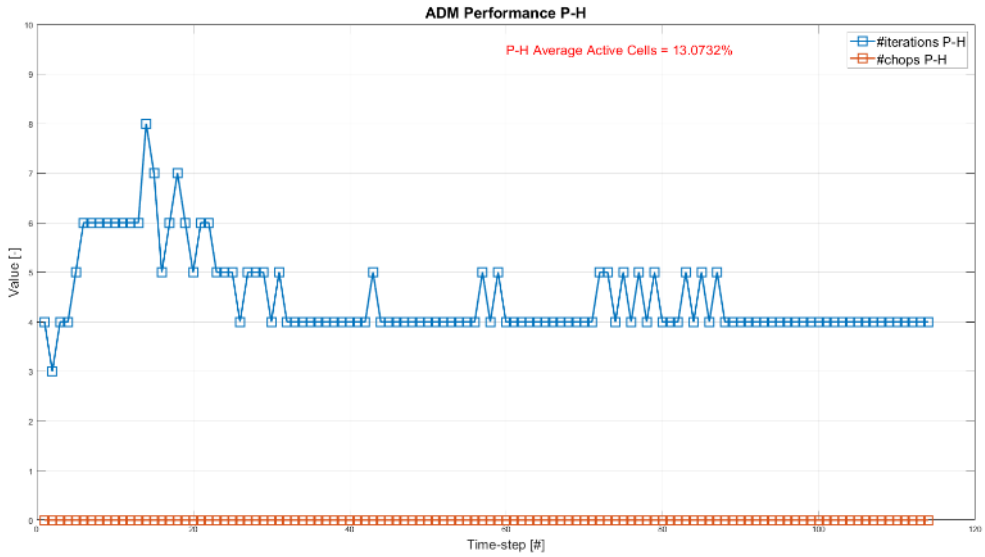

Figure 4.27: ADM simulation performance for the molar formulation.

Note that the ADM simulation results and performance are presented for the molar formulation only as the ADM simulation using the natural formulation was unable to find a solution.

4.4. Middenmeer – Realization 1

The first realization of the Middenmeer geothermal field is one without the presence of a fracture network. The fine-scale simulation results of the reservoir pressure are presented in figure 4.28. The pressure solution using the molar formulation is presented in subfigures (a), (b) and (c), and the pressure solution using the natural formulation is presented in subfigures (d), (e) and (f) for simulation times of 400, 1000 and 2000 [days], respectively. Subfigures (g), (h) and (i) show the error e_f between the solutions of both formulations at the respective simulation times.

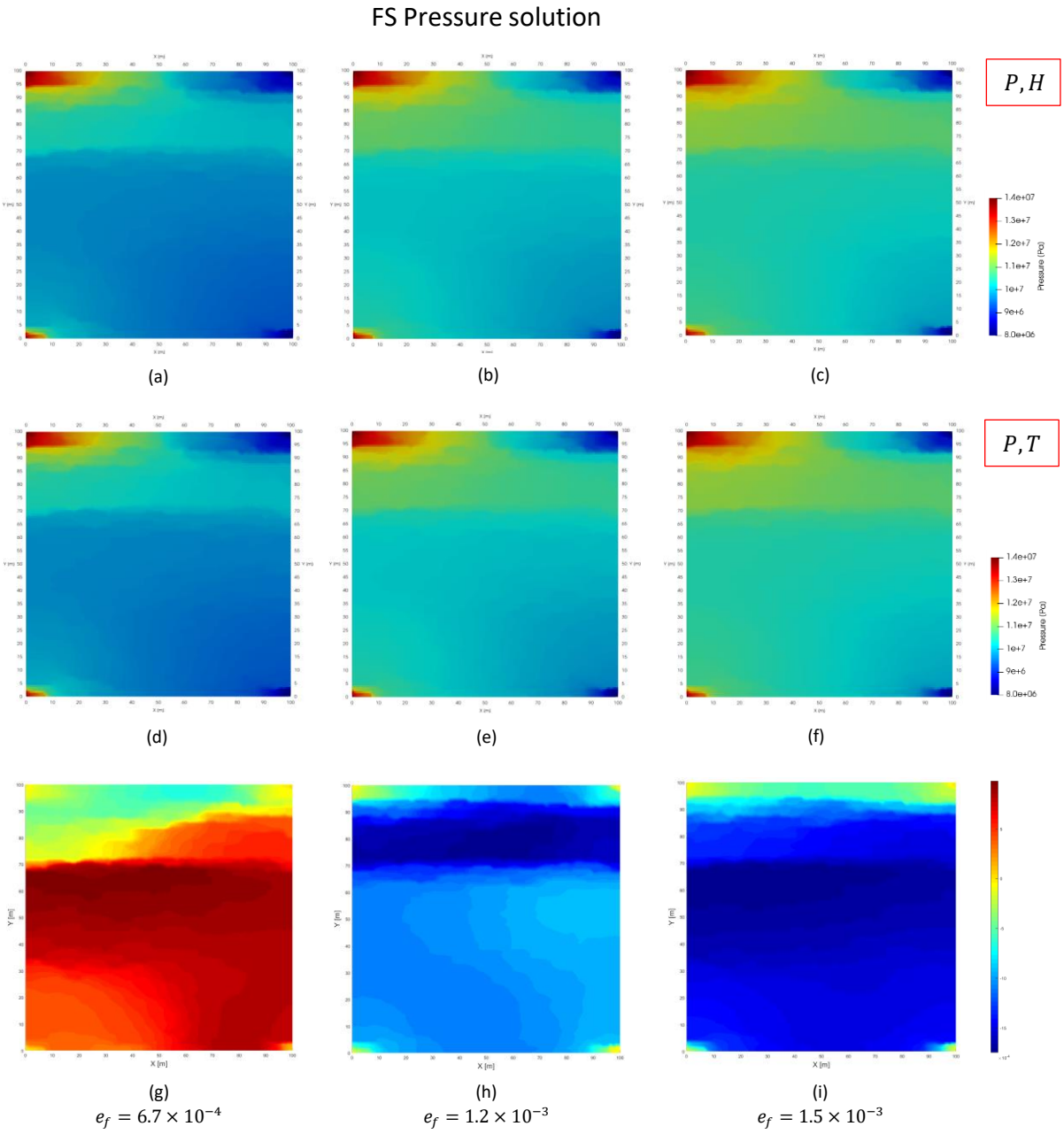

Figure 4.28: Fine-scale simulation results of reservoir pressure for realization 1 of the Middenmeer geothermal field. The first and second rows show the results using the molar and natural formulation, respectively. The third row shows the error between the results of both formulations. Column wise, the simulation time increases from 400 to 1000 to 2000 [days]. The formulation error e_f indicates the relative difference between the solutions obtained from both formulations.

The fine-scale simulation results of the reservoir temperature are presented in figure 4.29.

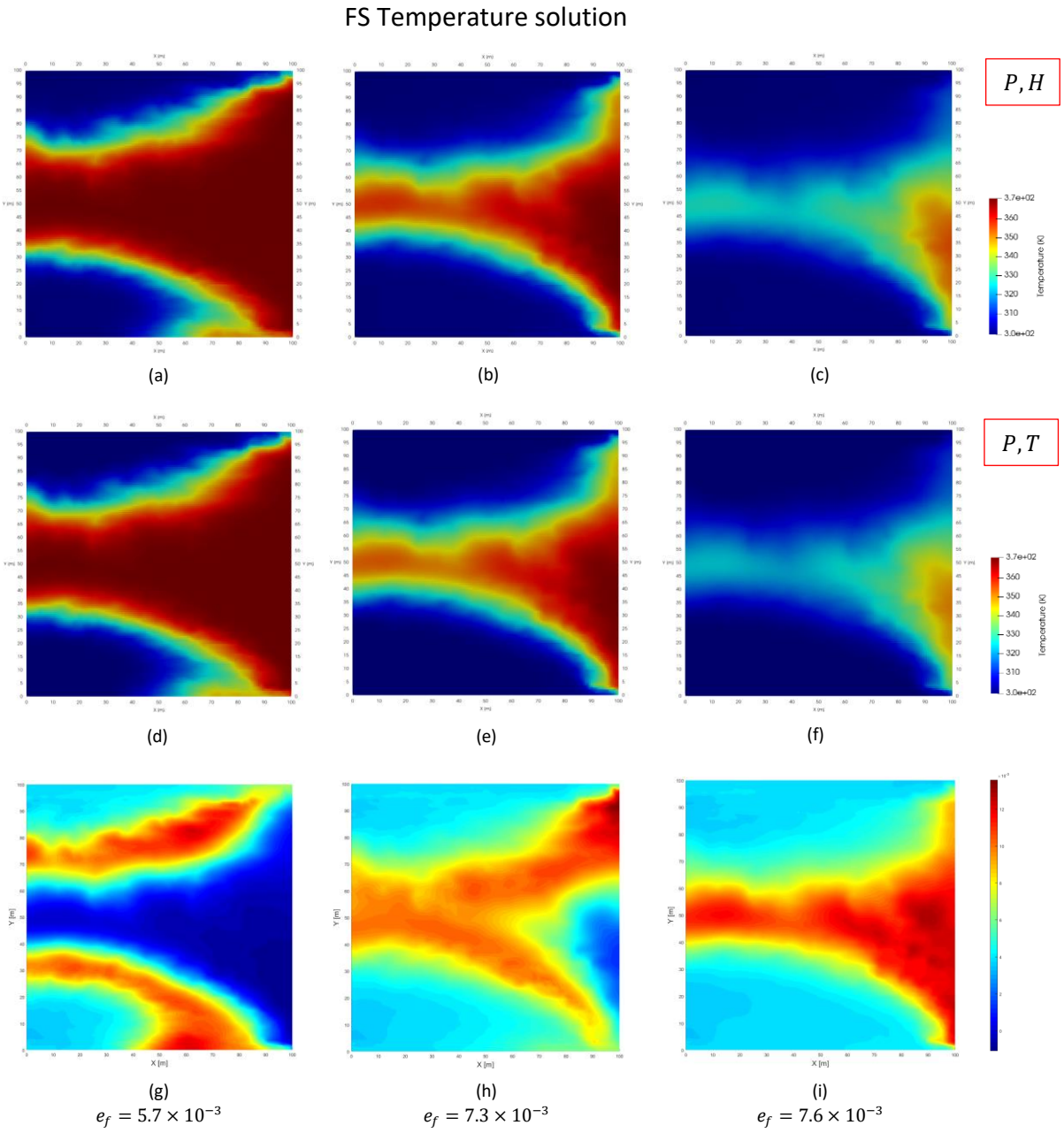

Figure 4.29: Fine-scale simulation results of reservoir temperature for realization 1 of the Middenmeer geothermal field. The first and second rows show the results using the molar and natural formulation, respectively. The third row shows the error between the results of both formulations. Column wise, the simulation time increases from 400 to 1000 to 2000 [days]. The formulation error e_f indicates the relative difference between the solutions obtained from both formulations.

The fine-scale simulation results of the reservoir enthalpy are presented in figure 4.30.

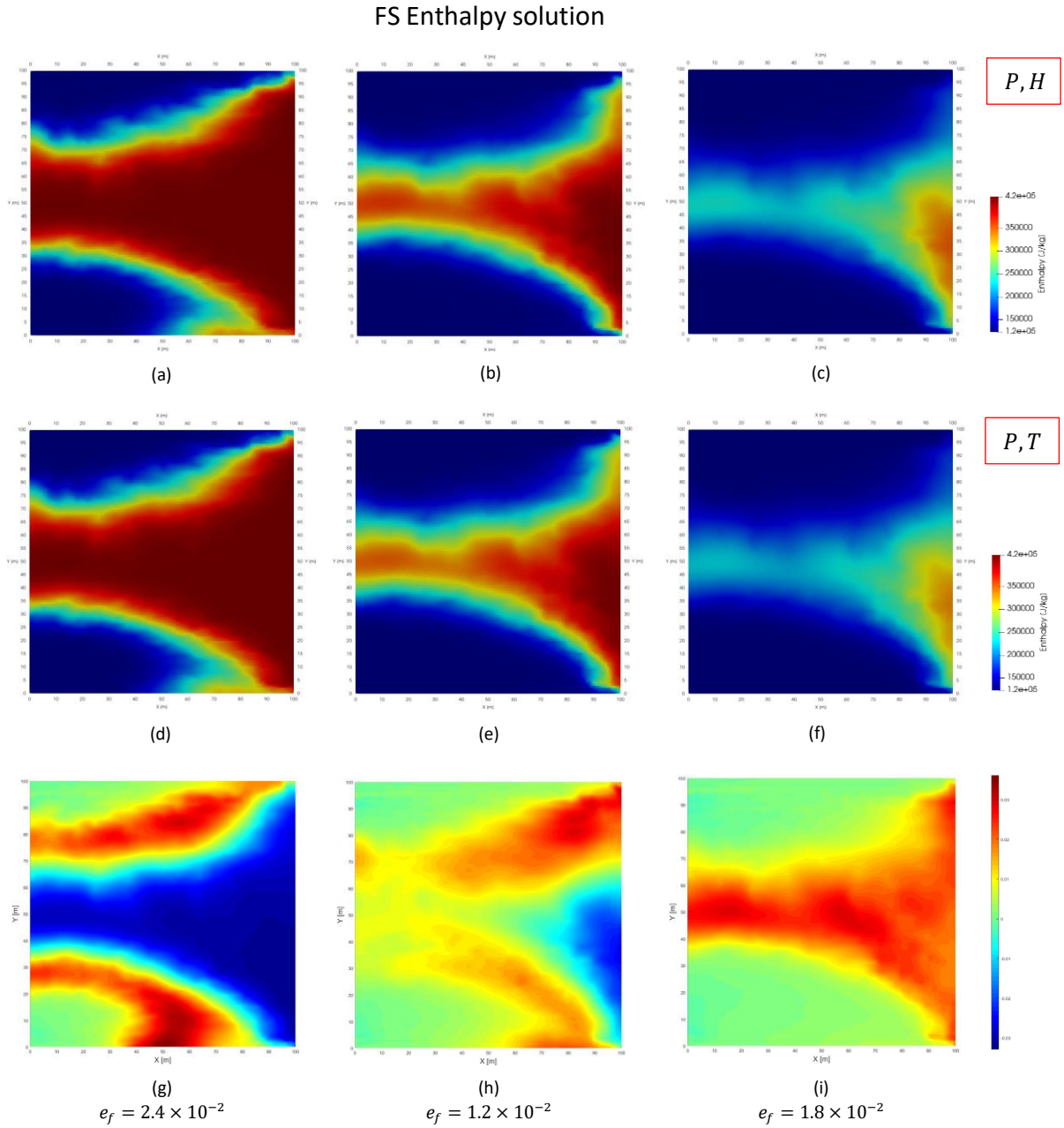

Figure 4.30: Fine-scale simulation results of reservoir enthalpy for realization 1 of the Middenmeer geothermal field. The first and second rows show the results using the molar and natural formulation, respectively. The third row shows the error between the results of both formulations. Column wise, the simulation time increases from 400 to 1000 to 2000 [days]. The formulation error e_f indicates the relative difference between the solutions obtained from both formulations.

The algebraic dynamic multilevel (ADM) simulation results of the reservoir pressure are presented in figure 4.31.

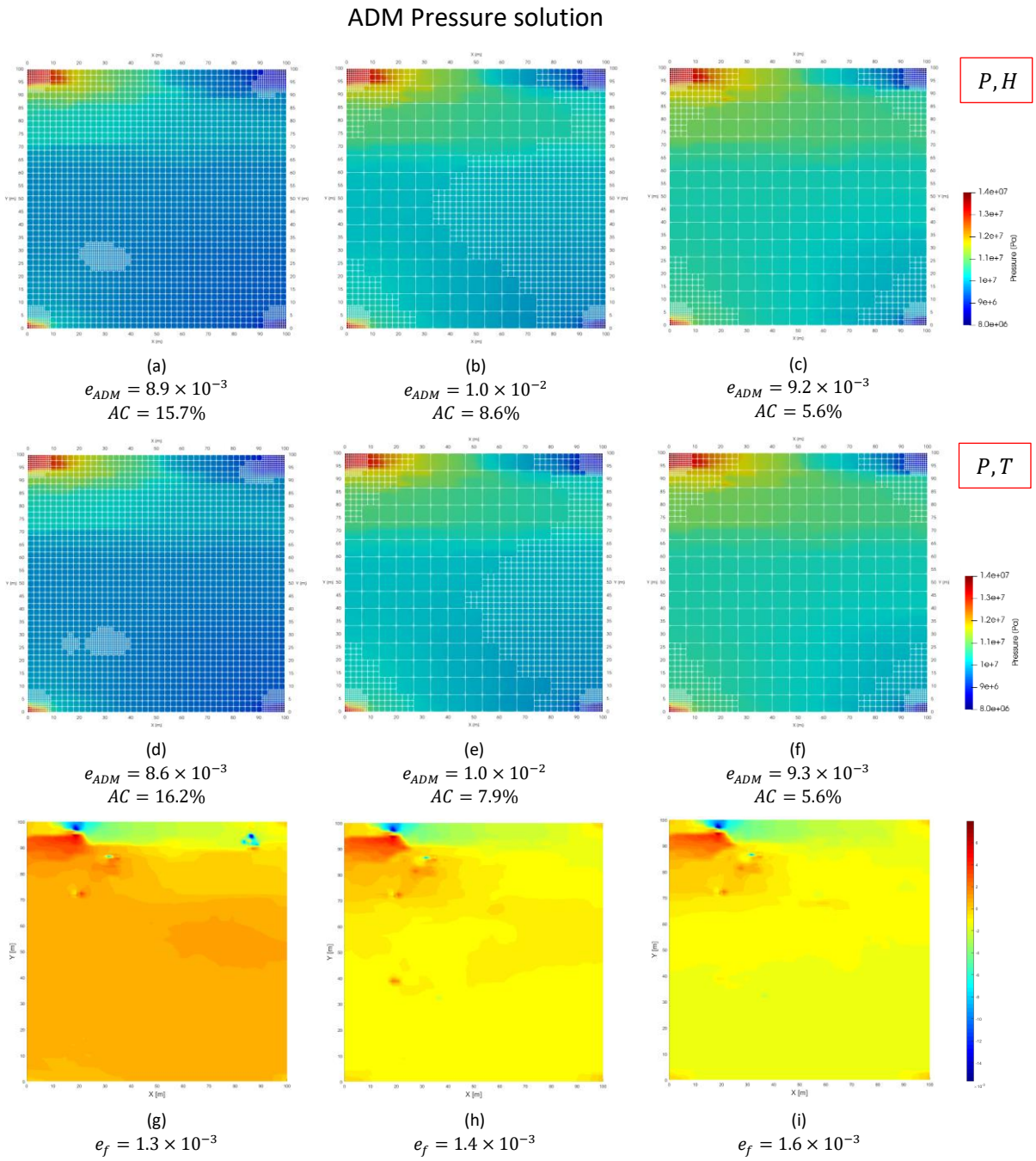

Figure 4.31: ADM simulation results of reservoir pressure for realization 1 of the Middenmeer geothermal field. The first and second rows show the results using the molar and natural formulation, respectively. The third row shows the error between the results of both formulations. Column wise, the simulation time increases from 400 to 1000 to 2000 [days]. The formulation error e_f indicates the relative difference between the solutions obtained from both formulations.

The algebraic dynamic multilevel (ADM) simulation results of the reservoir temperature are presented in figure 4.32.

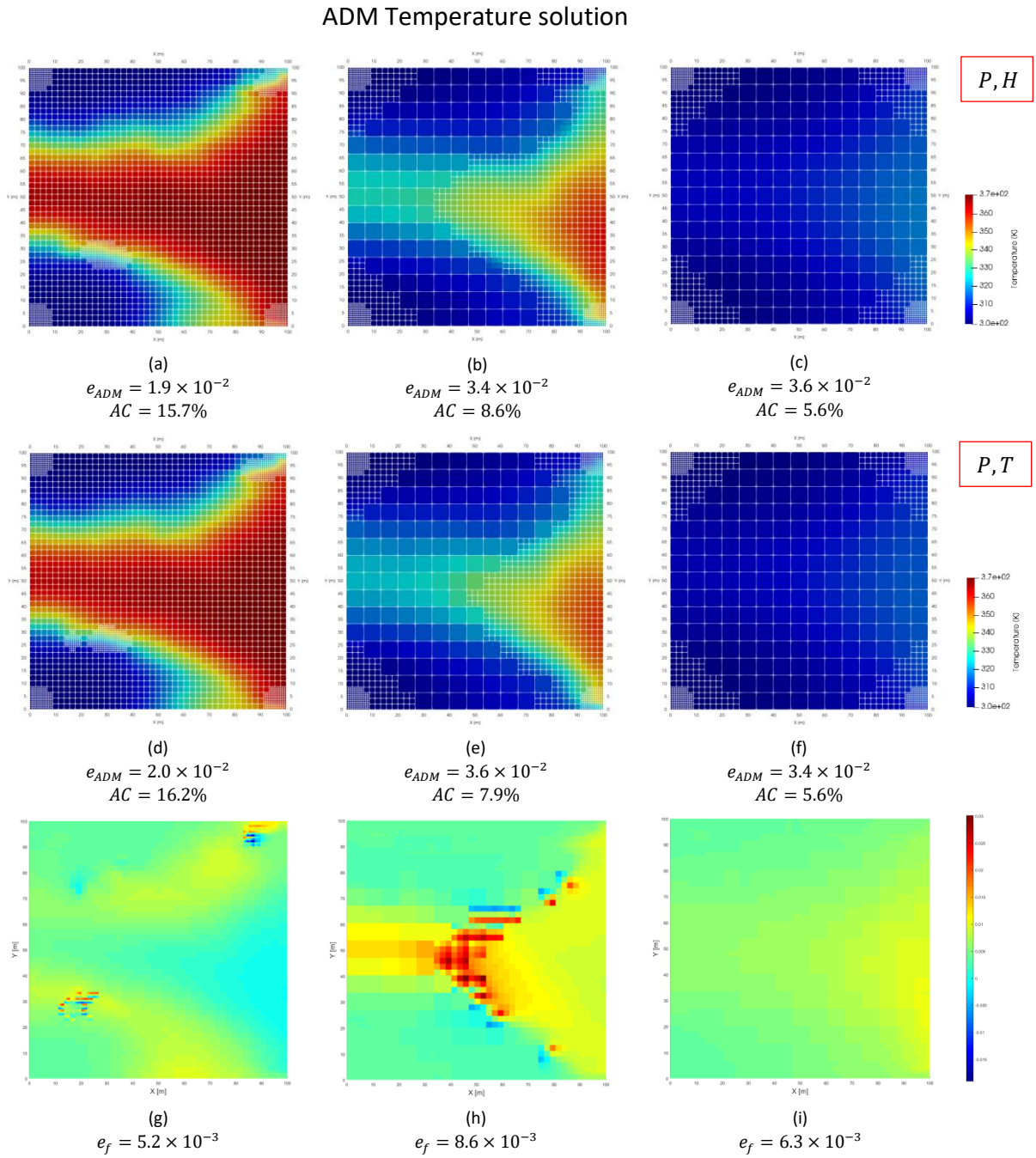

(a) $e_{ADM} = 1.9 \times 10^{-2}$, $AC = 15.7\%$

(b) $e_{ADM} = 3.4 \times 10^{-2}$, $AC = 8.6\%$

(c) $e_{ADM} = 3.6 \times 10^{-2}$, $AC = 5.6\%$

(d) $e_{ADM} = 2.0 \times 10^{-2}$, $AC = 16.2\%$

(e) $e_{ADM} = 3.6 \times 10^{-2}$, $AC = 7.9\%$

(f) $e_{ADM} = 3.4 \times 10^{-2}$, $AC = 5.6\%$

(g) $e_f = 5.2 \times 10^{-3}$

(h) $e_f = 8.6 \times 10^{-3}$

(i) $e_f = 6.3 \times 10^{-3}$

Figure 4.32: ADM simulation results of reservoir temperature for realization 1 of the Middenmeer geothermal field. The first and second rows show the results using the molar and natural formulation, respectively. The third row shows the error between the results of both formulations. Column wise, the simulation time increases from 400 to 1000 to 2000 [days]. The formulation error e_f indicates the relative difference between the solutions obtained from both formulations.

The algebraic dynamic multilevel (ADM) simulation results of the reservoir enthalpy are presented in figure 4.33.

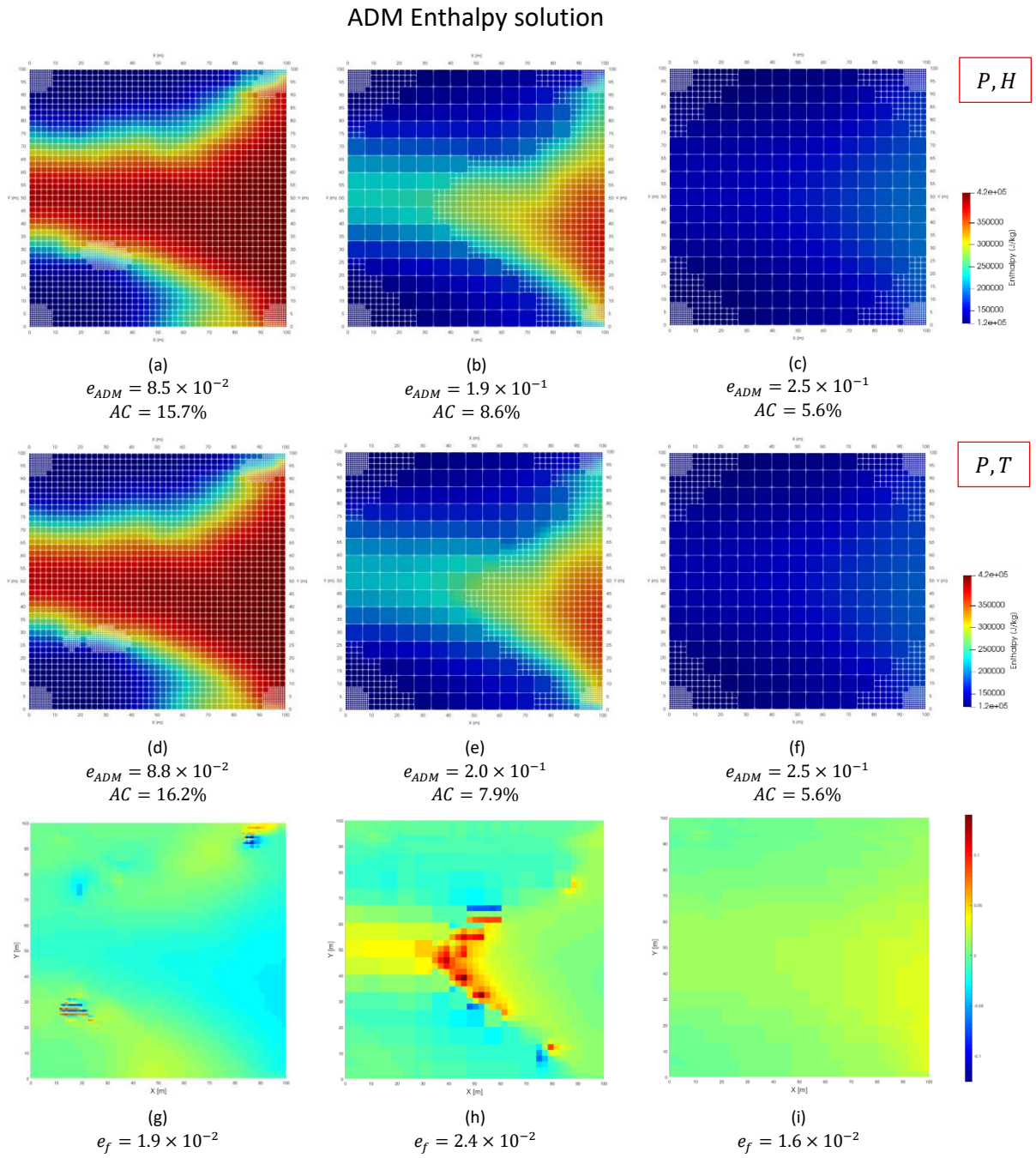

Figure 4.33: ADM simulation results of reservoir enthalpy for realization 1 of the Middenmeer geothermal field. The first and second rows show the results using the molar and natural formulation, respectively. The third row shows the error between the results of both formulations. Column wise, the simulation time increases from 400 to 1000 to 2000 [days]. The formulation error e_f indicates the relative difference between the solutions obtained from both formulations.

The error between both formulations in terms of reservoir pressure, temperature and enthalpy is presented in figure 4.34. The error is presented for both fine-scale and ADM simulation over the total number of timesteps.

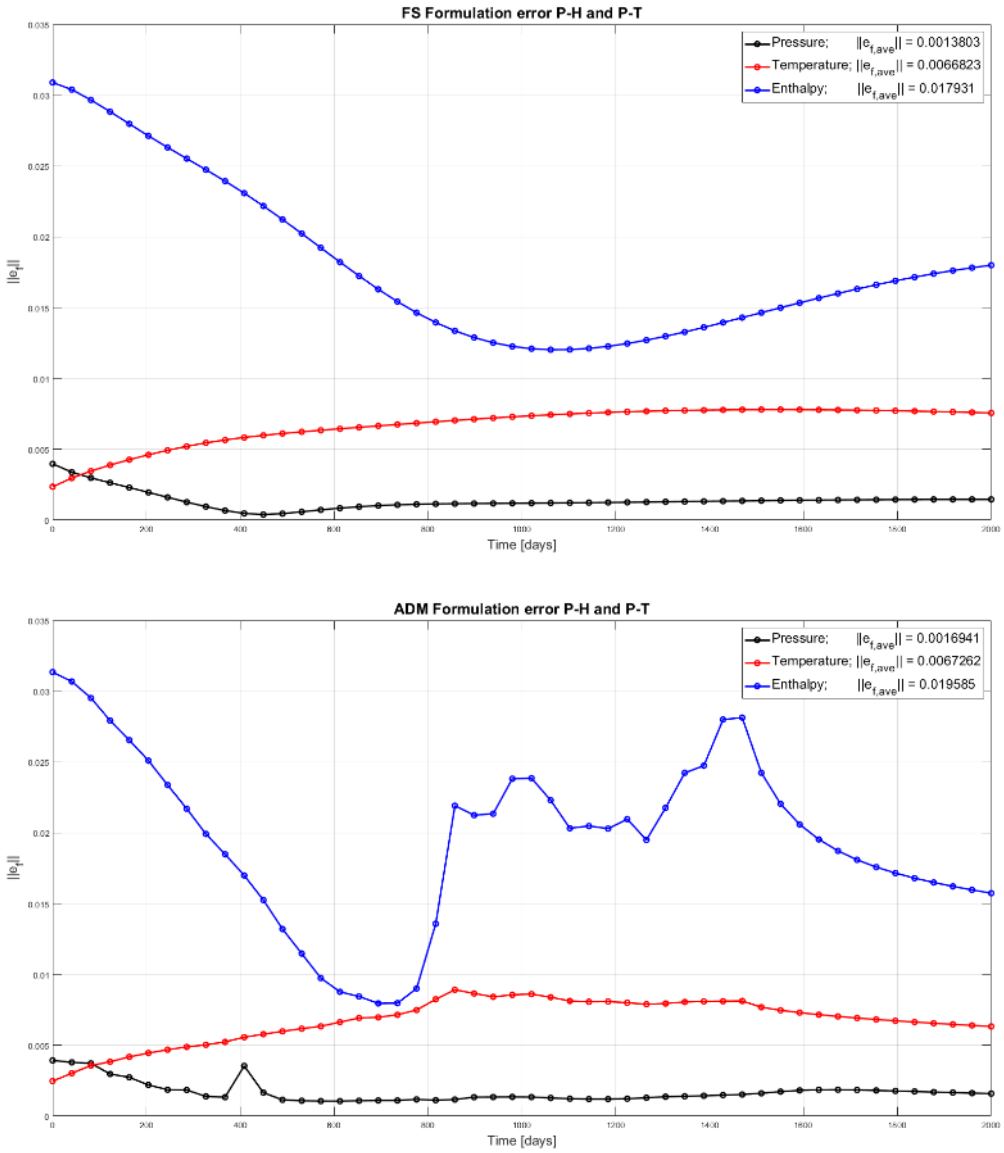

Figure 4.34: Pressure, temperature and enthalpy error between the molar and natural formulation e_f, for fine-scale (top) and ADM (bottom) simulations. The formulation error e_f indicates the relative difference between the solutions obtained from both formulations.

The performance comparison between both formulations is presented in figure 4.35, for both fine-scale and ADM simulations.

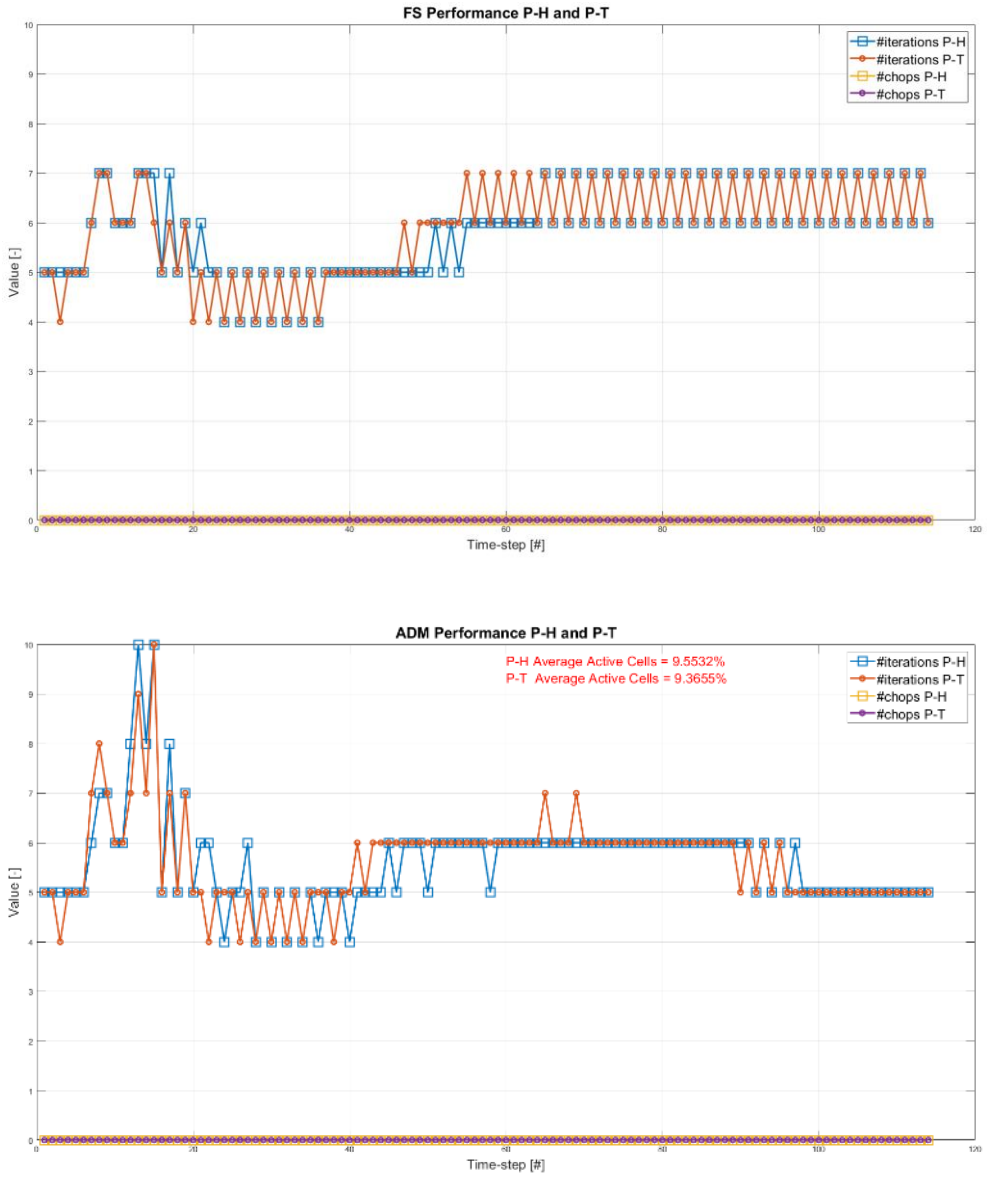

Figure 4.35: Fine-scale (top) and ADM (bottom) simulation performance for both formulations. The performance is compared at each timestep. Note that the average number of active cells during the entire simulation is marked in red in the ADM performance chart.

4.5. Middenmeer – Realization 2

The second realization of the Middenmeer geothermal field is one with a fracture network that consists of 15 fractures. The fine-scale simulation results of the reservoir pressure are presented in figure 4.36. The pressure solution using the molar formulation is presented in subfigures (a), (b) and (c), and the pressure solution using the natural formulation is presented in subfigures (d), (e) and (f) for simulation times of 400, 1000 and 2000 [days], respectively. Subfigures (g), (h) and (i) show the error e_f between the solutions of both formulations at the respective simulation times.

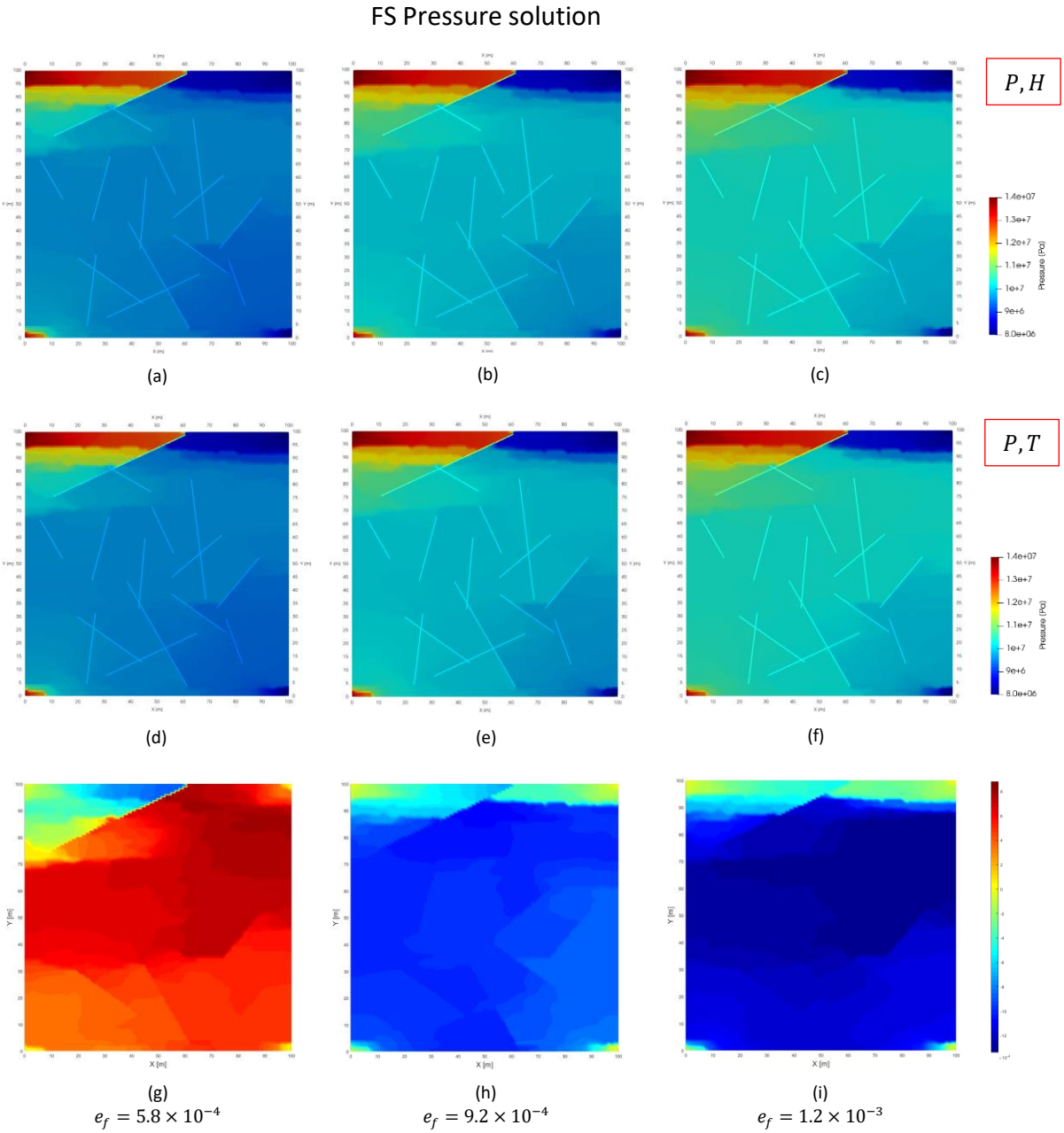

Figure 4.36: Fine-scale simulation results of reservoir pressure for realization 2 of the Middenmeer geothermal field. The first and second rows show the results using the molar and natural formulation, respectively. The third row shows the error between the results of both formulations. Column wise, the simulation time increases from 400 to 1000 to 2000 [days]. The formulation error e_f indicates the relative difference between the solutions obtained from both formulations.

The fine-scale simulation results of the reservoir temperature are presented in figure 4.37.

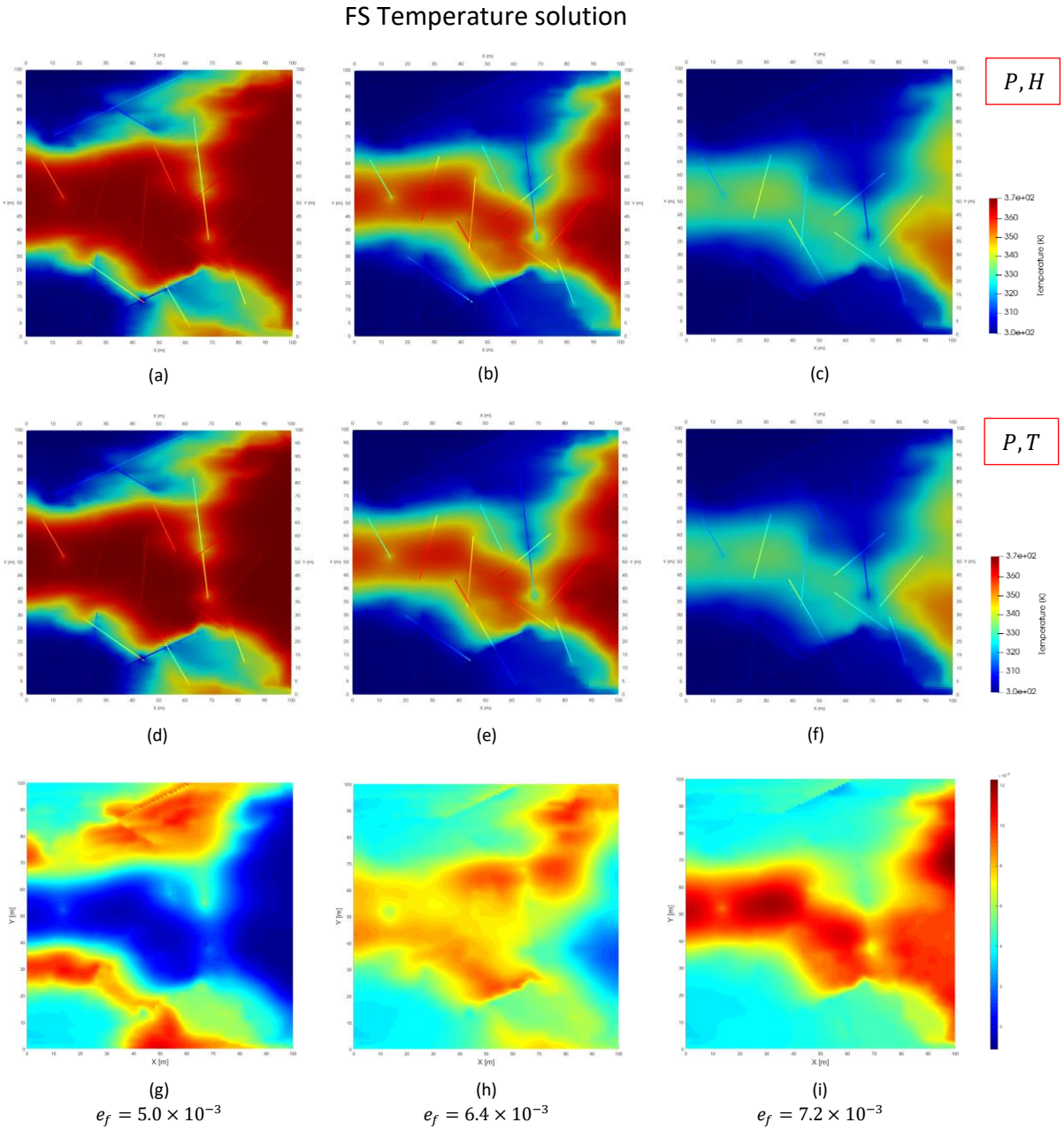

Figure 4.37: Fine-scale simulation results of reservoir temperature for realization 2 of the Middenmeer geothermal field. The first and second rows show the results using the molar and natural formulation, respectively. The third row shows the error between the results of both formulations. Column wise, the simulation time increases from 400 to 1000 to 2000 [days]. The formulation error e_f indicates the relative difference between the solutions obtained from both formulations.

The fine-scale simulation results of the reservoir enthalpy are presented in figure 4.38.

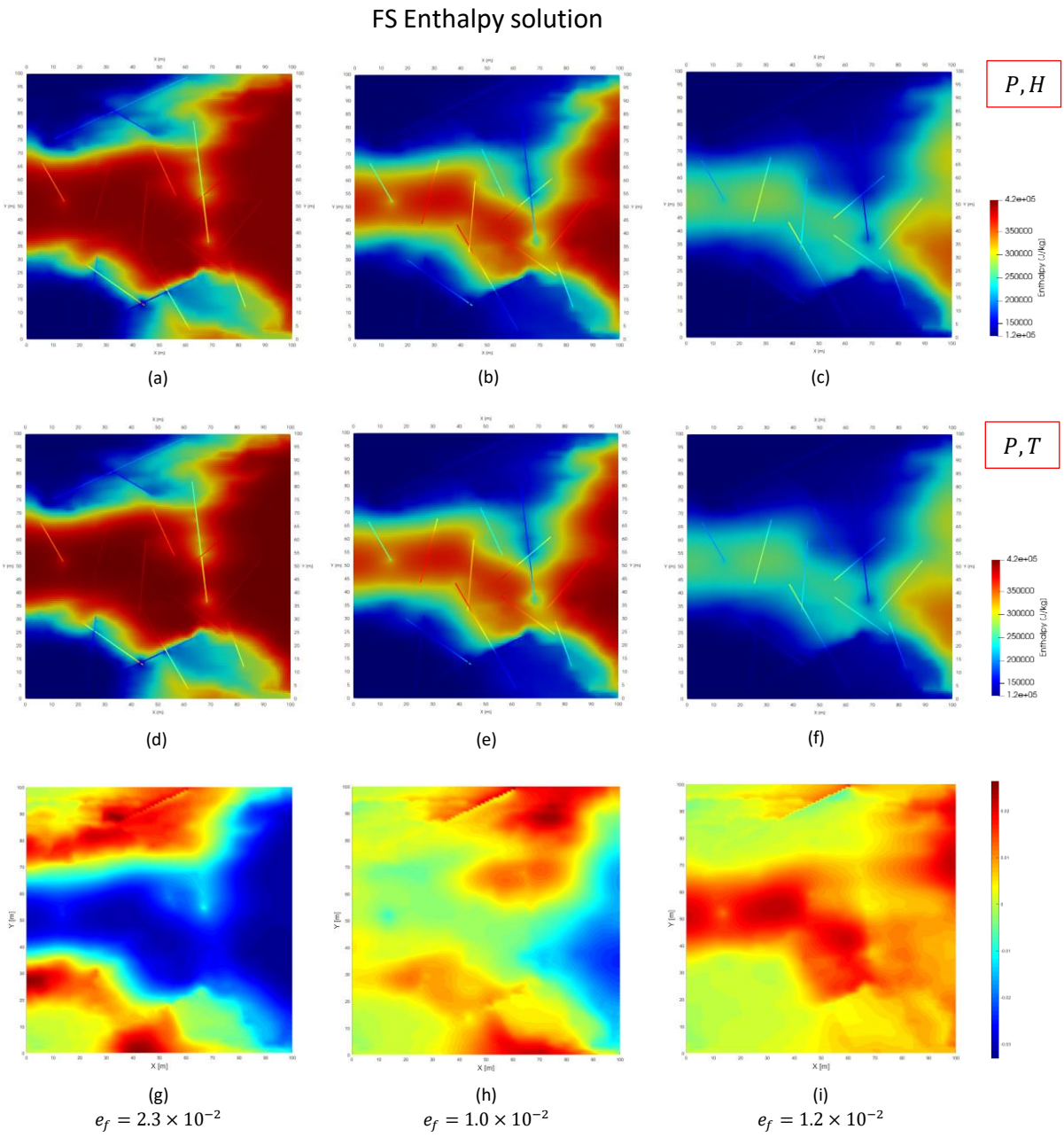

Figure 4.38: Fine-scale simulation results of reservoir enthalpy for realization 2 of the Middenmeer geothermal field. The first and second rows show the results using the molar and natural formulation, respectively. The third row shows the error between the results of both formulations. Column wise, the simulation time increases from 400 to 1000 to 2000 [days]. The formulation error e_f indicates the relative difference between the solutions obtained from both formulations.

The algebraic dynamic multilevel (ADM) simulation results of the reservoir pressure are presented in figure 4.39.

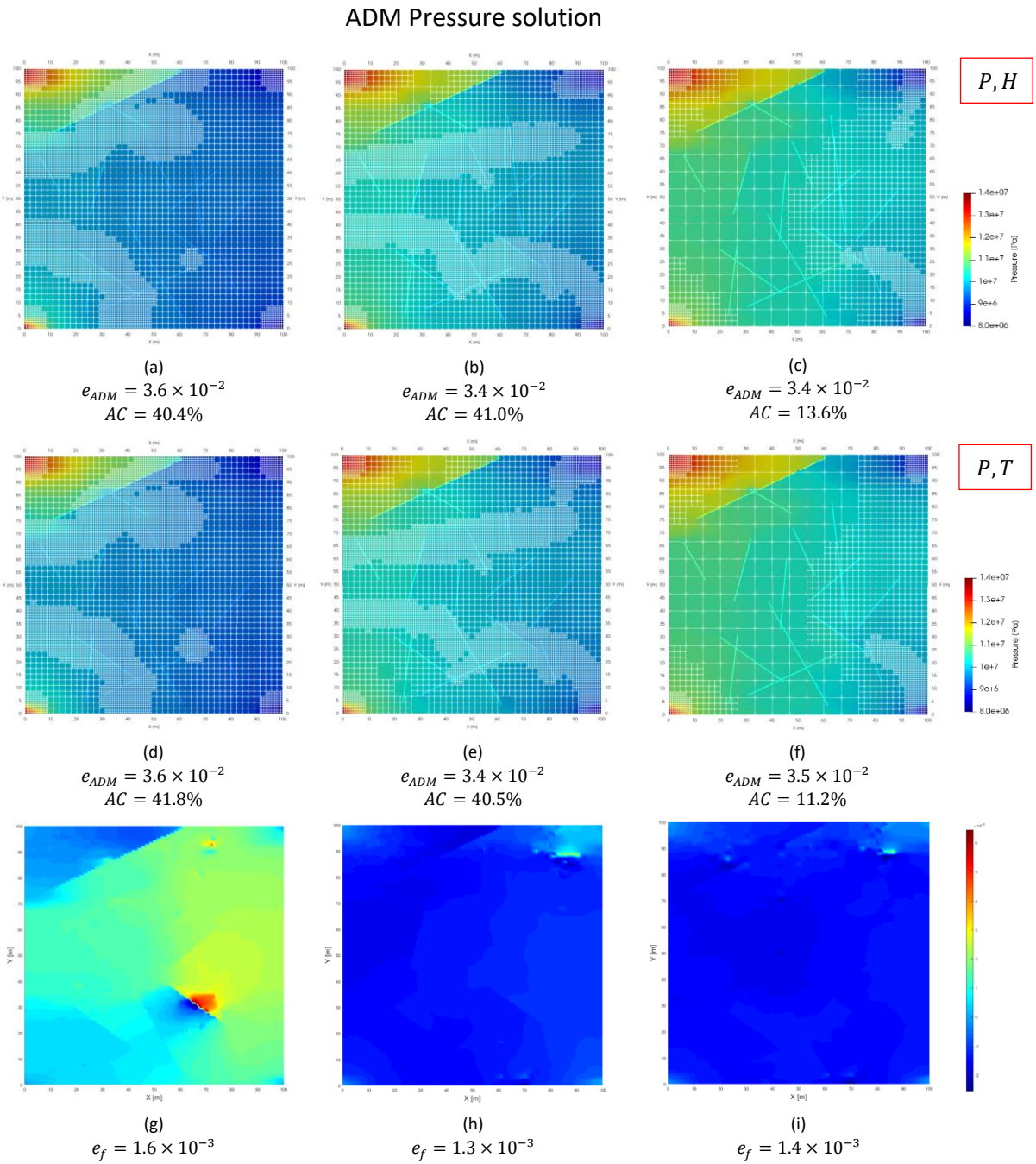

Figure 4.39: ADM simulation results of reservoir pressure for realization 2 of the Middenmeer geothermal field. The first and second rows show the results using the molar and natural formulation, respectively. The third row shows the error between the results of both formulations. Column wise, the simulation time increases from 400 to 1000 to 2000 [days]. The formulation error e_f indicates the relative difference between the solutions obtained from both formulations.

The algebraic dynamic multilevel (ADM) simulation results of the reservoir temperature are presented in figure 4.40.

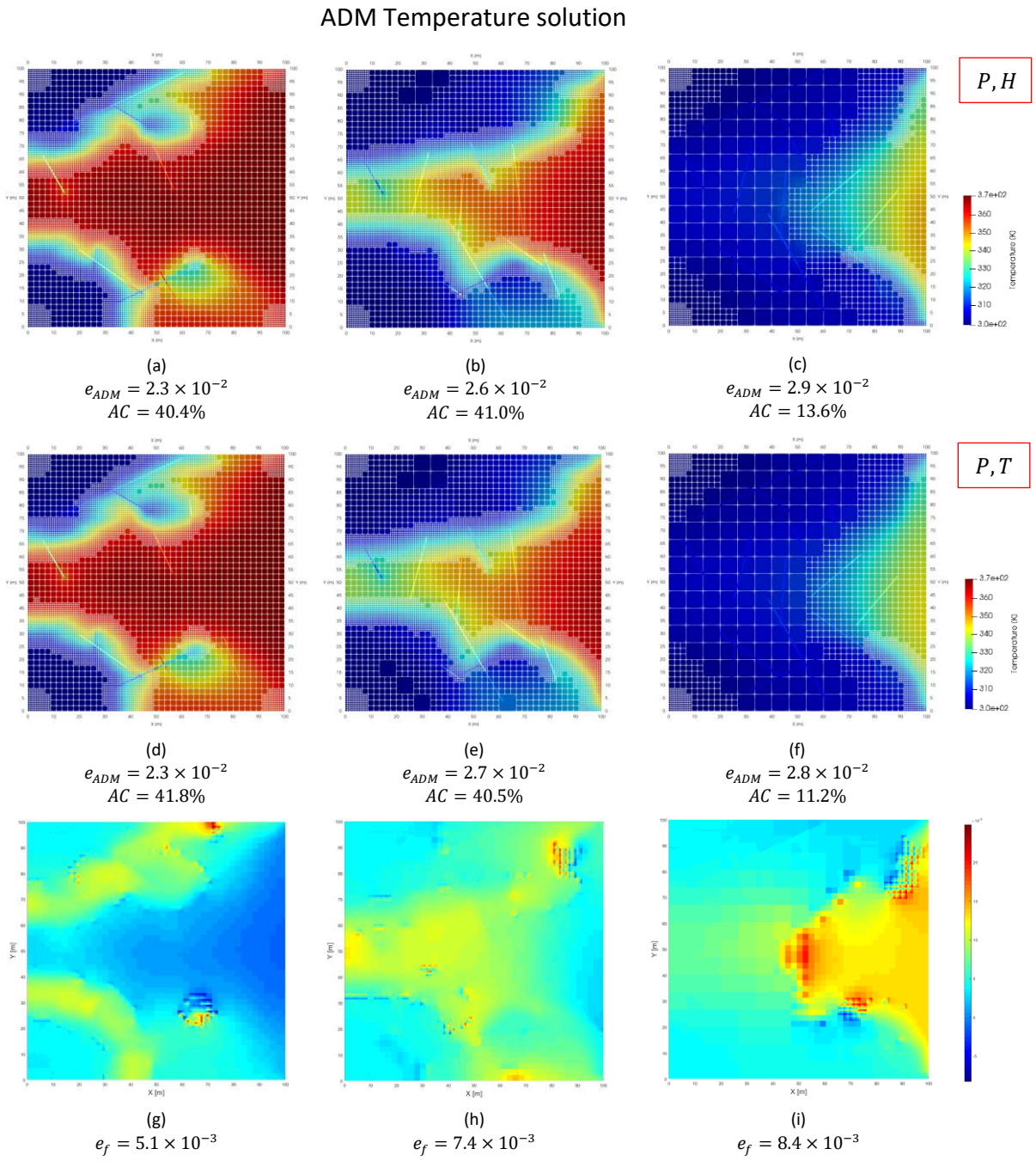

Figure 4.40: ADM simulation results of reservoir temperature for realization 2 of the Middenmeer geothermal field. The first and second rows show the results using the molar and natural formulation, respectively. The third row shows the error between the results of both formulations. Column wise, the simulation time increases from 400 to 1000 to 2000 [days]. The formulation error e_f indicates the relative difference between the solutions obtained from both formulations.

The algebraic dynamic multilevel (ADM) simulation results of the reservoir enthalpy are presented in figure 4.41.

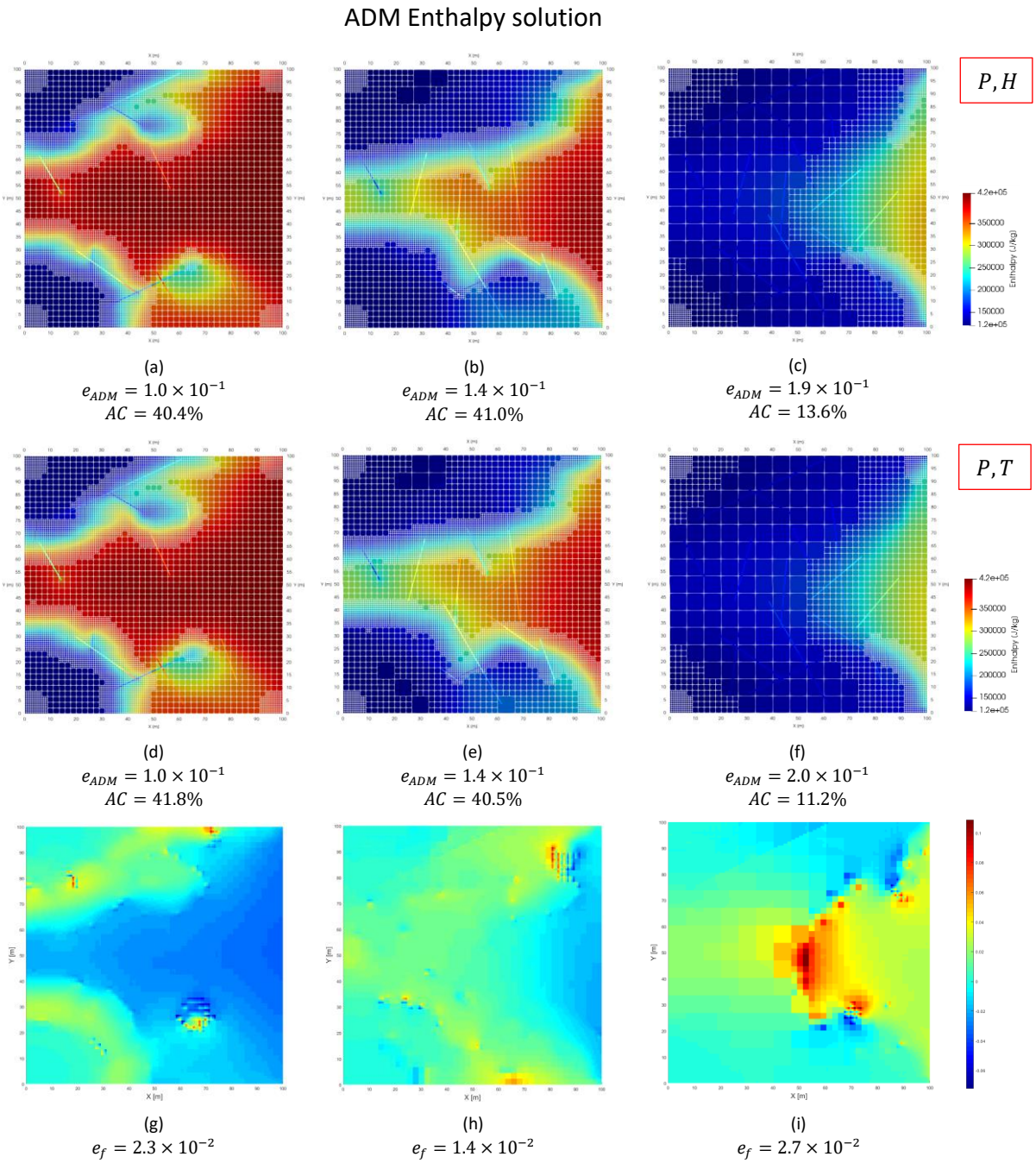

Figure 4.41: ADM simulation results of reservoir enthalpy for realization 2 of the Middenmeer geothermal field. The first and second rows show the results using the molar and natural formulation, respectively. The third row shows the error between the results of both formulations. Column wise, the simulation time increases from 400 to 1000 to 2000 [days]. The formulation error e_f indicates the relative difference between the solutions obtained from both formulations.

The error between both formulations in terms of reservoir pressure, temperature and enthalpy is presented in figure 4.42. The error is presented for both fine-scale and ADM simulation over the total number of timesteps. Note that the permeability contrast has been decreased for the ADM simulations. In addition, the ADM threshold for the grid selection has been increased, i.e. $\Delta T = 10\ [K]$.

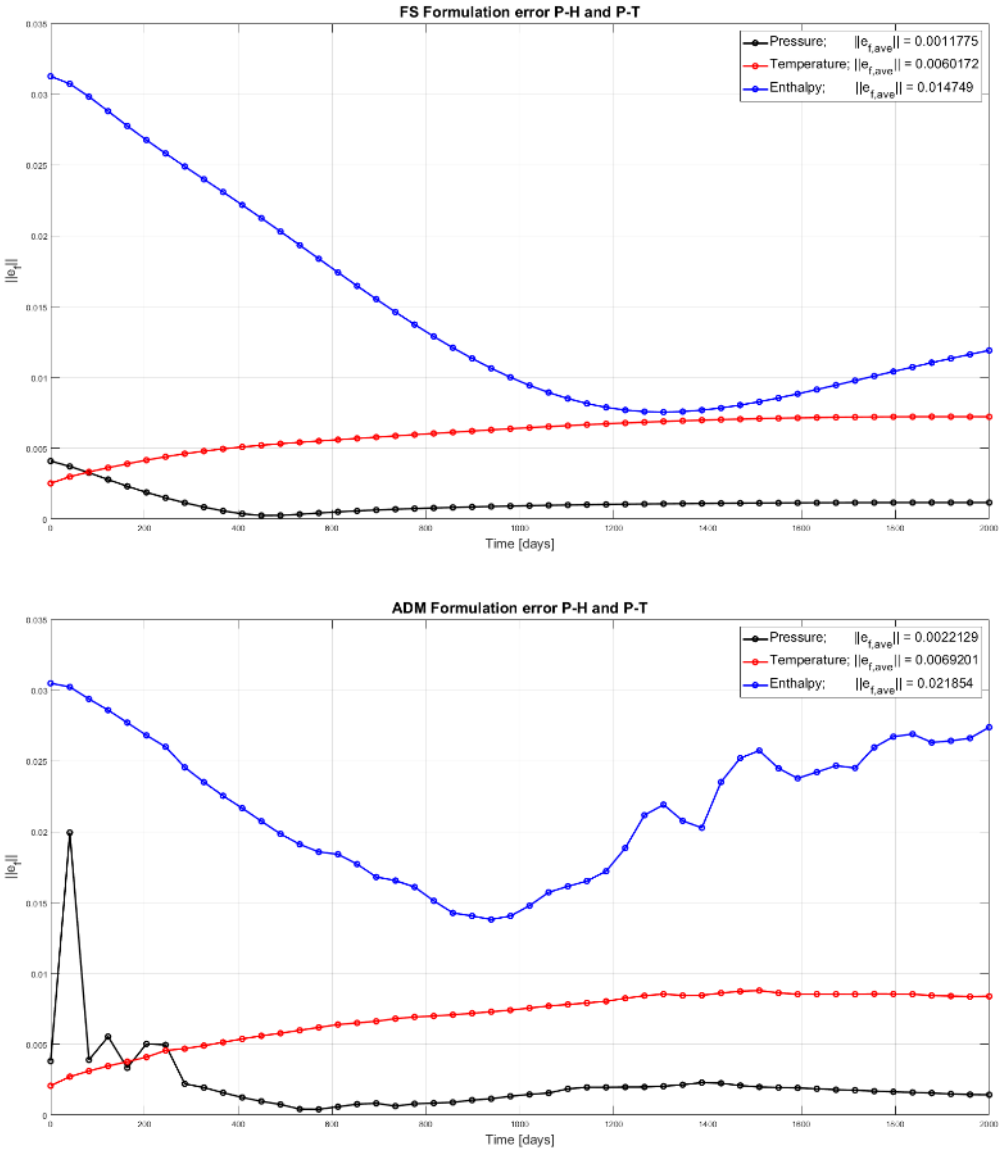

Figure 4.42: Pressure, temperature and enthalpy error between the molar and natural formulation e_f, for fine-scale (top) and ADM (bottom) simulations. The formulation error e_f indicates the relative difference between the solutions obtained from both formulations.

The performance comparison between both formulations is presented in figure 4.43, for both fine-scale and ADM simulations. Note that the permeability contrast has been decreased for the ADM simulations. In addition, the ADM threshold for the grid selection has been increased, i.e. $\Delta T = 10\ [K]$.

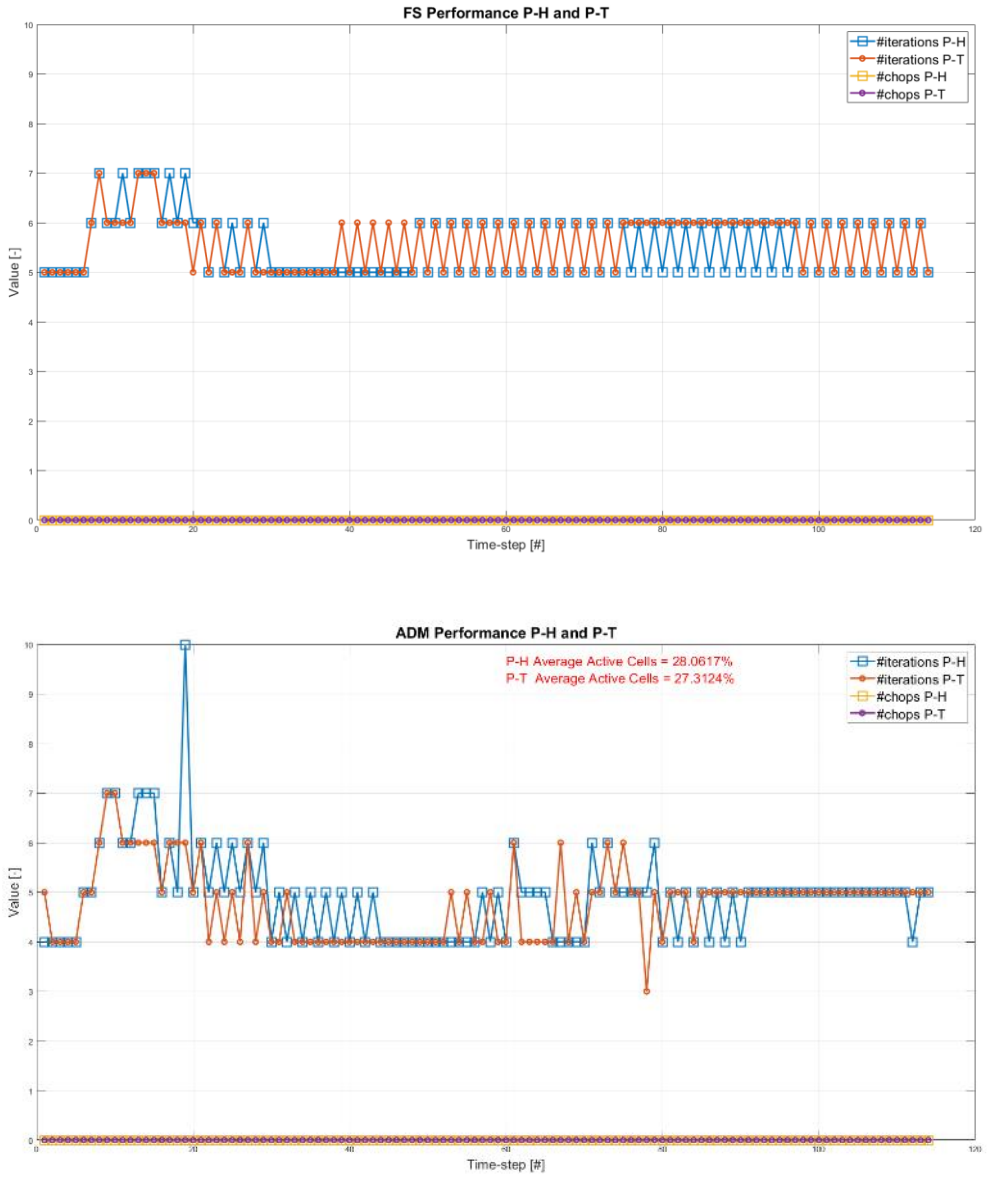

Figure 4.43: Fine-scale (top) and ADM (bottom) simulation performance for both formulations. The performance is compared at each timestep. Note that the average number of active cells during the entire simulation is marked in red in the ADM performance chart.

4.6. Middenmeer – Realization 3

The third realization of the Middenmeer geothermal field is one with a fracture network that consists of 30 fractures. The fine-scale simulation results of the reservoir pressure are presented in figure 4.44. The pressure solution using the molar formulation is presented in subfigures (a), (b) and (c), and the pressure solution using the natural formulation is presented in subfigures (d), (e) and (f) for simulation times of 400, 1000 and 2000 [days], respectively. Subfigures (g), (h) and (i) show the error e_f between the solutions of both formulations at the respective simulation times.

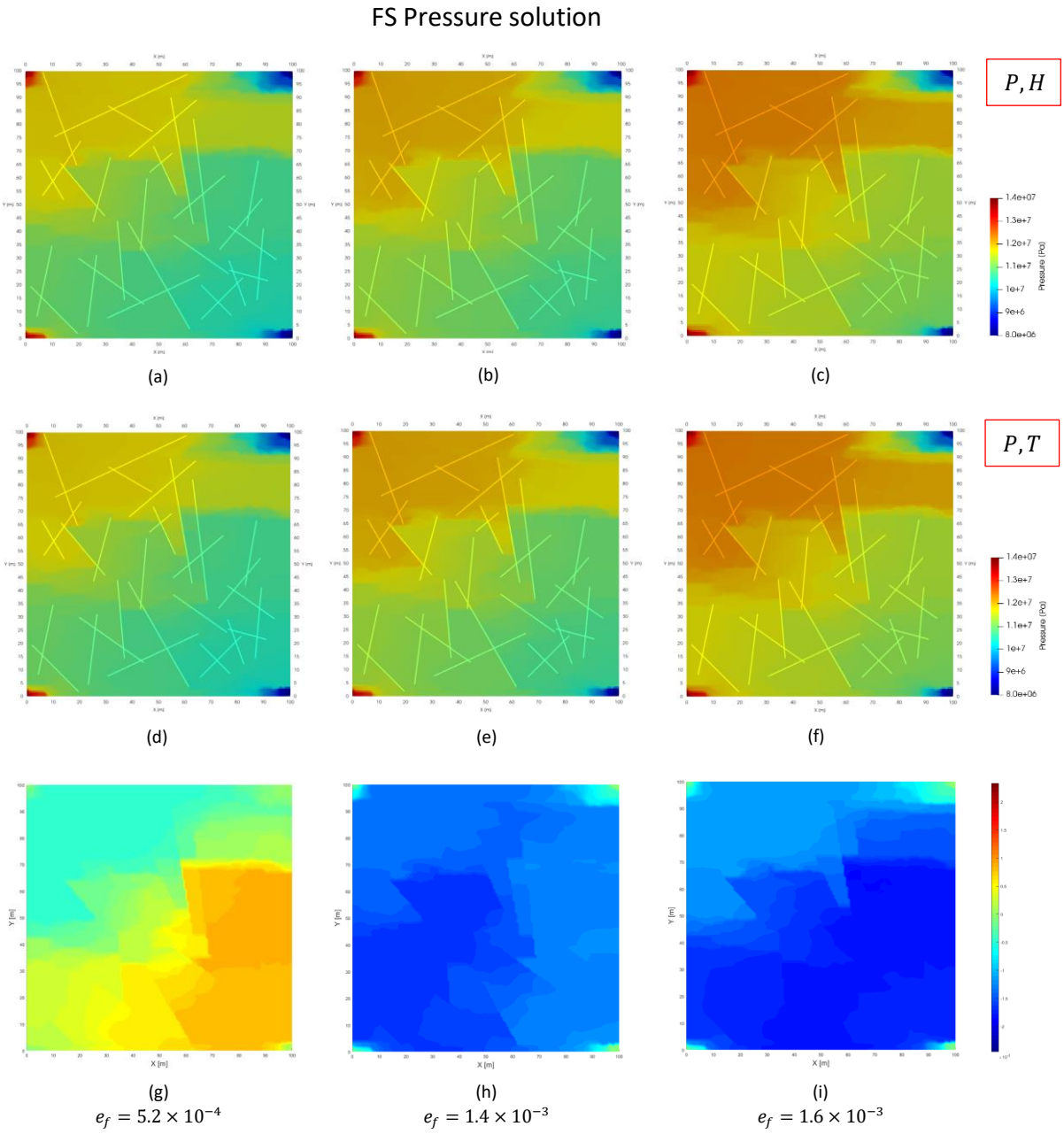

Figure 4.44: Fine-scale simulation results of reservoir pressure for realization 3 of the Middenmeer geothermal field. The first and second rows show the results using the molar and natural formulation, respectively. The third row shows the error between the results of both formulations. Column wise, the simulation time increases from 200 to 400 to 1000 [days]. The formulation error e_f indicates the relative difference between the solutions obtained from both formulations.

The fine-scale simulation results of the reservoir temperature are presented in figure 4.45.

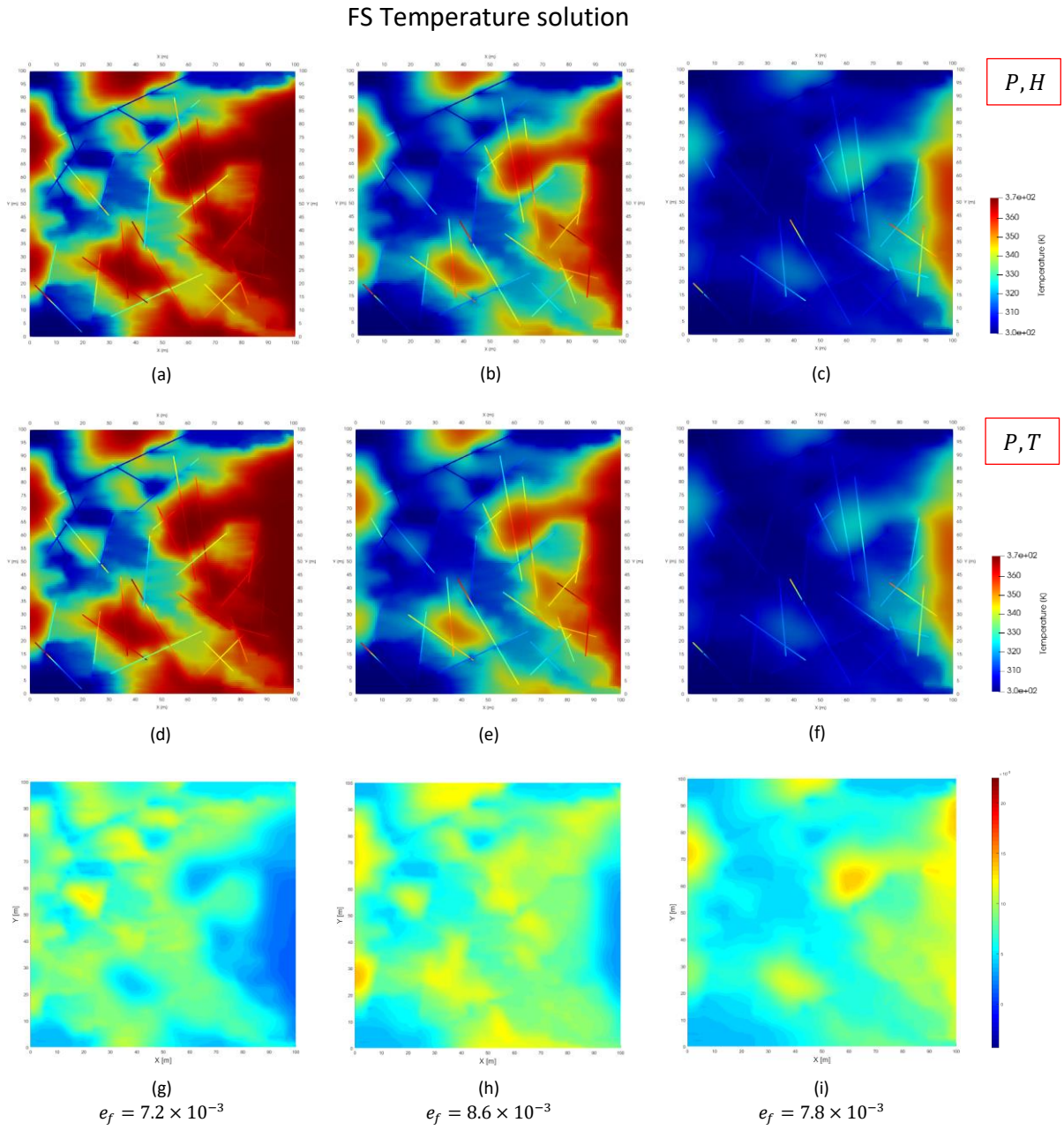

Figure 4.45: Fine-scale simulation results of reservoir temperature for realization 3 of the Middenmeer geothermal field. The first and second rows show the results using the molar and natural formulation, respectively. The third row shows the error between the results of both formulations. Column wise, the simulation time increases from 200 *to* 400 *to* 1000 *[days]. The formulation error* e_f *indicates the relative difference between the solutions obtained from both formulations.*

The fine-scale simulation results of the reservoir enthalpy are presented in figure 4.46.

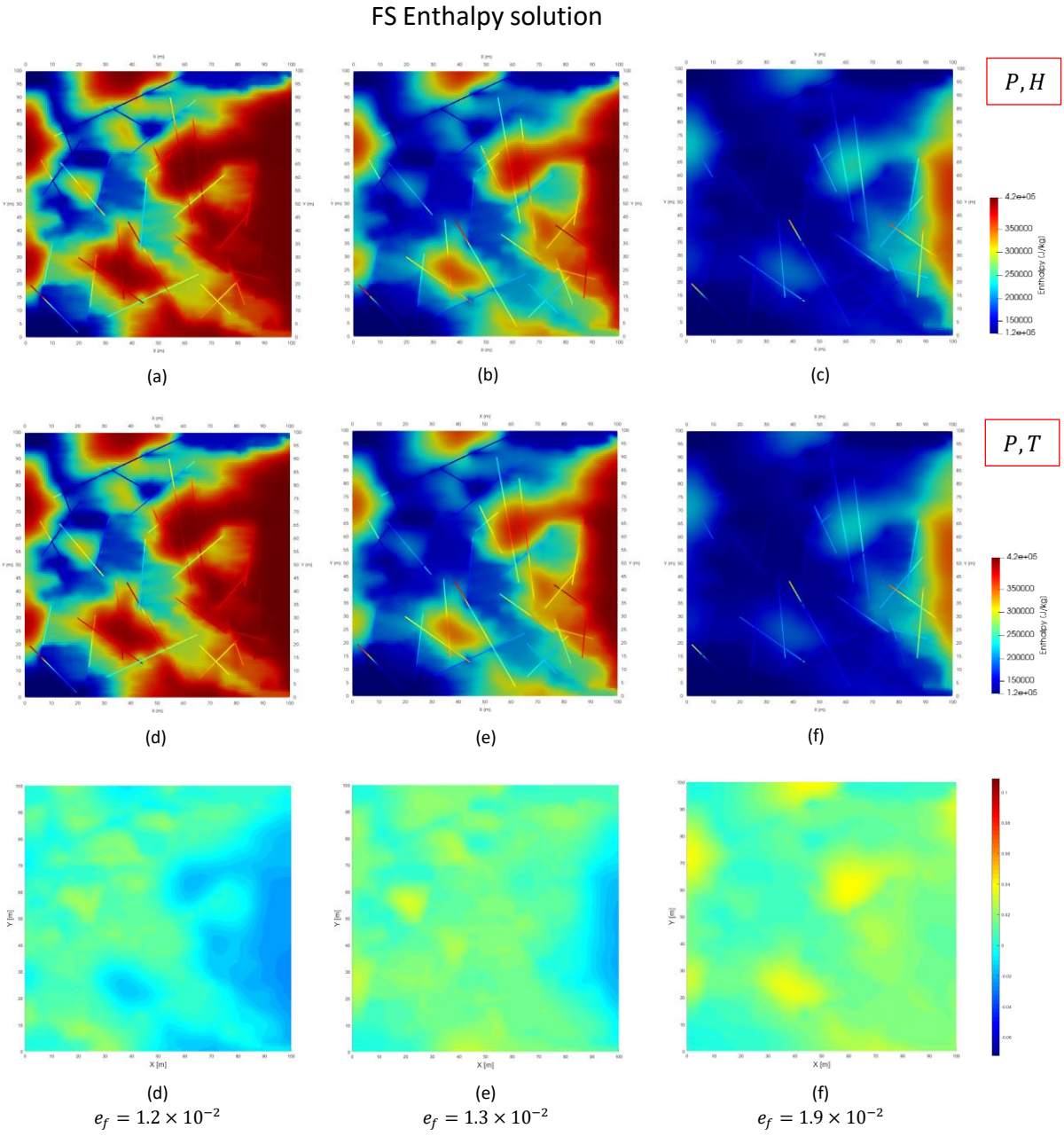

Figure 4.46: Fine-scale simulation results of reservoir enthalpy for realization 3 of the Middenmeer geothermal field. The first and second rows show the results using the molar and natural formulation, respectively. The third row shows the error between the results of both formulations. Column wise, the simulation time increases from 200 *to* 400 *to* 1000 *[days]. The formulation error* e_f *indicates the relative difference between the solutions obtained from both formulations.*

The algebraic dynamic multilevel (ADM) simulation results of the reservoir pressure are presented in figure 4.47.

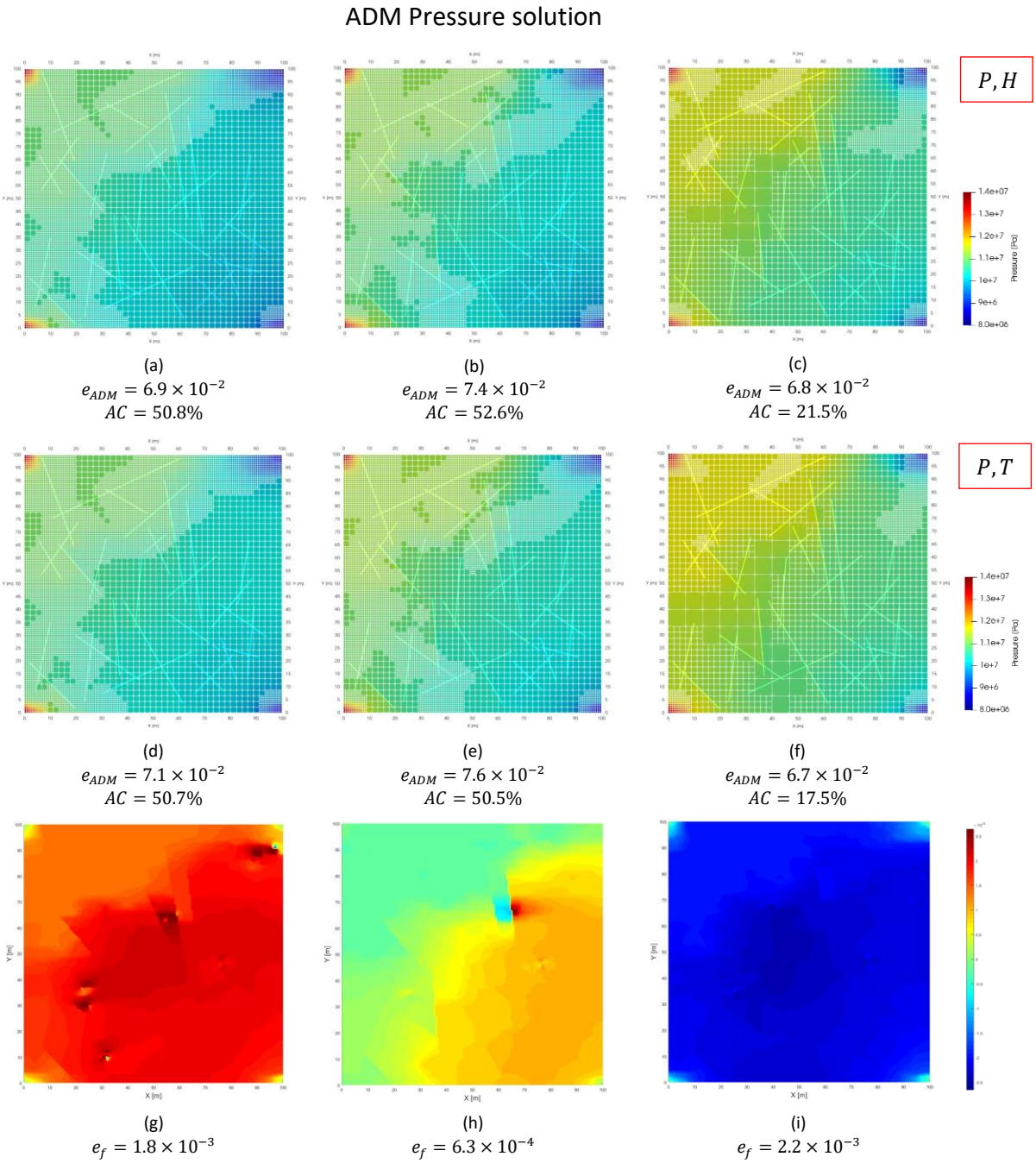

(a)
$e_{ADM} = 6.9 \times 10^{-2}$
$AC = 50.8\%$

(b)
$e_{ADM} = 7.4 \times 10^{-2}$
$AC = 52.6\%$

(c)
$e_{ADM} = 6.8 \times 10^{-2}$
$AC = 21.5\%$

(d)
$e_{ADM} = 7.1 \times 10^{-2}$
$AC = 50.7\%$

(e)
$e_{ADM} = 7.6 \times 10^{-2}$
$AC = 50.5\%$

(f)
$e_{ADM} = 6.7 \times 10^{-2}$
$AC = 17.5\%$

(g)
$e_f = 1.8 \times 10^{-3}$

(h)
$e_f = 6.3 \times 10^{-4}$

(i)
$e_f = 2.2 \times 10^{-3}$

Figure 4.47: ADM simulation results of reservoir pressure for realization 3 of the Middenmeer geothermal field. The first and second rows show the results using the molar and natural formulation, respectively. The third row shows the error between the results of both formulations. Column wise, the simulation time increases from 200 to 400 to 1000 [days]. The formulation error e_f indicates the relative difference between the solutions obtained from both formulations.

The algebraic dynamic multilevel (ADM) simulation results of the reservoir temperature are presented in figure 4.48.

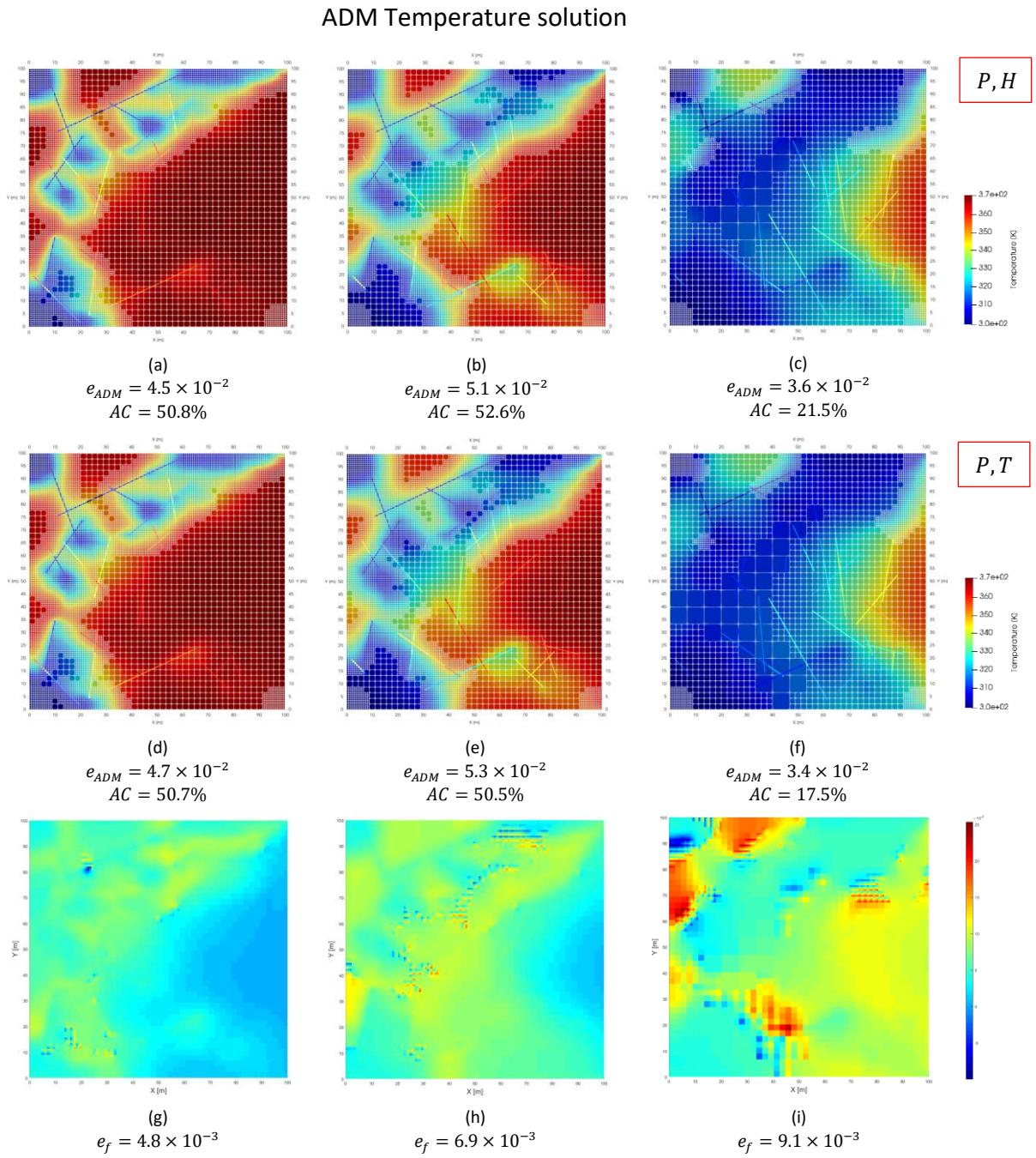

Figure 4.48: ADM simulation results of reservoir temperature for realization 3 of the Middenmeer geothermal field. The first and second rows show the results using the molar and natural formulation, respectively. The third row shows the error between the results of both formulations. Column wise, the simulation time increases from 200 to 400 to 1000 [days]. The formulation error e_f indicates the relative difference between the solutions obtained from both formulations.

The algebraic dynamic multilevel (ADM) simulation results of the reservoir enthalpy are presented in figure 4.49.

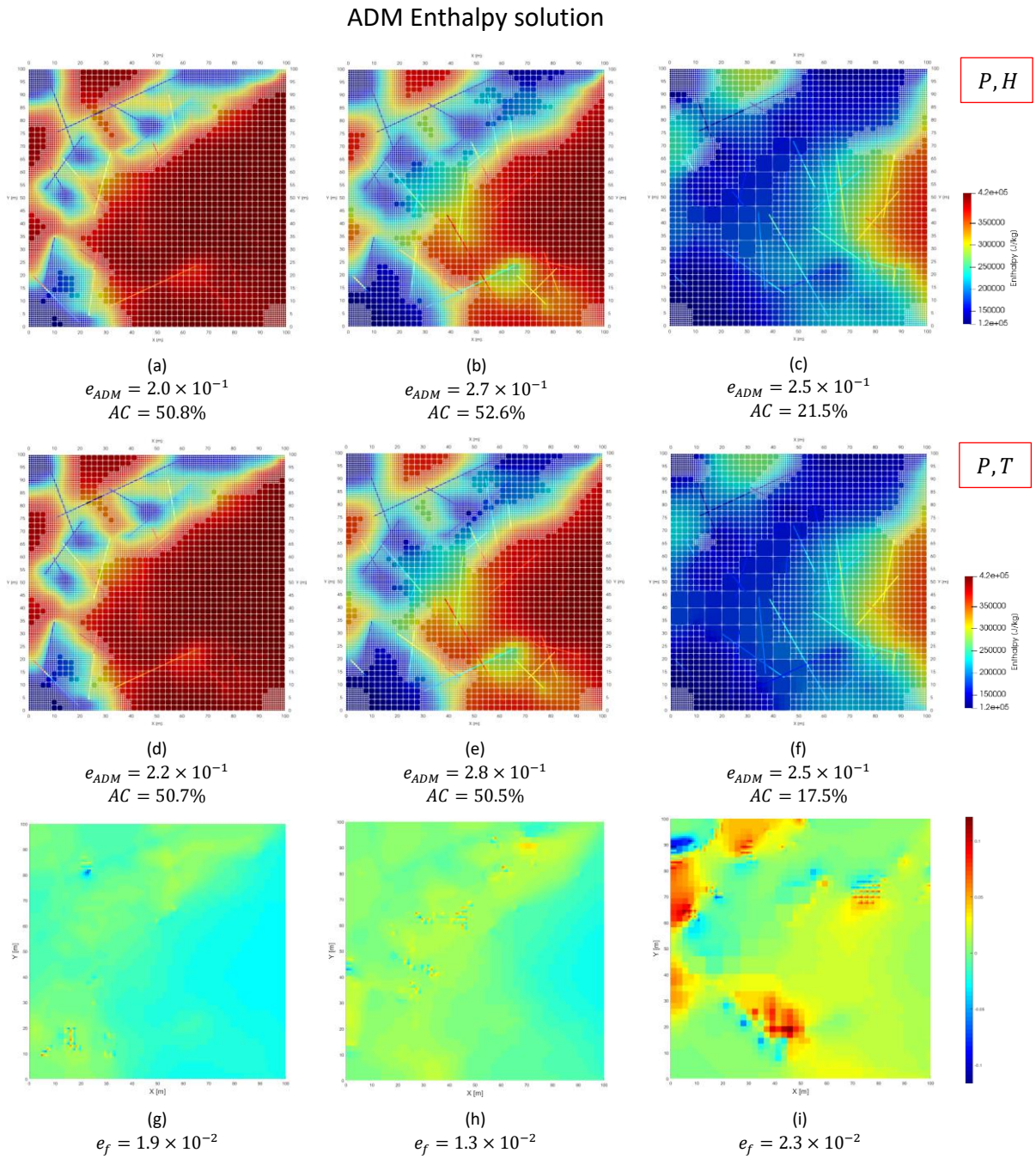

Figure 4.49: ADM simulation results of reservoir enthalpy for realization 3 of the Middenmeer geothermal field. The first and second rows show the results using the molar and natural formulation, respectively. The third row shows the error between the results of both formulations. Column wise, the simulation time increases from 200 to 400 to 1000 [days]. The formulation error e_f indicates the relative difference between the solutions obtained from both formulations.

The error between both formulations in terms of reservoir pressure, temperature and enthalpy is presented in figure 4.50. The error is presented for both fine-scale and ADM simulation over the total number of timesteps. Note that the permeability contrast has been decreased for the ADM simulations. In addition, the ADM threshold for the grid selection has been increased, i.e. $\Delta T = 10\ [K]$.

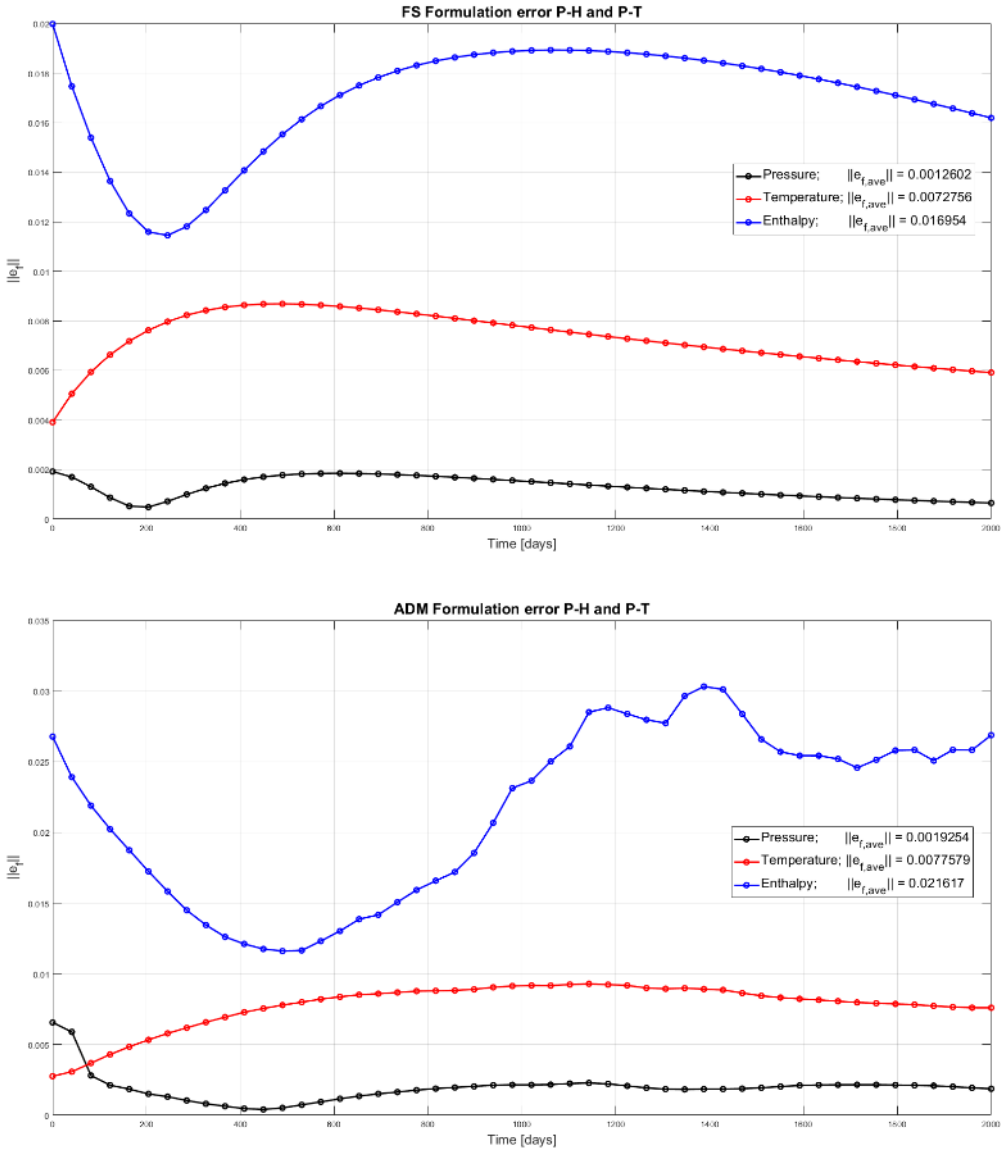

Figure 4.50: Pressure, temperature and enthalpy error between the molar and natural formulation e_f, for fine-scale (top) and ADM (bottom) simulations. The formulation error e_f indicates the relative difference between the solutions obtained from both formulations.

The performance comparison between both formulations is presented in figure 4.51, for both fine-scale and ADM simulations. Note that the permeability contrast has been decreased for the ADM simulations. In addition, the ADM threshold for the grid selection has been increased, i.e. $\Delta T = 10\ [K]$.

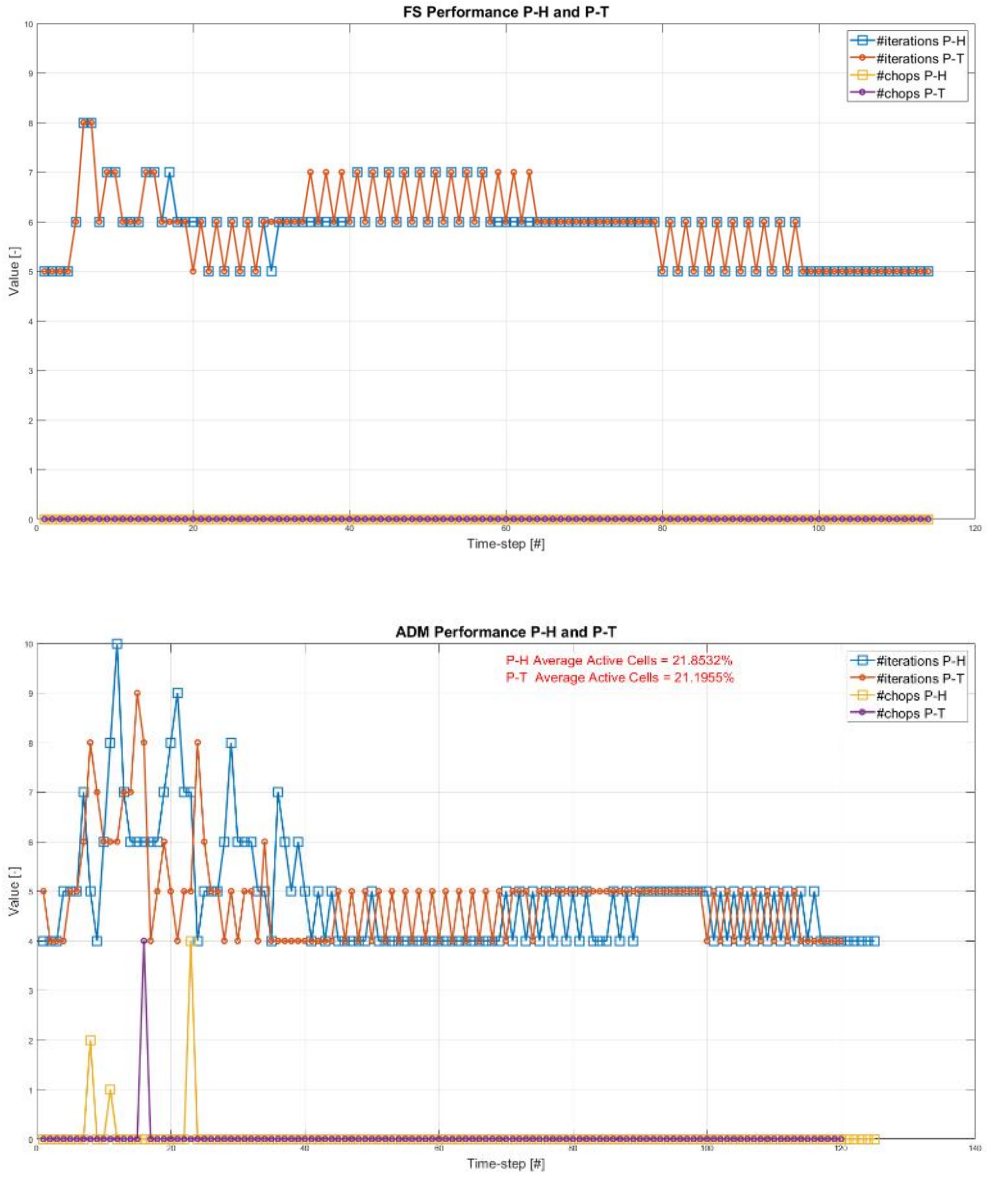

Figure 4.51: Fine-scale (top) and ADM (bottom) simulation performance for both formulations. The performance is compared at each timestep. Note that the average number of active cells during the entire simulation is marked in red in the ADM performance chart.

4.7. High-enthalpy fractured test case

The initial and boundary conditions of the 2nd realization of the Soultz-sous-Forêts geothermal field are modified in order to present a high-enthalpy (i.e. two-phase flow) test case of a fractured reservoir. The modified input parameters and initial reservoir conditions are presented in table 4.3.

	Value
$H_{initial}\ [J/kg]$	1.6×10^6
$T_{initial}\ [K]$	537
$T_{injection}\ [K]$	345
$P_{initial}\ [Pa]$	0.5×10^7
$P_{injection}\ [Pa]$	0.6×10^7
$P_{production}\ [Pa]$	0.4×10^7
$S_{w,initial}\ [-]$	0.28
$S_{w,injection}\ [-]$	1

Table 4.3: Modified simulation input parameters and initial reservoir conditions for the high-enthalpy test case.

The fine-scale simulation results of an unfractured one-dimensional model problem after the Soultz-sous-Forêts geothermal field are presented in figure 4.52.

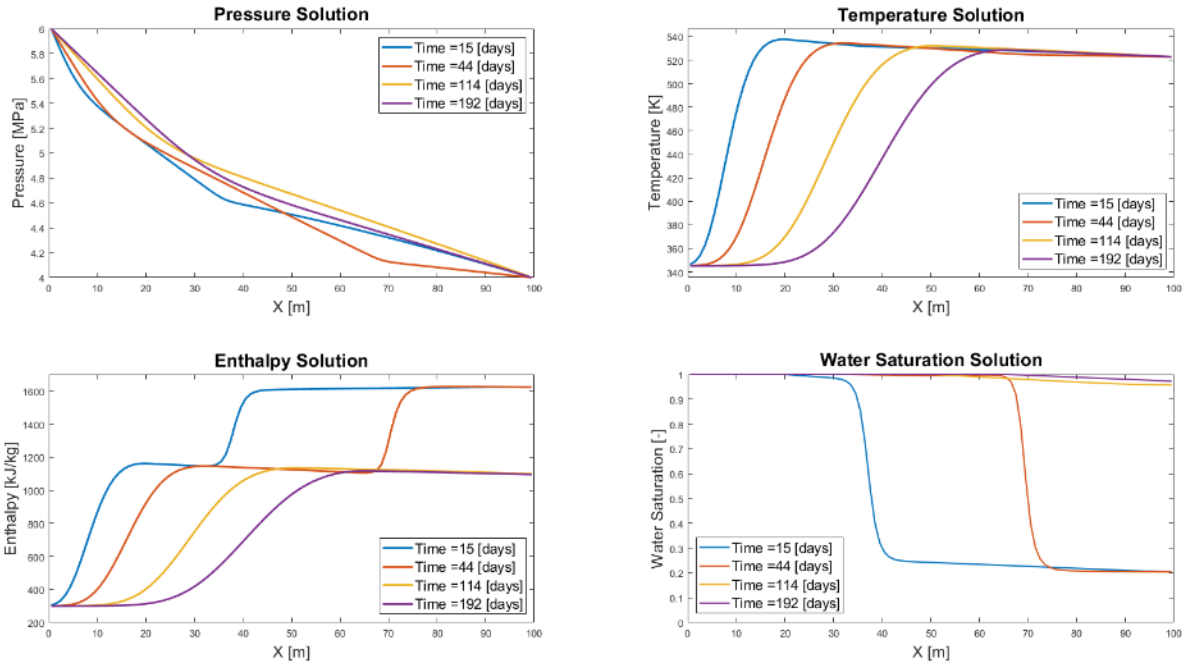

Figure 4.52: Multiphase simulation results of an arbitrary test case. Pressure, temperature, (mixture) enthalpy and water saturation solutions are presented at four different times.

The ADM simulation results of the (original) fractured two-dimensional realization are presented in figure 4.53 to illustrate the extended capabilities of the reservoir simulator and the applicability of the ADM and pEDFM methods for multiphase flow simulations. The (mixture) enthalpy solution is presented in subfigures (a), (b) and (c), the temperature solution is presented in subfigures (d), (e) and (f), and the water saturation solution is presented in subfigures (g), (h) and (i) for simulation times of 300, 500 and 1000 [days] respectively.

Note that separate ADM grid refinement thresholds $\Delta H = 1e5\ [J/kg]$ and $\Delta T = 15\ [K]$ are applied for the enthalpy and the temperature solutions, respectively. The threshold for the saturation solution is identical to that for the enthalpy solution.

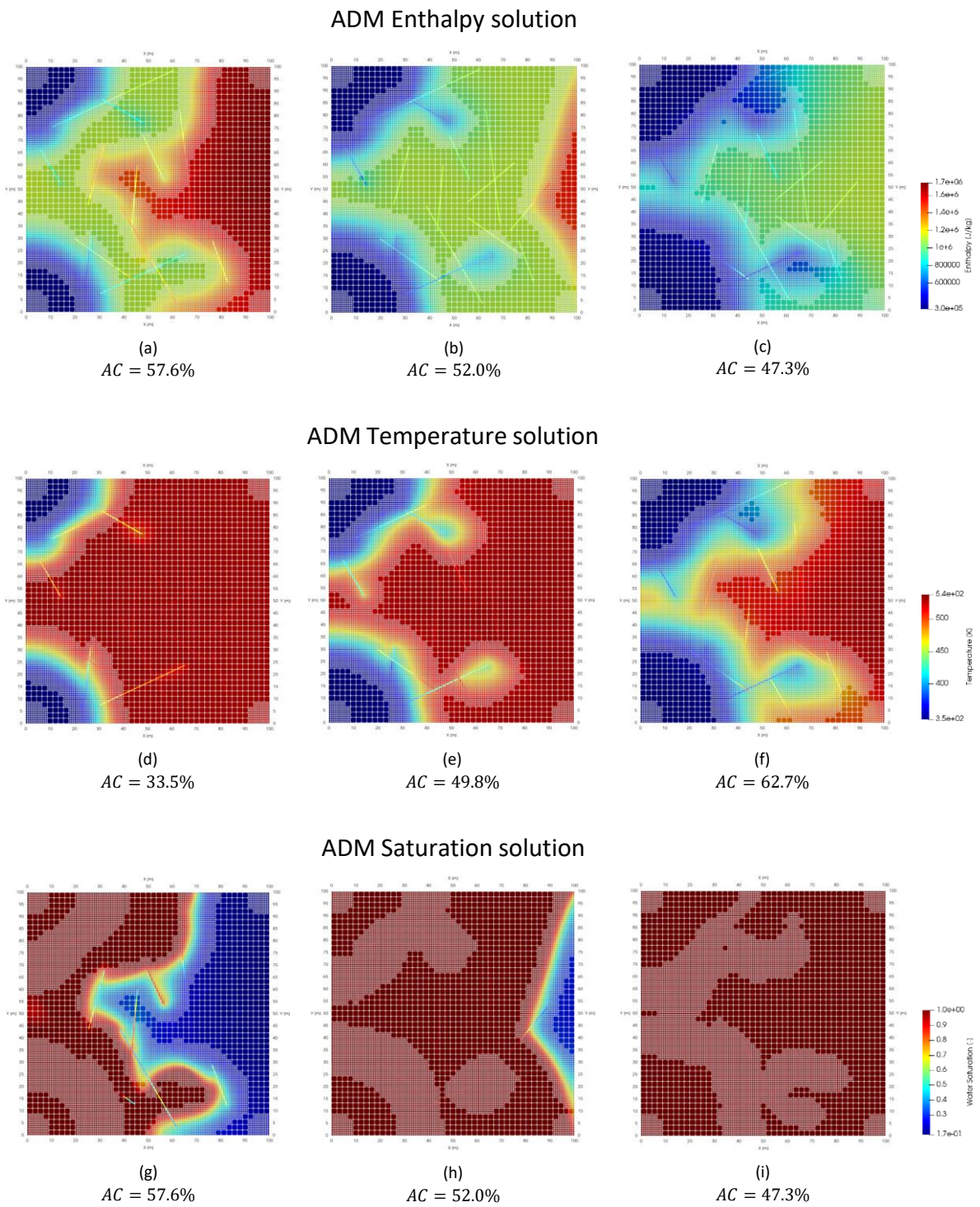

Figure 4.53: ADM simulation results of reservoir enthalpy (top row), temperature (middle row) and water saturation (bottom row) for a high-enthalpy realization of the Soultz-sous-Forêts geothermal field assuming a fracture network that consists of 15 fractures. Column wise, the simulation time increases from 300 *to* 500 *to* 1000 *[days].*

5. Discussion

The numerical model for the molar formulation is validated in this chapter. The results presented in chapter 4 are also discussed in this chapter on the basis of comparing the solutions and the performance between molar and natural variable formulations.

5.1. Numerical validation

In order to validate the numerical model using the molar formulation, the results of a low-enthalpy test case are compared with the Avdonin analytical solution (Faust and Mercer, 1979b). The test case consists of a one-dimensional reservoir with a length of $100\ [m]$ at initial pressure and temperature of $1 \times 10^7\ [Pa]$ and $165\ [^oC]$, respectively. Cold water is injected at a pressure of $1.2 \times 10^7\ [Pa]$ and a temperature of $71\ [^oC]$, whereas the production pressure is set at 0.9×10^7. Rock properties are set after the Middenmeer geothermal field.

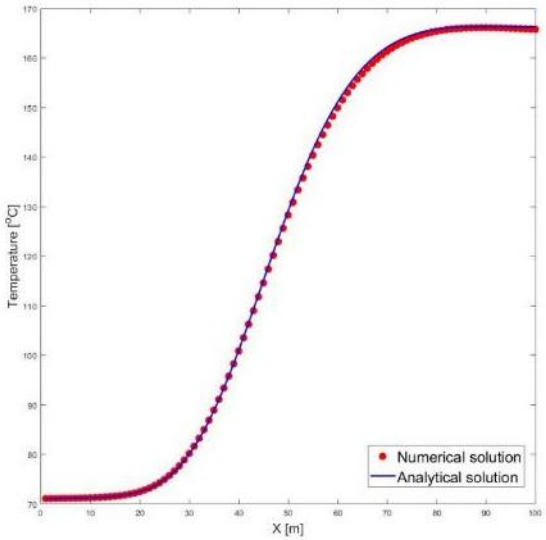

Figure 5.1: Numerical and analytical solutions to the described model problem effectively validating the numerical model using the molar variable formulation.

Figure 5.1 shows that there is a good match between the analytical solution and the numerical approximation, therefore validating the numerical model using the molar formulation.

5.2. Comparison of results

All test cases show similar results for the pressure, temperature and enthalpy solutions between the molar and natural variable formulations. The relative error (i.e. formulation error e_f) between both formulations ranges from 10^{-4} to 10^{-2} for all three solutions irrespective of the simulation approach (i.e. fine-scale or ADM).

The relative error for the pressure solution is smallest and fairly constant over time as pressure is defined as a primary variable in both formulations. The relative error that is present can be entirely attributed to the differences in the equations of state that are applied in each of the formulations. The relative error for the temperature solution tends to increase in the early stages of the simulation, after which it remains fairly constant for the remainder of the simulation time. The relative error for the enthalpy solution is largest in all test cases and decreases in the early stages of the simulation, after which it steadily increases during the remainder of the simulation. The relative errors for pressure,

temperature and enthalpy all exhibit the same general behavior over time, irrespective of the complexity of the model problem and the simulation approach. Note, however, that the relative error for the enthalpy solution in ADM simulations shows slightly more erratic behavior compared to the fine-scale simulations.

The larger (i.e. compared to pressure) relative error that is present in the temperature and enthalpy solutions can be attributed to the different primary variables that are defined in both formulations. In the molar formulation the enthalpy in the system is solved for and temperature is computed from the enthalpy solution. The natural formulation has the opposite approach. The equations of state applied in both formulations to compute temperature from enthalpy, and vice versa, are however not based on the same correlation. Figure 5.2 (top-left) shows that the correlation used in the molar formulation provides an accurate approximation of the reservoir temperature as the resulting temperature solution is equal to both the initial and boundary conditions (i.e. the temperatures in front of and behind the cold-water front). As the initial and boundary conditions are defined in terms of temperature, the correlations pertaining to both formulations are used to compute the initial reservoir enthalpy and injection enthalpy. Note that the correlation for enthalpy in the molar formulation is a re-written from of the correlation for temperature (see appendix A).

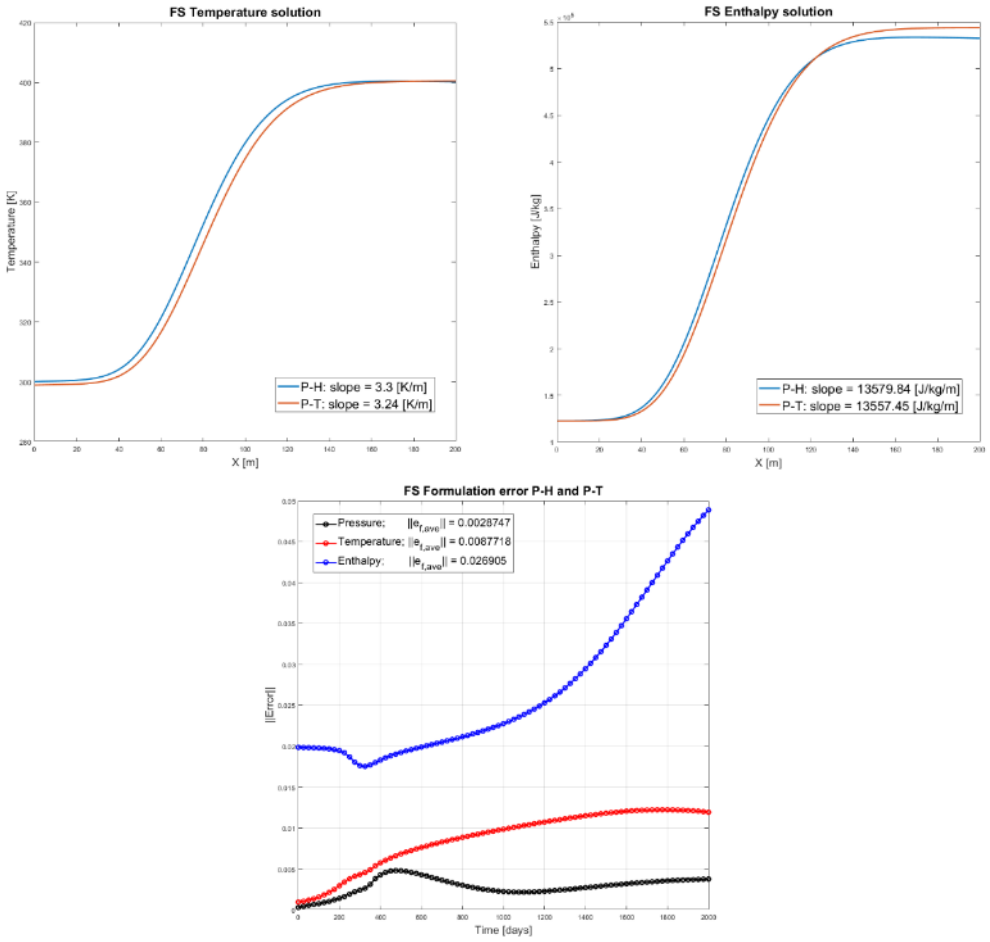

Figure 5.2: Comparison of cold-water front position between both formulations in terms of temperature (top-left) and enthalpy (top-right) for an arbitrary one-dimensional model problem. To illustrate further, the formulation error over time (bottom) is also presented. The formulation error e_f indicates the relative difference between the solutions obtained from both formulations.

The initial reservoir enthalpy shows a mismatch between both formulations, as illustrated in figure 5.2 (top-right). The correlation for enthalpy used in the natural formulation assumes the saturated internal energy and specific heat capacity of the fluid to be constant. This might prove to be an oversimplification causing the enthalpy to be structurally overestimated, as illustrated by the higher initial reservoir enthalpy and the position of the cold-water front. This mismatch causes the relative error for the enthalpy solution to be fundamentally larger than the relative temperature error. Furthermore, the mismatch in initial reservoir enthalpy becomes more significant when the cold-water front reaches the production well resulting in an increasing relative error over time. Note that the injection enthalpy is identical between both formulations. This is due to the application of a similar, yet re-written, correlation for the injection enthalpy and causes the relative error for enthalpy to decrease in the early stages of the simulation.

In regards to the position of the cold-water front, figure 5.2 shows a mismatch between both formulations in terms of the temperature solution, as well as the enthalpy solution. Results presented in chapter 4 show that this mismatch increases as the cold-water front propagates through the reservoir. This causes the relative error in both the temperature and enthalpy solutions to increase over time. Similar to the initial reservoir enthalpy, the amount of transported energy as described by the convection flux appears to be systematically overestimated in the natural formulation resulting in a different (i.e. overestimated) position of the cold-water front. Note that this also affects the temperature solution obtained from using the natural formulation. Using the molar formulation, the enthalpy in the convective flux term is treated as a primary variable resulting in a more accurate approximation of the amount of energy transported through the reservoir. Given the more accurate correlation for the temperature as a function of (pressure and) enthalpy, the approximation of the position of the cold-water front in the temperature solution obtained from the molar formulation can also be considered more accurate. Note that the same discretization strategy is applied in both formulations therefore minimizing the effect of numerical diffusion as a potential source of the mismatch in the position of the cold-water front between both formulations.

Changing the fluid models in such a way that the equations of state in both formulations are based on identical correlations may prove a viable option in reducing the relative temperature and enthalpy errors.

Although the behavior of the relative solution errors between both formulations is independent of the simulation approach, the relative error for the enthalpy solution shows more erratic behavior when the ADM simulation strategy is applied. As the grid selection criterion is given by a maximum temperature gradient, application of the fine-scale grid resolution is focused around the position of the cold-water front. The number of fine-scale grid cells applied in this region is determined at each time-step and generally affects the accuracy of the approximation of the position of the cold-water front. This results in slight variations of the relative enthalpy error over time. As the general mismatch in cold-water front positions between both formulations is also present in ADM simulations, the behavior of the relative enthalpy error is similar to that observed using the fine-scale simulation approach. Note that as the grid selection criterion is governed by temperature, combined with the more accurate correlation for temperature employed in the molar formulation, the relative temperature error shows less erratic behavior.

The error of the ADM method e_{ADM} is comparable between both formulations for the pressure, temperature and enthalpy solutions. The use of constant basis functions to approximate the temperature and enthalpy solutions increases their ADM error relative to that of the approximate

pressure solution (which uses multiscale basis functions). Furthermore, as the grid selection criterion is designed around a maximum temperature gradient, the ADM error of the enthalpy solution is larger than that of the temperature solution.

For both fine-scale and ADM simulation strategies, the difference in the solutions between both primary variable formulations can be considered negligible as it is largely dependent on the equations of state that are being used.

5.3. Comparison of performance

The simulations performance between both primary variable formulations shows the same behavior, independent of the simulation strategy. The required number of iterations for the non-linear system to converge starts low, and increases in the early stages of simulation. When cold-water is injected into the reservoir, the temperature at the location of the injection well decreases only due to conduction. It is when the reservoir temperature has decreased to the injection temperature that transport of the cold water through the reservoir starts taking place. The additional non-linearity introduced by the convective flux results in an increase in the required number of iterations. When the cold-water front propagates further from the injection well, the effect of the convective flux stabilizes and the number of iterations decreases again. Furthermore, the number of iterations also stabilizes at this point.

Considering a heterogeneous absolute permeability distribution greatly affects the transport of cold-water through the reservoir. This yields a variation in the contribution of the convective flux and therefore a more erratic behavior of the actual required number of iterations in the early stages of simulation. When a fracture network is added to the model complexity, the number of iterations required increases further as the contribution of the convective flux is dominant in the extended balance equations (i.e. in fractures). Similar to the heterogeneous absolute permeability, the different positions of the fractures relative to the position of the cold-water front further increase the erratic behavior of the actual number of iterations required.

The fine-scale simulation performance of both primary variable formulations is very similar for the model realizations of the Soultz-sous-Forêts geothermal field test case. As fractures are introduced to the model problem, the number of iterations required for the non-linear system to converge increases for both formulations. Contrary to the first two realizations, in which the number of iterations becomes constant at some point, the third realization shows a constant fluctuating number of iterations during the majority of the simulation for both formulations. This fluctuation is due to the changing magnitude of the timestep Δt in order to match the simulation time to the time at which the solution is written to file, and illustrates the sensitivity of the convergence to the size of the timestep for increasing model complexities.

The ADM simulation performance of both primary variable formulations shows similar behavior to the fine-scale simulation performance described above. Furthermore, the performance between the fine-scale and ADM simulation approaches is near identical, with the exception of the third realization of the Soultz-sous-Forêts geothermal field. Here, the ADM simulation strategy failed to find a solution based on the natural variable formulation. As the ADM strategy was able to effectively find a solution based on the molar formulation, the apparent issue regarding the natural formulation may be related to the increasing mismatch in reservoir enthalpy when using this formulation. The ADM results from the second realization of the Soultz-sous-Forêts field show no issues between the formulations in terms of capability of the ADM method to find a solution.

The fine-scale simulation performance of both primary variable formulations is again very similar for the model realizations of the Middenmeer geothermal field test case. Due to the heterogeneous permeability field, the required number of iterations to achieve convergence as well as the sensitivity to the size of the timestep is generally higher compared to the Soultz-sous-Forêts test case. However, the additional model complexity introduced by the presence of fractures does not result in an increase in the required number of iterations or in the sensitivity to the size of the timestep for fine-scale simulations. The ADM simulation performance is also similar between both primary variable formulations. Note that when a fracture network is introduced into the model problem, the natural formulation appears to perform slightly better as the number of iterations and number of chops is lower in these simulations.

A performance comparison between the fine-scale and ADM solution approaches can only be made for the first realization of the Middenmeer test case. The ADM strategy shows an increased number of iterations in the early stages of simulation compared to the fine-scale strategy. However, in the later stages the ADM strategy proves less susceptible to changes in the size of the time-step. This may be caused by the different grid resolution at which the solution is obtained. The ADM simulation strategy struggled to find a solution in the second and third (i.e. fractured) realizations of the Middenmeer test case based on the initial simulation parameters. This issue proved independent of the primary variable formulation used. By increasing the ADM threshold for the grid selection and decreasing the intrinsic permeability contrast, the ADM method showed no issues in finding a solution meaning that the added model complexities affect the performance of the ADM strategy. In addition, the performance is further affected by the fracture density as illustrated in figures 4.43 (bottom) and 4.51 (bottom).

The difference in performance between both formulations using a fine-scale simulation strategy is negligible. The performance itself is largely dependent on the complexity of the model problem. These results are similar to those presented by Wong, Horne and Voskov (2012), despite the added model complexities of a fracture network. Considering the ADM simulation strategy for the Middenmeer test case, the natural formulation tends to perform slightly better when the model complexity is increased.

5.4. High-enthalpy results

The results presented in the high-enthalpy test case of section 4.7 are indicative of a successful implementation of the molar formulation for multiphase flow and heat transfer simulations. In order to discuss the physical phenomena observed in multiphase simulations, the results from figure 4.52 are presented again in figure 5.3 highlighting the solution at 44 [days]. Three different regions can be defined in the pressure and enthalpy solutions presented in figure 5.3. The system, with initial conditions defined in the two-phase region, is still existing under these conditions in region C as illustrated by the enthalpy and saturation values.

The transition of the system into the single-phase compressed water region is marked by the boundary between regions C and B. First of all, the transition is indicated by a change in pressure gradient due to the different compressibilities between both phases. Secondly, as steam condenses into the liquid water phase, the enthalpy of the system decreases. This condensation also lowers the reservoir pressure. The latent heat of condensation yields an increase in both enthalpy and temperature when moving from region B to region A. Note that the water saturation in region B shows a minor amount of steam being present, and it is only in region A that the steam phase becomes fully absent.

Region A therefore represents the part of the reservoir in which the system has fully transitioned into the compressed water region, and therefore the cold-water front (dashed red line in figure 5.3) is observed in this region. As the system under two-phase conditions is represented by a single temperature, a temperature gradient is only observed at the location of the cold-water front. Naturally, a second enthalpy gradient is also observed at this location. Note that a slight change in pressure gradient can be observed at the position of the cold-water front due to the differences in the properties of liquid water at different temperatures.

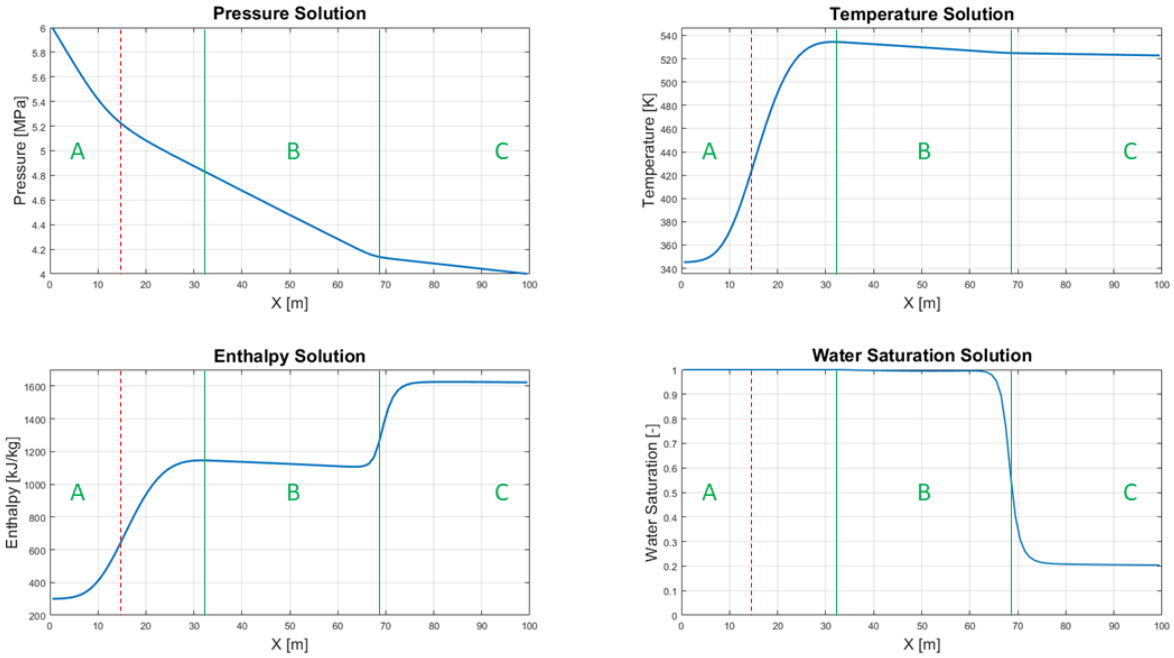

Figure 5.3: Numerical solution of high-enthalpy test case at the time of 44 [days]. Three regions are defined marking the different thermodynamic states of the system. Region A shows the system present in the compressed water region and region C shows the system under two-phase conditions. Region B marks the transition of the system from two-phase to single-phase conditions.

When applying an ADM threshold for the grid selection criterion based on a temperature gradient, only the cold-water front will be approximated at fine resolution. In order to capture the shock front between the liquid and steam phases, the ADM threshold needs to be defined based on an enthalpy gradient. This has been illustrated in the ADM results presented in section 4.7.

6. Conclusion

The aim of this study was to firstly compare the results and non-linear performance of the fine-scale and ADM simulation strategies between the molar and natural variable formulations for low-enthalpy fractured geothermal reservoirs, and secondly to extend the molar formulation to account for multiphase flow behavior. The molar formulation has been successfully implemented in the existing ADM simulation framework, and is able to account for multiphase flow conditions. Two test cases, modelled after existing low-enthalpy geothermal fields, are considered consisting of different (geological) realizations. Pressure, enthalpy and temperature solutions are compared between both primary variable formulations using both fine-scale and ADM simulation strategies. In addition, the performance of these simulation approaches is compared between both formulations.

Results show the relative difference in terms of pressure, temperature and enthalpy solutions between the molar and natural variable formulations to range between 10^{-4} and 10^{-2} independent of the simulation strategy. Comparison of fine-scale simulation performance shows negligible differences between both formulations. Added complexities to the model problem result in decreasing performance independent of the formulation used. Comparison of ADM simulation performance shows minor differences between both formulations for increasingly complex model problems.

In conclusion, any differences between the primary variable formulations can be considered negligible and their performance is largely dependent on the complexity of the model problem. Compared to the fine-scale simulation approach, the performance of the ADM simulation strategy is more affected by increasing model complexities.

7. Recommendations

In light of future work on simulating both low- and high-enthalpy fractured geothermal reservoirs, recommendations are given as to the direction in which this work may be continued and/or improved.

As both primary variable formulations are very similar in terms of results and performance for low-enthalpy geothermal reservoirs, the comparison can (and should) be extended to the simulation of high-enthalpy reservoirs in which multiphase flow conditions prevail. The added complexity of a fracture network should again be considered, and it would be interesting to see what effect fractures have on phase changes and how natural convection in the reservoir is affected by their presence.

As performance is largely dependent on the model complexity, the comparison study can be further improved by considering a three-dimensional model (including fractures) and anisotropy in matrix properties. Additionally, the initial temperature and/or enthalpy distributions can be considered as non-uniform. This becomes especially important when extending the model to three dimensions. Furthermore, when extending the model to three dimensions, the occurrence of natural convection should be taken into account by including the effects of gravity in the simulations. Natural convection cannot be neglected in (multiphase) simulations of high-enthalpy reservoirs. A new approach in the treatment of the gravity term is proposed by Croucher et al. (2020) and aims at reducing the convergence issues related to the non-linearity introduced by the gravity term.

As mentioned in the discussion presented in this work, the relative temperature and enthalpy errors between both formulations may be reduced by the implementation of a fluid model (i.e. set of equations of state) that is consistent for both formulations. To this end, the use of CoolProp (Bell et al., 2014) may provide a consistent approach in the thermodynamic description of fluid phase properties. An additional benefit of the implementation of CoolProp (Bell et al., 2014) is the significant extension in the range of validity of the fluid model, i.e. pressure and temperature values up to $1000\ [bar]$ and $2273.15\ [K]$, respectively.

In regards to the high-enthalpy test case considered in this work, it has been presented in order to illustrate the successful implementation of a multiphase formulation only. In terms of performance of these two-phase simulations, there is a lot of room for improvement. The most significant performance improvement is presented by Wong et al. (2016) and consists of a phase-change algorithm in which the enthalpy value is chopped at the phase boundaries in order to prevent oscillations around these boundaries. This algorithm proves especially fruitful when transitioning into the two-phase region. A secondary improvement may be found in the computation of the fluid phase properties in the two-phase region; inverse methods can be used to iteratively compute the values of density and saturation from the mixture enthalpy as described in equation 2.26 in this work. Such an iterative approach can also be used to compute the temperature in the two-phase region, and to estimate the Jacobian derivatives in the two-phase region.

Bibliography

Axelsson, G., Stefánsson, V., & Xu, V. (2002). Sustainable management of geothermal resources. *Proceedings, 2002 Beijing International Geothermal Symposium*.

Aziz, K., & Settari, A. (2002). *Petroleum reservoir simulation*. Calgary: K. Aziz & A. Settari.

Bell, I. H., Wronski, J., Quoilin, S., & Lemort, V. (2014). Pure and Pseudo-pure Fluid Thermophysical Property Evaluation and the Open-Source Thermophysical Property Library CoolProp. *Industrial & Engineering Chemistry Research, 53*(6), 2498–2508. doi: 10.1021/ie4033999

Berkowitz, B. (2002). Characterizing flow and transport in fractured geological media: A review. *Advances in Water Resources, 25*(8-12), 861-884. doi:10.1016/s0309-1708(02)00042-8

Burnell, J., Clearwater, E., Croucher, A., Kissling, W., O'Sullivan, J., O'Sullivan, M., & Yeh, A. (2012). Future directions in geothermal modelling. *Proceedings, 34th New Zealand Geothermal Workshop 2013,* 19-21.

Coats, K. H. (1977). Geothermal reservoir modelling. *SPE Annual Fall Technical Conference and Exhibition.*

Coats, K. H. (1980). An equation of state compositional model. *Society of Petroleum Engineers Journal, 20*, 363-376.

Croucher, A., O'Sullivan, M., O'Sullivan, J., Yeh, A., Burnell, J., & Kissling, W. (2020). Waiwera: A parallel open-source geothermal flow simulator. *Computers & Geosciences, 141*, 104529. doi:10.1016/j.cageo.2020.104529

Cusini, M., Kruijsdijk, C. V., & Hajibeygi, H. (2016). Algebraic dynamic multilevel (ADM) method for fully implicit simulations of multiphase flow in porous media. *Journal of Computational Physics, 314*, 60-79. doi:10.1016/j.jcp.2016.03.007

Dickson, M. H., & Fanelli, M. (2003). *Geothermal energy: utilization and technology*. Paris, FR: United Nations Educational, Scientific and Cultural Organization (UNESCO).

Faust, C. R., & Mercer, J. W. (1977). Finite-difference model of two-dimensional, single, and two-phase heat transport in a porous medium - Version I. *Open-File Report*. doi:10.3133/ofr77234

Faust, C. R., & Mercer, J. W. (1979a). Geothermal reservoir simulation: 1. Mathematical models for liquid- and vapor-dominated hydrothermal systems. *Water Resources Research, 15*(1), 23-30. doi:10.1029/wr015i001p00023

Faust, C. R., & Mercer, J. W. (1979b). Geothermal reservoir simulation: 2. Numerical solution techniques for liquid- and vapor-dominated hydrothermal systems. *Water Resources Research, 15*(1), 31-46. doi:10.1029/wr015i001p00031

Fletcher, P. (1993). *Chemical thermodynamics for earth scientists*. Harlow: Longman Scientific & Technical.

Hajibeygi, H., Karvounis, D., & Jenny, P. (2011). A hierarchical fracture model for the iterative multiscale finite volume method. *Journal of Computational Physics, 230*(24), 8729-8743. doi:10.1016/j.jcp.2011.08.021

Hosseinimehr, M., Kobaisi, M. A., Vuik, C., & Hajibeygi, H. (2019a). Dynamic Multilevel Multiscale Simulation of Naturally Fractured Reservoirs with Generic Fracture-Matrix Conductivity Contrasts. *SPE Reservoir Characterisation and Simulation Conference and Exhibition*. doi:10.2118/196626-ms

Hosseinimehr, M., Arbarim, R., Cusini, M., Vuik, C., & Hajibeygi, H. (2019b). Algebraic Dynamic Multilevel Method for Fractured Geothermal Reservoir Simulation. *SPE Reservoir Simulation Conference*. doi:10.2118/193894-ms

Hosseinimehr, M., Vuik, C., & Hajibeygi, H. (2020). Adaptive dynamic multilevel simulation of fractured geothermal reservoirs. *Journal of Computational Physics: X, 7*, 100061. doi:10.1016/j.jcpx.2020.100061

Ingebritsen, S. E., Sanford, W. E., & Neuzil, C. E. (2006). *Groundwater in geologic processes*. New York: Cambridge Univ. Press.

Lee, S. H., Wolfsteiner, C., & Tchelepi, H. A. (2008). Multiscale finite-volume formulation for multiphase flow in porous media: Black oil formulation of compressible, three-phase flow with gravity. *Computational Geosciences, 12*(3), 351-366. doi:10.1007/s10596-007-9069-3

Marelis, A. A. (2017). *Energy capacity of a geothermal reservoir* (Unpublished bachelor's thesis). Delft University of Technology.

McClure, M. W., & Horne, R. N. (2014). An investigation of stimulation mechanisms in Enhanced Geothermal Systems. *International Journal of Rock Mechanics and Mining Sciences, 72*, 242-260. doi:10.1016/j.ijrmms.2014.07.011

Moukalled, F., Mangani, L., & Darwish, M. (2016). *The finite volume method in computational fluid dynamics: An advanced introduction with OpenFOAM and Matlab*. Cham: Springer.

Nield, D. A., & Bejan, A. (2006). *Convection in porous media*. New York: Springer.

O'Sullivan, M.J., Pruess, K., & Lippmann, M.J. (2001). State of the art of geothermal reservoir simulation. *Geothermics, 30*, 395-429.

O'Sullivan, J., Croucher, A., Yeh, A., & O'Sullivan, M. (2013). Improved Convergence for Air-Water and CO2-Water TOUGH2 Simulations. *Proceedings, 35th New Zealand Geothermal Workshop 2013*.

Praditia, T., Helmig, R., & Hajibeygi, H. (2018). Multiscale formulation for coupled flow-heat equations arising from single-phase flow in fractured geothermal reservoirs. *Computational Geosciences, 22*(5), 1305-1322. doi:10.1007/s10596-018-9754-4

Pruess, K., Oldenburg, C., & Moridis, G. (1999). TOUGH2 Users Guide Version 2. doi:10.2172/751729

Toth, A., & Bobok, E. (2017). *Flow and heat transfer in geothermal systems: Basic equations for description and modeling geothermal phenomena and technologies*. Amsterdam: Elsevier.

Wang, Y., Hajibeygi, H., & Tchelepi, H.A. (2014). Algebraic multiscale solver for flow in heterogeneous porous media. *Journal of Computational Physics, 259* (14), 284-303.

Watanabe, N., Kikuchi, T., Ishibashi, T., & Tsuchiya, N. (2017). v-X-type relative permeability curves for steam-water two-phase flows in fractured geothermal reservoirs. *Geothermics, 65*, 269-279. doi:10.1016/j.geothermics.2016.10.005

Wong, Z. Y., Horne, R., & Voskov, D. (2015). A Geothermal Reservoir Simulator with AD-GPRS. *Proceedings, World Geothermal Congress 2015*.

Wong, Z. Y., Horne, R., & Voskov, D. (2016). Comparison of Nonlinear Formulations for Geothermal Reservoir Simulations. *Proceedings, 41st Workshop on Geothermal Reservoir Engineering*.

Wong, Z. Y., Rin, R., Tchelepi, H., & Horne, R. (2017). Comparison of a Fully Implicit and Sequential Implicit Formulation for Geothermal Reservoir Simulations. *Proceedings, 42nd Workshop on Geothermal Reservoir Engineering*.

Wong, Z. Y., Horne, R., & Voskov, D. (2018). Sequential implicit nonlinear solver for geothermal simulation. *Journal of Computational Physics, 368*, 236-253. doi:https://doi.org/10.1016/j.jcp.2018.04.043

Zaydullin, R., Voskov, D. V., James, S. C., Henley, H., & Lucia, A. (2014). Fully compositional and thermal reservoir simulation. *Computers & Chemical Engineering, 63*, 51-65. doi:10.1016/j.compchemeng.2013.12.008

Ţene, M., Wang, Y., & Hajibeygi, H. (2015). Adaptive algebraic multiscale solver for compressible flow in heterogeneous porous media. *Journal of Computational Physics, 300*, 679-694. doi:10.1016/j.jcp.2015.08.009

Ţene, M., Bosma, S. B., Kobaisi, M. S., & Hajibeygi, H. (2017). Projection-based Embedded Discrete Fracture Model (pEDFM). *Advances in Water Resources, 105*, 205-216. doi:10.1016/j.advwatres.2017.05.009

Appendix A

The simplified fluid models for both the natural and molar formulations are presented here. The natural formulation employs correlations developed by Coats (1977) and the molar formulation employs correlations developed by Faust and Mercer (1977). All variables are presented in SI units.

Both formulations apply the same correlations for the porosity ϕ and rock internal energy U_r. These correlations are given by

$$\phi(P) = \phi_0 \times \exp\big(c_r(P - P_0)\big) \tag{A.1}$$

in which c_r, ϕ_0 and P_0 are the rock compressibility, initial reservoir porosity and initial reservoir pressure, respectively, and

$$U_r(T) = C_p \times T \tag{A.2}$$

where C_p is the rock specific heat capacity. Note that $U_r = H_r$ is assumed as described in chapter 2 section 3.

A.1. Natural formulation

The density of the liquid phase in $[kg/m^3]$ is treated as a function of pressure and temperature and is given by

$$\rho_l(P,T) = \rho_{l,s}(T)\big[1 + c_f(T)(P - P_{sat})\big] \tag{A.3}$$

where the saturation pressure P_{sat} has a constant value of 10^5 $[Pa]$, and the density of the liquid phase at saturation conditions $\rho_{l,s}$ and fluid compressibility c_f are obtained from empirical correlations

$$\rho_{l,s}(T) = \begin{cases} -0.0032T^2 + 1.7508T + 757.5, & for\ T \leq 623.15\ [K] \\ -0.5214T^2 + 652.73T - 203714, & for\ T \geq 623.15\ [K] \end{cases} \tag{A.4}$$

$$c_f(T) = (0.0839T^2 + 652.73T - 203714) \times 10^{-12}, \qquad for\ 273\ [K] < T < 647\ [K] \tag{A.5}$$

The liquid phase enthalpy in $[J/kg]$ is treated as a function of pressure and temperature and is given by

$$h_l(P,T) = U_{l,s} + C_{p,l}(T - T_{sat}) + \frac{P}{\rho_l} \tag{A.6}$$

where the saturation temperature T_{sat} has a constant value of 373 $[K]$, the specific heat capacity of the liquid phase $C_{p,l}$ has a constant value of 4200 $\left[\frac{J}{kg.K}\right]$ and the liquid phase internal energy at saturation conditions $U_{l,s}$ has a constant value of 420000 $\left[\frac{J}{kg}\right]$.

The viscosity of the liquid phase in $[Pa.s]$ is treated as a function of temperature and is given by

$$\mu_l(T) = 2.414 \times 10^{-5} \times 10^{\left(\frac{247.8}{T-140}\right)} \tag{A.7}$$

A.2. Molar formulation

The correlations used to express the dependent variables in terms of pressure and enthalpy (i.e. molar formulation) are limited to the following range of validity

$$P: 1\ -175\ [bar], H: 209-3175\ \left[\frac{kJ}{kg}\right] and\ T: 274.15-573.15\ [K] \tag{A.8}$$

The pressure and enthalpy as input to the following correlations are in $10^{-6}[bar]$ and $10^{-7}[kJ/kg]$, respectively.

The liquid and vapor phase densities in $[kg/m^3]$ are treated as functions of pressure and enthalpy and are given by

$$\rho_l(P,H) = (1.00207 + 4.42607\times10^{-11}P - 5.47456\times10^{-12}H + 5.02875\times10^{-21}HP - 1.24791\times10^{-21}H^2)\times10^3 \tag{A.9}$$

$$\rho_v(P,H) = (-2.26162\times10^{-5} + 4.38441\times10^{-9}P - 1.79088\times10^{-19}PH + 3.69276\times10^{-36}P^4 + 5.17644\times10^{-41}PH^3)\times10^3 \tag{A.10}$$

The saturated liquid and vapor phase enthalpies in $[J/kg]$ are treated as functions of pressure and are given by

$$h_l(P) = (7.30984\times10^9 + 1.29239\times10^2P - 1.00333\times10^{-6}P^2 + 3.9881\times10^{-15}P^3 - 9.90697\times10^{15}P^{-1} + 1.29267\times10^{22}P^{-2} - 6.28359\times10^{27}P^{-3})\times10^{-7} \tag{A.11}$$

$$h_v(P) = (2.82282\times10^{10} - 3.91952\times10^5P^{-1} + 2.54342\times10^{21}P^{-2} - 9.38879\times10^{-8}P^2)\times10^{-7} \tag{A.12}$$

Temperature in $[K]$ is treated as a function of pressure and enthalpy in the single-phase regions. The temperature in the compressed water region is given by

$$T(P,H) = 273.15 - 2.41231 + 2.5622\times10^{-8}H - 9.31415\times10^{-17}P^2 - 2.2568\times10^{-19}H^2 \tag{A.13}$$

and in the superheated steam region by

$$T(P,H) = 273.15 - 374.669 + 4.79921\times10^{-6}P - 6.33606\times10^{-15}P^2 + 7.39386\times10^{-19}H^2 - 3.3372\times10^{34}H^{-2}P^{-2} + 3.57154\times10^{19}P^{-3} - 1.1725\times10^{-37}H^3P - 2.26861\times10^{43}H^{-4} \tag{A.14}$$

Note that in the two-phase region, the saturated liquid phase enthalpy is used in equation .. instead.

The liquid and vapor phase viscosities in $[Pa.s]$ are treated as functions of temperature and are given by

$$\mu_l(T) = \left(241.4\times10^{\left(\frac{247.8}{(T-273.15)+133.15}\right)}\right)\times10^{-4} \tag{A.15}$$

$$\mu_v(T) = (0.407(T-273.15)+80.4)\times10^{-4} \tag{A.16}$$

In order to set the initial and injection properties identically between both formulations, enthalpy is computed from temperature using

$$h_l(P,T) = \frac{-B + \sqrt{B^2 - 4D\big(A + CP^2 - (T - 273.15)\big)}}{2D} \tag{A.17}$$

where the constants $A = -2.41231$, $B = 2.5622 \times 10^{-8}$, $C = -9.31415 \times 10^{-17}$ and $D = -2.2568 \times 10^{-19}$. Note that this equation is only valid in the compressed water region, and therefore it is assumed that only the liquid phase is present in the injection well.

The water saturation is computed using equation 2.23 presented in chapter 2. This equation yields the pressure-enthalpy phase diagram as illustrated in figure A.1.

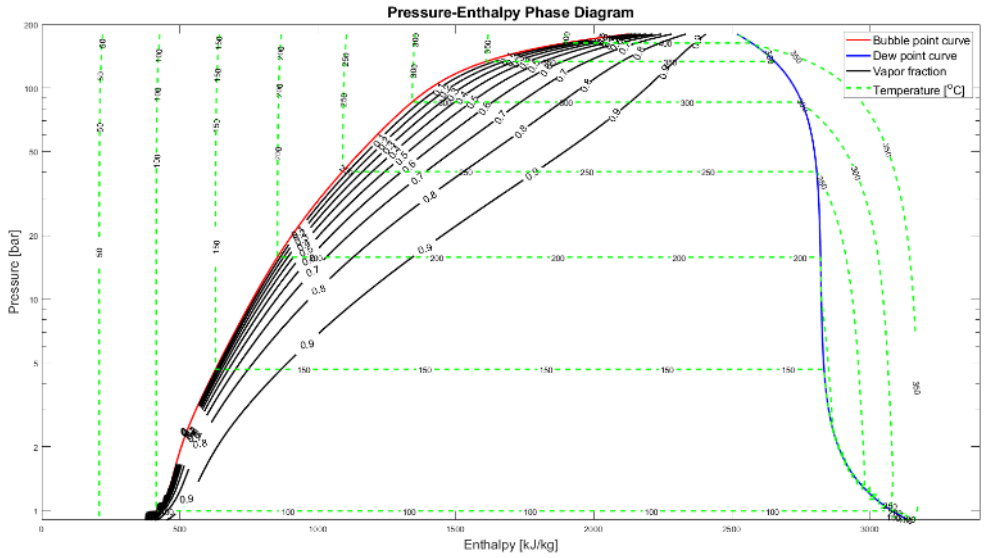

Figure A.1: Pressure-Enthalpy phase diagram. Contour lines of temperature are included in the diagram.

There exists considerable uncertainty regarding a proper correlation for the relative permeability of the two phases in geothermal systems. Watanabe et al. (2017) apply the Corey functions for relative permeability, whereas Faust and Mercer (1977) propose a variation on the Corey functions in which vaporization dominates condensation (a drainage displacement process). Verma functions are also often applied for porous rocks. They are especially applicable to water-steam two-phase flows as they are derived based on the enhancement of steam relative permeability due to phase transformation (Watanabe et al., 2017). Nield and Bejan (2006) state that "experience has shown that the main qualitative features of convection flows are not sensitive to the precise form of the relative permeability versus saturation relationship" and therefore suggest the application of a linear relationship. In an effort not to increase the non-linearity presented by the fluid model any further, a linear relation for the relative permeability is chosen at this point such that

$$k_{r,\alpha}(S_\alpha) = S_\alpha \tag{A.18}$$

for a given phase α.

Appendix B

The full derivation of the mass and energy conservation equations is presented in this appendix.

B.1. Description of conservation laws

Moukalled, Mangani and Darwish (2016) define the principle of conservation as certain physical measurable quantities being conserved over a local region in an isolated system. Conservation laws govern a variety of physical quantities such as mass, momentum and energy. A conservation law is an axiom and can thus be expressed by a mathematical relation. When fluid flow and related transfer phenomena are involved, either a Lagrangian (material volume, MV) or an Eulerian (control volume) approach can be taken to formulate the conservation laws.

The Lagrangian approach subdivides the fluid into fluid parcels, each of which is able to move through both space and time, and the flow path can be described by a function $x(t, x_0)$ where x_0 is the position of the parcels center of mass. The material volume and the shape of its bounding surface may vary in time representing successive configurations of the same fluid particles of fixed identity.

The Eulerian approach yields a description of changes in the properties of a moving fluid by focusing on a fixed point in the flow region while the fluid is passing it, and as time passes. This means that the flow velocity is a function of both space and time, i.e. $u(t, x)$. The configuration of the fluid particles is fixed in time, i.e. the control volume, its bounding surface and the number of fluid particles present in the control volume are fixed in time, but the configuration does not have to consist of the same (fixed identity) fluid particles at any given time.

The two description approaches are related by

$$v\big(t, x(t, x_0)\big) = \frac{\partial}{\partial t} x(t, x_0) \tag{B.1}$$

as the derivative of the position of a fluid parcel x_0 with respect to time equals its velocity (Moukalled et al., 2016).

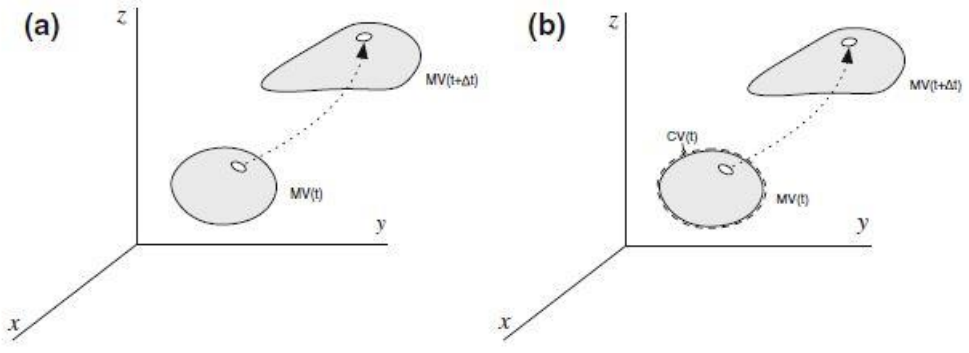

Figure 1: Lagrangian (a) and Eulerian (b) description of fluid flow. From Moukalled et al., 2016.

In this work, the Eulerian formulation is used to describe the conservation laws, i.e. a (fixed) control volume is considered. This formulation allows for a field (or system) scale approach as it abandons the necessity of simulating individual particle paths. An Eulerian approach enables control over the domain of interest, i.e. the region of interest can be defined and fixed in space, which is very useful as the fluid

flow problems considered in this work require the computation of fluid properties in a fixed region. It should also be mentioned that the presence of an advective rate of change term (or flux) in the conservation equations presented in this work is a direct result of the use of an Eulerian approach, and yields a (strong) non-linear behavior of the conservation equations.

B.2. Conservation of mass

Toth and Bobok (2017) define the principle of conservation of mass as the mass of a body being constant (or conserved) during its motion, i.e. the rate of change with time of the mass of a body is equal to zero (absence of source and/or sink). As the shape of the material volume may vary in time, the mass of the volume can be expressed as a volume integral of the density over the volume. The principle of conservation of mass can be mathematically expressed as the material derivative of this volume integral (Toth and Bobok, 2017)

$$\frac{d}{dt}\int_{V(t)} \rho \, dV = 0 \tag{B.2}$$

The definition of the conservation principle presented above applies to a moving material volume of fluid, and not to a fixed point or control volume. In order to express the conservation laws using a Eulerian formulation, Reynolds transport theorem must be applied to find the Eulerian equivalent of an integral taken over a moving material volume of fluid (Moukalled et al., 2016). This yields

$$\frac{d}{dt}\int_{V(t)} \rho \, dV + \int_{S(t)} \rho u \cdot n \, dS = 0 \tag{B.3}$$

The Leibniz integral rule can be applied in order to differentiate a volume integral of which the limits are dependent on the differential variable (Moukalled et al., 2016). Considering a fixed control volume, the geometry is independent of time and application of the Leibniz integral rule simply yields the interchange of the integral and partial differential operators. This allows writing equation B.3 as

$$\int_{V} \frac{\partial}{\partial t} \rho \, dV + \int_{S} \rho u \cdot n \, dS = 0 \tag{B.4}$$

which illustrates the principle of conservation of mass as described by an Eulerian formulation. It states that the sum of the local rate of change of mass (accumulation) and the convective rate of change of mass (mass flux ρu across the bounding surface, i.e. net outgoing flux) is equal to zero in the absence of a source and/or sink (Moukalled et al., 2016; Toth and Bobok, 2017). This means equation B.4 may also be formulated as

$$accumulation - net\ outgoing\ flux = source\ term \tag{B.5}$$

where the $source\ term$ is equal to zero as source and/or sink are assumed absent in order to illustrate the mass conservation principle. The mass conservation equation can thus also be obtained by analyzing the properties of the flow into and out of an infinitesimal control volume.

The surface integral of the mass flux across the bounding surface (equation B.4) can be transformed into a volume integral by application of the divergence theorem. The divergence theorem states that, in order for mass to be conserved, the sum of all sources (and sinks) of mass inside the control volume is equal to the rate at which mass leaves the control volume, i.e. the net outgoing flux (Moukalled et al., 2016). The sum of all sources and sinks of mass is defined as a volume integral of the divergence of the mass flux over the region inside the bounding surface.

Application of this theorem yields

$$\int_V \frac{\partial}{\partial t}\,\rho\,dV + \int_V \nabla\cdot(\rho u)\,dV = 0 \tag{B.6}$$

which, by combining the volume integrals, can be rewritten as

$$\int_V \left[\frac{\partial \rho}{\partial t} + \nabla\cdot(\rho u)\right] dV = 0 \tag{B.7}$$

The integral of equation B.7 must be equal to zero for it to hold for any control volume. This results in the differential form of the law of conservation of mass, i.e. the mass conservation or continuity equation (Moukalled et al., 2016; Toth and Bobok, 2017)

$$\frac{\partial \rho}{\partial t} + \nabla\cdot(\rho u) = 0 \tag{B.8}$$

In order for the mass conservation equation to account for both single- and two-phase flow the total mass within a control volume at any given time is the sum of the mass fraction in the liquid phase and the mass fraction in the vapor phase. The volume occupied by fluids and/or gases in the control volume is given by the porosity ϕ in the case the control volume describes a porous medium. This means the mass conservation equation may be written as

$$\frac{\partial}{\partial t}(\phi\rho_w S_w + \phi\rho_s S_s) + \nabla\cdot(\rho_w u_w + \rho_s u_s) = 0 \tag{B.9}$$

where the saturation $S_{w,s}$ is representative of the volume fraction of either the liquid water phase w or the vapor steam phase s. By describing a single component fluid present as either of the two phases, or both, mass transfer between phases is assumed absent and the accumulation and flux terms in equation B.9 can be described by the sum of the phases. When mass transfer is taken into account, separate mass conservation equations have to be written for the individual phases. Such equations often include a diffusive mass flux term and are linked through a source term representing vaporization and condensation phenomena (Faust and Mercer, 1979a).

Assuming the fluid phase velocity is governed by Darcy's law for multiphase flow, i.e. a simplified momentum conservation equation assuming negligible inertia and viscous effects, equation B.9 can be written as

$$\begin{aligned}\frac{\partial}{\partial t}(\phi\rho_w S_w + \phi\rho_s S_s) - \nabla\cdot\left(\rho_w \frac{K k_{r,w}}{\mu_w}\cdot(\nabla P_w - \rho_w g z)\right) \\ -\nabla\cdot\left(\rho_s \frac{K k_{r,s}}{\mu_s}\cdot(\nabla P_s - \rho_s g z)\right) = 0\end{aligned} \tag{B.10}$$

where the phase pressures $P_{w,s}$ are related through the capillary pressure $P_c = P_s - P_w$. The surface tension between liquid and vapor phases is a function of temperature, i.e. it decreases with increasing temperature until it becomes fully absent at the critical point (Ingebritsen et al., 2006).

The effect of gravitational forces is included in Darcy's law to account for the occurrence of natural convection as a result of phase change. Due to the high density difference between the water and steam phases, buoyancy forces play a major role in the transport of heat within the reservoir. The

effect of density driven flow is an essential part of the convective flux and can be categorized as natural convection (Ingebritsen et al., 2006).

Under the assumption of equilibrium boiling conditions, capillary effects may be considered negligible resulting in $P_w = P_s$, and we can write equation B.10 as

$$\frac{\partial}{\partial t}\left(\phi \sum_{\alpha=1}^{n_p} \rho_\alpha S_\alpha\right) - \nabla \cdot \left(\sum_{\alpha=1}^{n_p}\left(\rho_\alpha \frac{K k_{r,\alpha}}{\mu_\alpha} \cdot (\nabla P - \rho_\alpha g z)\right)\right) = 0 \tag{2.11}$$

where the subscript α denotes the liquid or vapor phase, and the number of phases n_p is two.

Although equation B.11 is derived for a single control volume, it does also apply to a series of control volumes describing the full geothermal reservoir. Under production stresses, mass may be added to and/or extracted from the system through injection and production wells, respectively. These mass fluxes are defined for both phases, the sum of which is captured as a source or sink term in the mass conservation equation. This yields the mass conservation equation of the model problem

$$\frac{\partial}{\partial t}\left(\phi \sum_{\alpha=1}^{n_p} \rho_\alpha S_\alpha\right) - \nabla \cdot \left(\sum_{\alpha=1}^{n_p}\left(\rho_\alpha \frac{K k_{r,\alpha}}{\mu_\alpha} \cdot (\nabla P - \rho_\alpha g z)\right)\right) = \sum_{\alpha=1}^{n_p} \rho_\alpha q_\alpha \tag{2.12}$$

By defining the fluid phase mobility $\lambda_\alpha = \frac{K k_{r,\alpha}}{\mu_\alpha}$, and by defining total fluid properties to capture the summation operators for the different phases, equation B.12 can be simplified to

$$\frac{\partial}{\partial t}(\phi \rho_t) - \nabla \cdot ((\rho\lambda)_t \nabla P - (\rho^2\lambda)_t g \nabla z) = (\rho q)_t \tag{B.13}$$

where the total (fluid) density $\rho_t = \rho_w S_w + \rho_s S_s$, the total convective mass flux $(\rho\lambda)_t = \rho_w \lambda_w + \rho_s \lambda_s$, the gravity term $(\rho^2\lambda)_t = \rho_w^2 \lambda_w + \rho_s^2 \lambda_s$ and the source term $(\rho q)_t = \rho_w q_w + \rho_s q_s$.

B.3. Conservation of energy

Moukalled, Mangani and Darwish (2016) define the principle of conservation of energy as the sum of all forms of energy (mechanical, kinetic, chemical, etc.) being constant in an isolated system, and the energy is conserved over time. This principle 'is governed by the first law of thermodynamics which states that energy can be neither created nor destroyed during a process; it can only change from one form into another' (Moukalled et al., 2016).

The first law of thermodynamics applied to the material volume states that the rate of change of the total energy e of the material volume is equal to the rate of heat addition Q to the volume and the rate of work done W on the volume. This can be mathematically expressed as

$$\frac{d}{dt}\int_{V(t)} \rho e \, dV = Q + W \tag{B.14}$$

where the total energy e is defined as $U + \frac{1}{2}u \cdot u$, i.e. the sum of the specific internal energy U (internal energy per unit mass) and kinetic energy per unit mass of the material volume. The sign convention ensures that both the heat added to and the work done on the material volume are positive. Note that when conservative forces are considered, the work done W on the volume corresponds to a change in the potential energy related to these forces.

The net rate of heat addition Q consists of two components; the rate of heat transfer across the boundaries of the material volume Q_S and the rate of heat generation and/or destruction within the material volume Q_V. The net rate of work done W consists of the rate of work done by surface forces W_S and body forces W_B acting on the material volume. This means the first law of thermodynamics in equation B.14 can be written as

$$\frac{d}{dt}\int_{V(t)} \rho e \, dV = Q_V + Q_S + W_B + W_S \tag{B.15}$$

Application of Reynolds transport theorem to the material derivative of equation B.15 yields its Eulerian equivalent. Subsequent differentiation of the volume integral using Leibniz integral rule, assuming a fixed control volume, allows writing equation B.15 by means of an Eulerian formulation. This yields

$$\int_V \frac{\partial}{\partial t} \rho e \, dV + \int_S \rho e u \cdot n \, dS = Q_V + Q_S + W_B + W_S \tag{B.16}$$

in which the principle of conservation of energy is illustrated as the sum of the local rate of change of energy (accumulation) and the convective rate of change of energy (net outgoing flux) being equal to the rate of heat addition and the rate of work done (source and/or sink terms).

A force that acts on the entire control volume is considered a body force. An example of such a force is given by gravity. The rate of work done by a body force f_b can, by definition, be expressed as the product of a force and a velocity. The rate of work done by body forces W_B can thus be written as

$$W_B = \int_V f_b \cdot u \, dV \tag{B.17}$$

Considering an arbitrary control volume, two types of forces acting upon its surface can be distinguished; a normal force and a shear or deviatoric force. These forces can be expressed in terms of the total stress tensor Σ and an orientation n such that $\Sigma \cdot n$ represents the surface force acting on the boundary dS of the control volume. Substituting this expression for the surface force f_S and subsequent application of the divergence theorem allows the rate of work done by surface forces W_S to be written as

$$\begin{aligned} W_S &= \int_S f_S \cdot u \, dS = \int_S (\Sigma \cdot u) \cdot n \, dS = \int_V \nabla \cdot (\Sigma \cdot u) \, dV = \\ &= \int_V \nabla \cdot [(-P\mathrm{I} + \tau) \cdot u] \, dV = \int_V [-\nabla \cdot (Pu) + \nabla \cdot (\tau \cdot u)] \, dV \end{aligned} \tag{B.18}$$

where the stress tensor Σ has been rewritten in terms of two separate components. The first component is the $-\nabla \cdot (Pu)$-term (where P is a constant pressure) originating from the main diagonal elements of the stress tensor. This component is representative of the normal forces either acting upon the control volume as a result of an external pressure, or exerted by the control volume as a result of an internal pressure, or both. This term directly relates to the compressibility of the system; an external pressure affects the compressibility of the rock matrix, whereas changes in internal pressure relate to the compressibility of the fluid. Written here with a minus sign it is illustrative of an external pressure affecting the control volume.

The second component is the $\nabla \cdot (\tau \cdot u)$-term (where τ is the shear force) originating from the off diagonal elements of the stress tensor and is representative of the shear or deviatoric forces acting upon the control volume. Such forces may also occur within the control volume due to viscous effects. Under the assumption that the control volume is not subject to angular deformation in any direction and viscous shearing effects are negligible, the contribution of the shear force to the work done by surface forces can be neglected. In addition, normal forces are (often) much greater than shear forces resulting in a minimal contribution of the $\nabla \cdot (\tau \cdot u)$-term when angular deformation and viscous effects are considered (Moukalled et al., 2016; Toth and Bobok, 2017).

The rate of heat generation and/or destruction within the control volume can be considered as a heat source or sink q_V, and can thus be formulated as (where q_V is heat transfer at constant volume)

$$Q_V = \int_V q_V \, dV \tag{B.19}$$

The rate of heat transfer Q_S to the control volume can be considered as a heat flux q_S across the boundaries of the control volume, and, through application of the divergence theorem, can be written as

$$Q_S = -\int_S q_S \cdot n \, dS = -\int_V \nabla \cdot q_S \, dV \tag{B.20}$$

where n is the outward pointing normal to the boundaries of the volume. This heat flux describes a conductive rate of change of heat rather than a convective rate of change.

Substitution of the rate of work and heat transfer terms by their equivalent expressions into equation B.16, and subsequent application of the divergence theorem yields

$$\begin{aligned} &\int_V \left[\frac{\partial}{\partial t}(\rho e) + \nabla \cdot (\rho e u)\right] dV = \\ &= -\int_V \nabla \cdot q_S \, dV + \int_V -\nabla \cdot (Pu) \, dV + \int_V f_b \cdot u \, dV + \int_V q_V \, dV \end{aligned} \tag{B.21}$$

Equation B.21 can be rewritten such that the sum of the integrals is equal to zero (the source term can be assumed zero) and the equation holds for any control volume. This results in the differential form of the law of conservation of (specific) total energy, or simply energy equation

$$\frac{\partial(\rho e)}{\partial t} + \nabla \cdot (\rho e u) = -\nabla \cdot q_S - \nabla \cdot (Pu) + f_b \cdot u + q_V \tag{B.22}$$

The energy equation may be written in terms of specific internal energy, specific enthalpy, specific total enthalpy and, under special conditions, in terms of temperature.

To rewrite the total energy equation of equation B.22 in terms of specific internal energy, the kinetic energy has to be subtracted from the total energy. Moukalled, Mangani and Darwish (2016) present a detailed derivation of the kinetic energy equation of which the main steps are repeated here in order to substantiate the derivation of the energy equation in terms of specific internal energy presented in this work.

The kinetic energy equation is obtained by multiplication of the momentum conservation equation with the velocity u

$$\left[\frac{\partial(\rho u)}{\partial t} + \nabla \cdot \{\rho u u\}\right] \cdot u = f \cdot u \tag{B.23}$$

which, after some manipulations and rearranging of terms, becomes

$$\frac{\partial}{\partial t}(\rho u \cdot u) + \nabla \cdot [\rho(u \cdot u)u] - u \cdot \rho\left[\frac{\partial u}{\partial t} + (u \cdot \nabla)u\right] = f \cdot u \tag{B.24}$$

where the $\rho\left[\frac{\partial u}{\partial t} + (u \cdot \nabla)u\right]$-term represents the non-conservative form of the momentum conservation equation which is equal to the net force f acting on the control volume. As mentioned earlier, the net force consists of both surface and body forces. This term can therefore be replaced by similar expressions as presented in equations B.17 and B.18, again neglecting the contribution of the shear forces acting on the control volume. This yields

$$\frac{\partial}{\partial t}\left(\rho\frac{1}{2}u \cdot u\right) + \nabla \cdot \left[\rho\left(\frac{1}{2}u \cdot u\right)u\right] = u \cdot [\nabla \cdot (-P\mathrm{I})] + f_b \cdot u \tag{B.25}$$

in which, by considering conservative normal forces, the pressure $-P$ represents a constant pressure acting upon the control volume. This allows writing the first term on the right hand side as $-u \cdot \nabla P$, stating that the local rate of change of kinetic energy is in part equal to the work done by a pressure gradient ∇P relative to the control volume.

Through application of $\nabla \cdot (Pu) = u \cdot \nabla P + P\nabla \cdot u$, equation B.25 can be rewritten in the following form

$$\frac{\partial}{\partial t}\left(\rho\frac{1}{2}u \cdot u\right) + \nabla \cdot \left[\rho\left(\frac{1}{2}u \cdot u\right)u\right] = -\nabla \cdot (Pu) + P\nabla \cdot u + f_b \cdot u \tag{B.26}$$

Subtracting the kinetic energy from the total energy, i.e. subtracting equation B.26 from equation B.22, yields the energy conservation equation in terms of the specific internal energy U

$$\frac{\partial(\rho U)}{\partial t} + \nabla \cdot (\rho U u) = -\nabla \cdot q_S - P\nabla \cdot u + q_V \tag{B.27}$$

where the contribution of the body forces vanishes.

The $P\nabla \cdot u$ term in equation B.27 is representative of the work done by compression (when defined as a negative) and/or expansion (when defined as a positive) of the fluid volume as a result of a change in the net external pressure acting upon the system when assuming both fluid and rock matrix are compressible, but non-deformable (Faust and Mercer, 1979a). The minus sign indicates work being done on the fluid volume and consequently a loss of combined potential and kinetic energy, which yields an increase in internal energy within the control volume (Toth and Bobok, 2017). Oppositely, the rate of work done by expansion of the fluid volume poses as a sink to internal energy. This means that, for a system subject to a constant external pressure, heat is transferred to and from the system (i.e. control volume) in the form of internal energy and work (i.e. combined potential and kinetic energy).

A state function, derived from the first law of thermodynamics, describing the transfer of heat to a system at constant (external) pressure is the enthalpy H and is defined as

$$H = U + PV \tag{B.28}$$

where the work done on and/or by the fluid volume through pressure inside the fluid volume, and an associated change in (fluid) volume, is captured in the PV-term (Fletcher, 1993). The effect of pressure on the internal energy of the system is best described by the so-called Joule-Thomson effect, which relates the compressibility of liquids and gases to changes in temperature or internal energy. The enthalpy within the liquid volume is constant during either compression or expansion.

By defining the net outgoing flux in terms of internal energy, the contribution of the compressible work PV to the energy in the control volume is neglected. As superheated steam is highly compressible, the work done by compression and/or expansion cannot be disregarded. Therefore, the convective flux should be rewritten in terms of enthalpy. This is straightforward and follows directly from its definition according to which the specific internal energy and specific enthalpy are related by

$$U = H - \frac{P}{\rho} \tag{B.29}$$

where the associated change in volume is described by a change in density. Note that here, again, P represents a constant external pressure acting upon the system. Substituting this relation for the specific internal energy, the convective flux term evolves as

$$\nabla \cdot (\rho U u) = \nabla \cdot \left(\rho \left(H - \frac{P}{\rho}\right) u\right) = \nabla \cdot (\rho H u) - \nabla \cdot (P u) = \nabla \cdot (\rho H u) - P \nabla \cdot u \tag{B.30}$$

where the convective flux now takes into account the effect of pressure on the liquid volume, and the associated change in liquid volume.

Substitution of the expression in equation B.30 into the energy equation of equation B.27 results in the differential form of the energy conservation equation considered in this work

$$\frac{\partial(\rho U)}{\partial t} + \nabla \cdot (\rho H u) = -\nabla \cdot q_S + q_V \tag{B.31}$$

where the work done by compression and/or expansion is captured in the convective flux rather than in a separate source term. Coats (1980) explicitly states that the use of a convective flux in terms of internal energy is mistaken.

The rate of heat transfer q_S represents heat transfer by diffusion, i.e. a conductive heat flux. Thermal diffusion or simply conduction is governed by Fourier's law according to

$$q_S = -[k \nabla T] \tag{B.32}$$

where k is the thermal conductivity of the material. Fourier's law states that heat flows in the direction of the temperature gradient, i.e. from source to sink. In the case of an anisotropic medium the rate of heat transfer is described by the dot product of the thermal conductivity tensor κ and the temperature gradient, and in this case heat does not (necessarily) flows in the direction of the temperature gradient. Substitution of Fourier's law into the energy conservation equation of equation B.31 yields

$$\frac{\partial(\rho U)}{\partial t} + \nabla \cdot (\rho H u) = \nabla \cdot [\kappa \cdot \nabla T] + q_V \tag{B.32}$$

Similar to the description of the mass conservation equation for both single- and two-phase flow, the energy per unit mass within a control volume is the sum of the energy content in both the liquid and vapor phase, i.e. $\phi\rho_w U_w S_w + \phi\rho_s U_s S_s$. In terms of the energy conservation equation, there is additional energy present in the rock matrix of the porous medium, i.e. $(1-\phi)\rho_r U_r$. The phase velocities are again governed by Darcy's law for multiphase flow, assuming capillary pressure is negligible. Under production stresses, a source or sink term is added capturing the energy fluxes of both phases related to the addition and/or extraction of energy to and from the system. This allows rewriting the energy conservation equation of equation B.32 as

$$\frac{\partial}{\partial t}\left[(1-\phi)\rho_r U_r + \phi\sum_{\alpha=1}^{n_p}\rho_\alpha U_\alpha S_\alpha\right] - \nabla\cdot\left(\sum_{\alpha=1}^{n_p}\left(\rho_\alpha H_\alpha \frac{K k_{r,\alpha}}{\mu_\alpha}\cdot(\nabla P - \rho_\alpha g z)\right)\right) = \nabla\cdot\left(\sum_{\beta=1}^{n_p}\left(k_\beta\cdot\nabla T_\beta\right)\right) + q_V + \sum_{\alpha=1}^{n_p}\rho_\alpha H_\alpha q_\alpha \tag{B.33}$$

where the energy flux in the well is defined in terms of specific enthalpy in order to account for the effects of compression and/or expansion of the circulating fluid in the well. The conductive heat flux consists of the thermal conductivities of all phases β, i.e. water, steam and rock matrix, and the respective temperature in each phase.

The presence of radioactive minerals posing as a source of heat is neglected, as well as radiation as a heat transfer mechanism. As viscous shearing effects are assumed negligible no amount of heat is generated through viscous dissipation. The assumption of single-component water as the carrying fluid eliminates the possibility of chemical reactions generating heat within the fluid. Therefore, the rate of heat generation and/or destruction q_V is equal to zero.

Local thermal equilibrium is assumed between all phases. It is based on the assumption that both the liquid and vapor phase flow rates are sufficiently slow and the contact areas between all phases are sufficiently large (Coats, 1977; Ingebritsen et al., 2006). This assumption results in the absence of terms describing the transfer of heat between phases and allows the combination of thermal conductivities of all phases in an average thermal conductivity tensor D. By defining an average conductivity tensor, a single temperature gradient can be applied to the entire control volume, i.e. to all phases. Furthermore, the transfer of heat due to thermal dispersion is assumed negligible because of the high thermal conductivity of the rock matrix (Ingebritsen et al., 2006). The average thermal conductivity tensor D is defined as

$$D_{ave} = (1-\phi)D_r + \phi(S_w D_w + S_s D_s) \tag{B.34}$$

in which D_r, D_w and D_s are the phase thermal conductivities of rock, water and steam, respectively.

Based on these assumptions, the energy conservation equation of the model problem is written as

$$\frac{\partial}{\partial t}\left[(1-\phi)\rho_r U_r + \phi\sum_{\alpha=1}^{n_p}\rho_\alpha U_\alpha S_\alpha\right] - \nabla\cdot\left(\sum_{\alpha=1}^{n_p}\left(\rho_\alpha H_\alpha \frac{Kk_{r,\alpha}}{\mu_\alpha}\cdot(\nabla P - \rho_\alpha g z)\right)\right)$$
$$-\nabla\cdot(D_{ave}\cdot\nabla T) = \sum_{\alpha=1}^{n_p}\rho_\alpha H_\alpha q_\alpha \tag{B.35}$$

where the conductive flux term is written on the left-hand-side to illustrate the formulation presented in equation B.5, i.e. $accumulation - net\ outgoing\ flux = source\ term$, in which the $net\ outgoing\ flux$ is equal to the sum of the convective and conductive heat fluxes.

Again, by defining the fluid phase mobility $\lambda_\alpha = \frac{Kk_{r,\alpha}}{\mu_\alpha}$, and by defining total fluid properties to capture the summation operators for the different phases, equation B.35 can be simplified to

$$\frac{\partial}{\partial t}[(1-\phi)\rho_r U_r + \phi\rho_t U_t] - \nabla\cdot((\rho H\lambda)_t\nabla P - (\rho^2 H\lambda)_t g\nabla z) -$$
$$\nabla\cdot(D_{ave}\cdot\nabla T) = (\rho H q)_t \tag{B.36}$$

where the total convective energy flux $(\rho H\lambda)_t = \rho_w H_w\lambda_w + \rho_s H_s\lambda_s$, the gravity term $(\rho^2 H\lambda)_t = \rho_w^2 H_w\lambda_w + \rho_s^2 H_w\lambda_s$ and the source term $(\rho H q)_t = \rho_w H_w q_w + \rho_s H_s q_s$. The total internal energy of the water-steam mixture U_t is defined as the weighted average of the phase specific internal energies with respect to mass, and is written as

$$U_t = \frac{\rho_w U_w S_w + \rho_s U_s S_s}{\rho_w S_w + \rho_s S_s} = \frac{\rho_w U_w S_w + \rho_s U_s S_s}{\rho_t} \tag{B.37}$$